

# Surface Modification and Polymer-Free Transfer of Vertical Graphene Nanosheets for Electrochemical Capacitor Applications

By

**GOPINATH SAHOO**

(Enrolment No. PHYS 02 2015 04 023 )

**Indira Gandhi Centre for Atomic Research, Kalpakkam, India**

*A thesis submitted to the  
Board of Studies in Physical Sciences  
in partial fulfillment of requirements  
for the Degree of*

**DOCTOR OF PHILOSOPHY**

of

**HOMI BHABHA NATIONAL INSTITUTE**



September, 2020

## Homi Bhabha National Institute

### Recommendations of the Viva Voce Board

As members of the Viva Voce Committee, we certify that we have read the dissertation prepared by **Gopinath Sahoo** entitled “**Surface Modification and Polymer-Free Transfer of Vertical Graphene Nanosheets for Electrochemical Capacitor Applications**” and recommend that it may be accepted as fulfilling the thesis requirement for the award of Degree of Doctor of Philosophy.

N.V. Chandra Shekar Date: 21/01/2021  
(Chairman: Dr. N. V. Chandra Shekar)

M. Kamruddin Date: 21/01/2021  
(Guide/Convener: Dr. M. Kamruddin)

3. RA Date: 21/01/2021  
(External Examiner: Dr. Viswanath Balakrishnan)

Tom Mathews Date: 21/01/2021  
(Member 1: Dr. Tom Mathews)

Sharat Chandra Date: 21/01/2021  
(Member 2: Dr. Sharat Chandra)

Santanu Bera Date: 21/01/2021  
(Member 3: Dr. Santanu Bera)

P. S. R. Polaki Date: 21/01/2021  
(Technology Advisor: Dr. S. R. Polaki)

Final approval and acceptance of this thesis is contingent upon the candidate's submission of the final copies of the thesis to HBNI.

I hereby certify that, I have read this thesis prepared under my direction and recommend that it may be accepted as fulfilling the thesis requirement

Date: 21/01/2021

Place: Kalpakkam

M. Kamruddin  
(Dr. M. Kamruddin)

(Guide)

## Homi Bhabha National Institute

### Recommendations of the Viva Voce Board

As members of the Viva Voce Committee, we certify that we have read the dissertation prepared by **Gopinath Sahoo** entitled “**Surface Modification and Polymer-Free Transfer of Vertical Graphene Nanosheets for Electrochemical Capacitor Applications**” and recommend that it may be accepted as fulfilling the thesis requirement for the award of Degree of Doctor of Philosophy.

N.V. Chandra Shekar Date: 21/01/2021  
(Chairman: Dr. N. V. Chandra Shekar)

M. Kamruddin Date: 21/01/2021  
(Guide/Convener: Dr. M. Kamruddin)

3.RA Date: 21/01/2021  
(External Examiner: Dr. Viswanath Balakrishnan)

Tom Mathews Date: 21/01/2021  
(Member 1: Dr. Tom Mathews)

Sharat Chandra Date: 21/01/2021  
(Member 2: Dr. Sharat Chandra)

Santanu Bera Date: 21/01/2021  
(Member 3: Dr. Santanu Bera)

P. S. R. Polaki Date: 21/01/2021  
(Technology Advisor: Dr. S. R. Polaki)

Final approval and acceptance of this thesis is contingent upon the candidate's submission of the final copies of the thesis to HBNI.

I hereby certify that, I have read this thesis prepared under my direction and recommend that it may be accepted as fulfilling the thesis requirement

Date: 21/01/2021

Place: Kalpakkam

M. Kamruddin  
(Dr. M. Kamruddin)

(Guide)



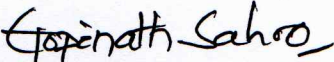
## STATEMENT BY AUTHOR

This dissertation has been submitted in partial fulfillment of requirements for an advanced degree at Homi Bhabha National Institute (HBNI) and is deposited in the Library to be made available to borrowers under rules of the HBNI.

Brief quotations from this dissertation are allowable without special permission, provided that accurate acknowledgment of source is made. Requests for permission for extended quotation from or reproduction of this manuscript in whole or in part may be granted by the Competent Authority of HBNI when in his or her judgment the proposed use of the material is in the interests of scholarship. In all other instances, however, permission must be obtained from the author.

Date: 21/01/2021

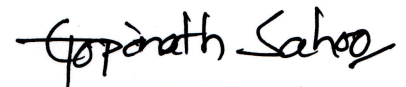
Place: Kalpakkam

  
GOPINATH SAHOO



## DECLARATION

I, hereby declare that the investigation presented in the thesis has been carried out by me. The work is original and has not been submitted earlier as a whole or in part for a degree/diploma at this or any other Institution/University.

  
GOPINATH SAHOO



# List of Publications

## (a) Journals:

1. Synergetic effect of NiO<sub>x</sub> decoration and oxygen plasma treatment on electrochemical capacitor performance of vertical graphene nanosheets. **Gopinath Sahoo**, S. R. Polaki, P. Anees, N. G. Krishna, T. Mathews, M. Kamruddin; **ACS Appl. Energy Mater.**, 2021, DOI:10.1021/acsaem.0c02683.
2. Engineering the edge-termination and defect-density to enhance the electrochemical capacitance performance of vertical graphene nanosheets. S. R. Polaki, **Gopinath Sahoo**, P. Anees, N. G. Krishna, M. Kamruddin, S. Dhara; **Appl. Surf. Sci.**, 545 (2021) 149045.
3. Insights into the electrochemical capacitor performance of transition metal-vertical graphene nanosheets hybrid electrodes. **Gopinath Sahoo**, S. R. Polaki, P. Anees, S. Ghosh, S. Dhara, M. Kamruddin; **Phys. Chem. Chem. Phys.**, 21 (2019) 25196.
4. Electrochemical capacitor performance of TiO<sub>2</sub> decorated vertical graphene nanosheets electrode. **Gopinath Sahoo**, S. R. Polaki, N. G. Krishna, M. Kamruddin; **J. Phys. D: Appl. Phys.**, 52 (2019) 375501.
5. Plasma-tuneable oxygen functionalization of vertical graphenes enhance electrochemical capacitor performance. **Gopinath Sahoo**, S. R. Polaki, S. Ghosh, N. G. Krishna, M. Kamruddin, K. Ostrikov; **Energy Storage Mater.**, 14 (2018) 297-305.
6. Temporal-stability of plasma functionalized vertical graphene electrodes for charge storage. **Gopinath Sahoo**, S. R. Polaki, S. Ghosh, N. G. Krishna, M. Kamruddin; **J. Power Sources**, 401 (2018) 37-48.
7. Enhanced supercapacitance of activated vertical graphene nanosheets in hybrid electrolyte. S. Ghosh, **Gopinath Sahoo**, S. R. Polaki, N. G. Krishna, M. Kamruddin, T. Mathews; **J. Appl. Phys.**, 122 (2017) 214902.
8. Scalable transfer of vertical graphene nanosheets for flexible supercapacitor applications. **Gopinath Sahoo**, S. Ghosh, S. R. Polaki, T. Mathews, M. Kamruddin; **Nanotechnology**, 28 (2017) 415702.

## (b) Oral/Poster presentation:

1. Plasma surface modification of vertical graphene nanostructures for high electrochemical capacitor performance. **Gopinath Sahoo**, S. R. Polaki, N. G. Krishna, M. Kamruddin; 30<sup>th</sup> International Conference on Diamond and Carbon Materials (ICDCM), Melia lebreros, Seville, Spain, 2019 (September 8-12): Poster presentation (**Young scientist international travel grant, SERB, DST, India**).
2. Super-wetting vertical graphene nanosheets for energy storage applications. S. R. Polaki, **Gopinath Sahoo**, M. Kamruddin; International Conference on Supercapacitors, Energy storage and Applications (ICSEA), Center for materials for electronics technology (C-MET), Thrissur, Kerala, India, 2019 (March 8-10): Oral presentation
3. Conformal deposition of titanium nanoparticles on vertical graphene for supercapacitance enhancement. **Gopinath Sahoo**, S. R. Polaki, M. Kamruddin; Research Scholar Meet on Material Science and Engineering of Nuclear Materials (RSM-MSENM), HBNI, IGCAR, Kalpakkam, India, 2018 (May 7-9): Poster presentation.
4. Oxygen plasma treated vertical graphene nanosheets for supercapacitor application. **Gopinath Sahoo**, S. Ghosh, S. R. Polaki, M. Kamruddin; International Conference on Nanotechnology: Ideas, Innovations and Initiatives (ICN:3I), IIT Roorkee, Roorkee, India, 2017 (December 6-8): Oral presentation (**Best oral presentation**).
5. Effect of post-growth annealing on structural and wetting property of vertical graphene nanosheets. **Gopinath Sahoo**, S. Ghosh, S. R. Polaki, M. Kamruddin; International Conference on Advances in Nanomaterials and Nanotechnology (ICANN), Jamia Millia Islamia, New Delhi, India, 2016 (November 4-5): Poster presentation.

## (c) Other publications (Not Included in the Thesis)

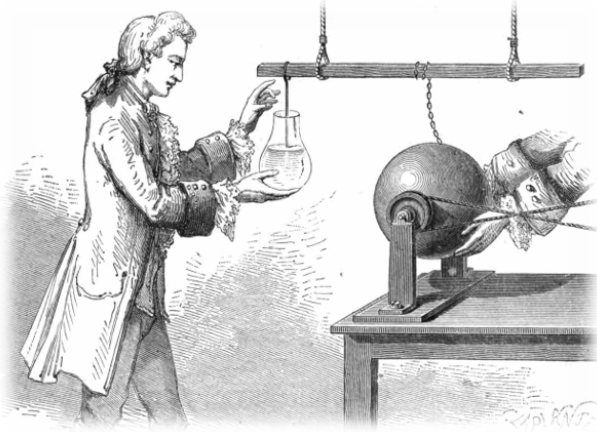
1. Engineering high-defect densities across vertically-aligned graphene nanosheets to induce photocatalytic reactivity. A. Guirguis, S. R. Polaki, **Gopinath Sahoo**, S. Ghosh, M. Kamruddin, A. Merenda, X. Chen, J. W. Maina, G. Szekely, L. Dumege; **Carbon**, 168 (2020) 32-41.

2. Influence of barium doping on structural and magnetic properties of bismuth ferrite thin films via spray pyrolysis method. T. K. Pani, B. Sundaray, **Gopinath Sahoo**, D. Rout; **J. Phys. D: Appl. Phys.**, **53** (2020) 325001.
3. Designing metal oxide-vertical graphene nanosheets structures for 2.6 V aqueous asymmetric electrochemical capacitor. S. Ghosh, S. R. Polaki, **Gopinath Sahoo**, E. M. Jin, M. Kamruddin, J. S. Cho, S. M. Jeong; **J. Ind. Eng. Chem.**, **72** (2019) 107-116.

  
GOPINATH SAHOO



**Dedicated to**  
**Science and my parents**  
**Bhagaban Sahoo and Kuni Sahoo**



I've found out so much about electricity that I've reached the point where I understand nothing and can explain nothing.

- Pieter van Musschenbroek



## Acknowledgments

In this page, I want to recall the people behind the scene, contributed to this journey towards the dissertation, without them reaching the goal and this dissertation would not have been possible.

First and foremost, I am grateful to thank my supervisor, Dr. M. Kamruddin, for his valuable guidance, constant encouragement and support throughout the course of present dissertation.

I am also very grateful to the distinguished faculty in my doctoral committee, Dr. A. K. Tyagi (former), Dr. N. V. Chandra Shekar, Dr. Saroja Saibaba (former), Dr. Tom Mathews, Dr. Sharat Chandra, Dr. Santanu Bera, Dr. S. R. Polaki and Dr. R. Pandian (former) for sharing their valuable time, providing valuable comments and evaluating my work at each stage.

I want to express my gratitude to Dr. A. K. Bhaduri and Dr. S.A.V. Satya Murty, present and former Director, IGCAR, for permitting me to pursue Ph. D. at IGCAR. I am highly thankful to Dr. Shaju K. Albert and Dr. G. Amarendra, present and former Group Director, MSG, for providing a pleasant atmosphere for my smooth research. I thank Dr. T. S. Lakshmi Narasimhan and Dr. M. Saibaba, present and former Dean SA, for the wonderful hospitality during my stay at JRF Enclave. I would like to thank Dr. R. Rajaraman, Dr. N. V. Chandra Shekar and Dr. B. V. R. Tata, present and former Dean physical sciences, HBNI, IGCAR for their support and being friendly during all the procedure throughout the tenure.

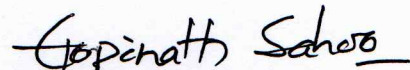
It is my pleasure to express my gratitude to Dr. S. R. Polaki and my senior, Dr. Subrata Ghosh, for their suggestions and constructive reviews that helped me to improve a lot. I would like to thank Dr. S. K. Dhara and Dr. G. Mangamma for their suggestions and

corrections. I want to extend my sincere thank to Dr. K. Ostrikov (Queensland University of Technology, Australia), Mr. N. G. Krishna, Dr. Anees P., Dr. Shamima Hussain, Dr. S. Amirthapandian, Mr. Magudapathy, Dr. K. Ganesan, Dr. P. K. Aji Kumar, Dr. P. A. Manoj Kumar, Dr. Arindam Das, Dr. K. K. Madapu, Dr. R. Krishnan, Dr. Madhusmita Sahoo, Mrs. Sheela, Mr. Ashok Bahuguna and all members of MSG for the collaboration, discussions and immensely help in various stages of my Ph.D. career.

I would like to acknowledge the Dept. of Atomic Energy, Govt. of India for research fellowship. I am also thankful to all reviewers and examiner for their time and careful evaluation.

I would like to thank my seniors, batchmates, friends, juniors, Dr. Avinash Patsha, Dr. Bonu Venkatramana, Dr. A. K. Sivadasan, Dr. Madhusmita Panda, Dr. Raktima Basu, Ijee, Pragyna, Akshaya, Rajitha, Jakatha, Bala, Dhilipan, Darpan, Vikas, Pavan, Madhav, Reshma P R, Mohasin, Abinash, Reshma T S, Hrudya and all research scholars of IGCAR for their suggestions, encouragement, friendship and help during these years. I am thankful to the musketeers' group; Dr. Santanu Parida, Dillip, Alok, Binaya, Bijay, Dr. Padmalochan Panda, Dr. Nilakantha Meher, Pradosh, Sitakanta, Prashant, Anil, Suvendu for the energy boost trips and keeping me happy. I wish to extend my sincere gratitude to all my teachers, who had taught me at educational career.

Finally, I am thankful to my beloved parents and the whole family for their encouragement and unconditional love. I am grateful to my sisters: Manika, Sasi, Pratima, brother: Sana and brother-in-law's whose encouragement helped me to go forward. Special thanks to Aliva (Mama) for all her adoration, care and support for me and for everything. Thanks to my big brother Manoranjan Dash for his advice, support and faith. Thank you all for your love, patience and help to make it possible.

  
GOPINATH SAHOO

# Contents

	Page
<b>Abstract</b>	<b>xv</b>
<b>1 Introduction</b>	<b>1</b>
1.1 Two-dimensional carbon . . . . .	1
1.2 VGN and its properties . . . . .	4
1.3 Electrochemical capacitors . . . . .	8
1.4 Difficulties in the polymer based transfer process . . . . .	14
1.5 Surface modification: a strategy to enhance electrochemical capacitance . . . . .	16
1.6 Research objectives and overview of the thesis . . . . .	21
<b>2 Experimental techniques</b>	<b>25</b>
2.1 Introduction . . . . .	25
2.2 Growth techniques . . . . .	26
2.2.1 Electron cyclotron resonance chemical vapor deposition . . . . .	26
2.2.2 Thermal evaporation unit . . . . .	29
2.2.3 DC sputtering . . . . .	30
2.3 Characterization techniques . . . . .	31
2.3.1 Morphological characterization . . . . .	31
2.3.2 X-ray photoelectron spectroscopy (XPS) . . . . .	31
2.3.3 Raman spectroscopy . . . . .	33
2.3.4 Contact angle measurement . . . . .	35
2.3.5 Four-probe point method . . . . .	36
2.3.6 Electrochemical measurement . . . . .	38
2.4 Summary . . . . .	41
<b>3 Growth of vertical graphene nanosheets and scalable transfer for flexible supercapacitor applications</b>	<b>43</b>
3.1 Introduction . . . . .	43
3.2 Growth and transfer of VGN . . . . .	44
3.2.1 Growth of VGN . . . . .	44

3.2.2	Transfer of VGN . . . . .	45
3.3	Morphology and structural analysis . . . . .	48
3.4	Surface chemistry analysis . . . . .	50
3.5	Electrical property study . . . . .	51
3.6	Electrochemical capacitance study . . . . .	52
3.7	Conclusion . . . . .	56
<b>4</b>	<b>Plasma activated VGN for enhanced electrochemical capacitance</b>	<b>57</b>
4.1	Introduction . . . . .	57
4.2	Tuneable oxygen plasma activation of VGN and capacitor performance . . . . .	60
4.2.1	Morphological analysis . . . . .	60
4.2.2	Structural analysis . . . . .	62
4.2.3	Water contact angle measurement . . . . .	64
4.2.4	Surface chemistry analysis . . . . .	64
4.2.5	Electrochemical capacitance study . . . . .	68
4.2.6	Discussion . . . . .	72
4.3	Different plasma activation of VGN and capacitor performance . . . . .	74
4.3.1	Morphological analysis . . . . .	74
4.3.2	Structural analysis . . . . .	75
4.3.3	Contact angle measurement and surface energy calculation . . . . .	76
4.3.4	Surface chemistry analysis . . . . .	77
4.3.5	Electrochemical capacitance study . . . . .	79
4.3.6	Discussion . . . . .	81
4.4	Temporal stability of oxygen plasma activated VGN . . . . .	81
4.4.1	Water contact angle measurement . . . . .	82
4.4.2	Surface chemistry analysis . . . . .	83
4.4.3	Electrochemical capacitance study . . . . .	84
4.4.4	Discussion . . . . .	84
4.5	Symmetric supercapacitor fabrication and performance . . . . .	86
4.6	Conclusion . . . . .	89
<b>5</b>	<b>Metal/metal oxide-VGN hybrid structures and their electrochemical capacitor performance</b>	<b>91</b>
5.1	Introduction . . . . .	91
5.2	Metal-VGN hybrid electrodes and the effect of charge transfer on electrochemical capacitance . . . . .	93
5.2.1	Morphological analysis . . . . .	93
5.2.2	Structural analysis . . . . .	94
5.2.3	Surface chemistry analysis . . . . .	96
5.2.4	Electrical measurement . . . . .	99

5.2.5	Electrochemical capacitance study . . . . .	101
5.2.6	Computational analysis of charge transfer . . . . .	105
5.2.7	Dicsussion . . . . .	109
5.3	Metal oxide-VGN hybrid structure and the electrochemical capacitance .	110
5.3.1	Morphological analysis . . . . .	110
5.3.2	Structural analysis . . . . .	111
5.3.3	Electrochemical capacitance study . . . . .	113
5.3.4	Surface chemistry analysis . . . . .	115
5.4	Conclusion . . . . .	117
<b>6</b>	<b>Electrochemical capacitor performance of activated VGN in hybrid electrolyte</b>	<b>119</b>
6.1	Introduction . . . . .	119
6.2	Growth and activation of VGN . . . . .	121
6.3	Morphology and structural analysis . . . . .	121
6.4	Water contact angle measurement . . . . .	123
6.5	Surface chemistry analysis . . . . .	124
6.6	Electrochemical capacitance study . . . . .	125
6.7	Conclusion . . . . .	132
<b>7</b>	<b>Summary and future scope</b>	<b>133</b>
7.1	Summary of the Thesis . . . . .	133
7.2	Future scope . . . . .	135
	References. . . . .	137

# List of Figures

1.1	(a) Graphene crystal structure, (b) schematic of <i>in-plane</i> $\sigma$ and perpendicular $\pi$ bonds, (c) band-energy diagram of graphene and (d) graphitic allotropes: layered 3D structure of graphite, 0D allotrope: C <sub>60</sub> molecule fullerene, 1D allotrope: single-wall carbon nanotube. . . . .	3
1.2	Schematic representation of VGN structure and its amazing properties. . . . .	5
1.3	Schematic of various applications of VGN (images are taken from the corresponding references given in text). . . . .	6
1.4	Schematic of a conventional/electrostatic capacitor. . . . .	8
1.5	(a) Ragone plot and (b) schematic of the a typical supercapacitor. . . . .	9
1.6	Schematic of EDLC and pseudocapacitance charge storage. . . . .	10
1.7	Schematic of the electric double layer charge storage mechanisms. . . . .	11
1.8	(a) Schmatic of the LIFT technique, (b) Shows the damaged structure after the LIFT transfer and (c) schematic of the polymer based transfer process. Pictures are taken from the literature discussed in text. . . . .	15
2.1	(a) Photograph and (b) schematic of the ECRCVD. . . . .	27
2.2	Typical temperature vs. time growth profile for VGN. . . . .	28
2.3	Schematic of thermal evaporation unit. . . . .	29
2.4	Schematic of (a) sputtering process and (b) DC spurrering unit. . . . .	31
2.5	Schematic view of X-ray photo electron emission process and (b) block diagram of XPS. . . . .	32
2.6	Schematic of scattering process in Raman spectroscopy. . . . .	33
2.7	Schematic of the Raman spectrometer. . . . .	34
2.8	Schematic (a) of the contact angle by a liquid droplet, (b) illustration of relation between angles and (c) contact angle set up in our lab. . . . .	36
2.9	Schematic of four point probe contact on the arbitrary shape of the material. . . . .	37
2.10	(a) Schematic of three electrode system, and (b) block diagram of potentiostat/galvanostat. . . . .	39
2.11	Photograph of electrochemical setup. . . . .	39
3.1	Photograph of transferred VGN to overhead projector (OHP) sheet. . . . .	46

3.2	Schematic of the transfer process of VGN onto flexible substrate. (a) VGN/Ni, (b) baked VGN/Ni, (c) floated VGN/Ni in FeCl <sub>3</sub> solution, (d) freely floating VGN after Ni etching, (e) dilution of FeCl <sub>3</sub> solution by DI water, (f) free floating VGN on DI water, (g) scooped out VGN to flexible substrate and (h), (i) optical image of 2×1 cm <sup>2</sup> VGN on flexible substrate with scaling. . . . .	47
3.3	FESEM micrograph of (a) as-grown VGN/Ni and (b) transferred VGN/OHP ; 1 cm = 500 nm, (c) cross sectional image of VGN with NG layer and (d) Raman spectra of as-grown and transferred VGN. . . . .	49
3.4	WCA of (a) as-grown VGN/Ni and (b) transferred VGN/OHP. . . . .	50
3.5	XPS spectra of (a) C1s and (b) Fe2p spectrum of transferred VGN/OHP. . . . .	51
3.6	I-V characteristic of transferred VGN/OHP. Inset shows the schematic of electrical contacts on VGN for measurement. . . . .	52
3.7	CV of (a) as-grown VGN/Ni and (b) transferred VGN/OHP in the 3-electrode system at different scan rates, (c) comparative CV of VGN/Ni and VGN/OHP at a scan rate of 300 mV/s, (d) plot of areal capacitance of VGN/Ni and VGN/OHP as a function of scan rate, (e) charge-discharge profile of transferred VGN at different current densities and (f) capacitive retention versus cycle number; inset shows few charge/discharge cycles. . . . .	53
3.8	(a) Schematic of symmetric VGN supercapacitor device (b) Photograph of the transfer electrode for device. . . . .	55
3.9	Electrochemical capacitance performance of the symmetric device in 2-electrode setup; (a) CV at different scan rates, (b) plot of areal capacitance <i>vs.</i> scan rate, (c) charge-discharge profile at different current densities and (d) capacitance retention <i>vs.</i> cycle number, inset of (d) represents few charge-discharge cycles. . . . .	56
4.1	FESEM micrograph of (a) as-grown VGN (b) 600 W <i>ex-situ</i> and (c) 600 W <i>in-situ</i> plasma-treated VGN. Insets show the respective cross-section images. HRTEM micrograph of (d) as-grown VGN (e) 600 W <i>ex-situ</i> and (f) 600 W <i>in-situ</i> plasma-treated VGN. . . . .	61
4.2	Inter-sheet distance distribution for as-grown VGN, 600 W <i>ex-situ</i> and 600 W <i>in-situ</i> plasma-treated VGN. . . . .	62
4.3	Raman spectra of (a) typical as-grown VGN and (b) plasma-treated VGN at different plasma powers; the variation of (c) FWHM <sub>D</sub> , FWHM <sub>G</sub> and FWHM <sub>G'</sub> as well as (d) I <sub>D</sub> /I <sub>G</sub> , I <sub>D'</sub> /I <sub>G</sub> and I <sub>G'</sub> /I <sub>G</sub> for as-grown and plasma-treated VGN. . . . .	63
4.4	Water contact angle photograph of VGN (a) before and (b) after plasma treatment. . . . .	64
4.5	XPS C1s spectra for (a) as-grown VGN, (b) 600 W <i>ex-situ</i> and (c) 600 W <i>in-situ</i> plasma-treated VGN; XPS O1s spectra for (e) 600 W <i>ex-situ</i> and (e) 600 W <i>in-situ</i> plasma-treated VGN. . . . .	65

4.6	(a) CV and (b) CD curve of as-grown VGN, (c) CV comparison of as-grown and 600 W <i>ex-situ</i> and <i>in-situ</i> plasma-treated VGN, (d) areal capacitance of all the samples, (e) CV of 600 W <i>in-situ</i> plasma-treated VGN, and (f) capacitance retention for as-grown and 600 W <i>in-situ</i> plasma-treated VGN, inset shows the CD for 600 W <i>in-situ</i> plasma-treated VGN. . . . .	68
4.7	CV of 1 <sup>st</sup> and 1000 <sup>th</sup> cycles for alcohol soaked VGN at 0.1 mV/s. . . . .	70
4.8	Mean current passed during anodic/cathodic scan for (a) as-grown VGN, (b) 600 W <i>ex-situ</i> and (c) 600 W <i>in-situ</i> as a function of scan rate. . . . .	71
4.9	Impedance responses of as-grown VGN, 600 W <i>ex-situ</i> and 600 W <i>in-situ</i> plasma-treated VGN: (a) Nyquist plot, inset represents the equivalent circuit of fitted impedance spectra and (b) Bode plot . . . . .	72
4.10	Schematic representation oxygenated functional groups attached to the plasma-treated VGN surfaces and dependence on capacitance. . . . .	73
4.11	FESEM micrographs of (a) as-grown VGN (b) H <sub>2</sub> -VGN (c) N <sub>2</sub> -VGN and (d) O <sub>2</sub> -VGN. . . . .	74
4.12	(a) Raman spectra of as-grown and different plasma-treated VGN and (b) change in FWHM <sub>G</sub> and I <sub>D</sub> /I <sub>G</sub> after plasma treatment. . . . .	75
4.13	(a) Water contact angle (WCA) and (b) Glycerol contact angle (GCA) of as-grown and different plasma-treated VGN samples; and (c) Bar graph representing the calculated surface energy of the as-grown and plasma-treated VGN. . . . .	76
4.14	(a) XPS spectra of as-grown and different plasma-treated VGN and (b) FTIR spectra for different plasma-treated VGN. . . . .	77
4.15	C1s XPS spectra for different plasma-treated VGN (a-c) and N1s XPS spectra of N <sub>2</sub> plasma-treated VGN. . . . .	78
4.16	CV and CD for (a, d) H <sub>2</sub> -VGN, (b, e) N <sub>2</sub> -VGN and (c, f) O <sub>2</sub> -VGN. . . . .	79
4.17	(a) CV comparison at 0.1 V/s and (b) areal capacitance <i>vs.</i> scan rate profile, for as-grown and different plasma-treated VGN. . . . .	80
4.18	Contact angle <i>vs.</i> ageing time of as-grown and plasma-treated VGN at different powers. . . . .	82
4.19	O/C percentage variation (a) for plasma-treated VGN after 90 days and (b) for 600 W at different WCA. . . . .	83
4.20	(a) CV of as-grown and 600 W plasma-treated VGN for WCA 0°, 60° and 80° at 0.1 V/s scan rate (b) Change in areal capacitance and WCA with ageing time for as-grown and 600 W plasma-treated VGN. . . . .	84
4.21	Structural models for change in WCA (a) before and after plasma treatment and (b) with ageing. . . . .	85
4.22	Schematic of the symmetric electrochemical capacitor device. . . . .	86

4.23	(a) CV of coin-type device at different scan rates, (b) change in areal capacitance with scan rate, inset shows the CV and CD at different potential window, (c) CD at different current densities and (d) capacitance retention for 5000 cycles at 0.1 mA/cm <sup>2</sup> , inset shows the CD curve comparison for 1 <sup>st</sup> and 5000 <sup>th</sup> cycle. Impedance responses of coin-type device (e) Nyquist plot (inset shows the entire range of frequency and Randel's circuit) and (f) Bode plot, inset shows the discharge of the device through LED. . . .	87
5.1	FESEM micrographs of (a) as-grown VGN on CP (VGN/CP) and inset shows magnified image and (b) a cross-sectional image of as-grown VGN. Magnified micrographs of the metal nanoparticle (c) Au, (d) Ag, (e) Cu and (f) Ni decorated VGN/CP. . . . .	93
5.2	(a) Raman spectrum of as-grown VGN with deconvoluted peaks and (b) Raman spectra of as-grown and metal-decorated VGN. . . . .	94
5.3	Variations in the POS <sub>G</sub> , FWHM <sub>G</sub> and I <sub>D</sub> /I <sub>G</sub> values of as-grown VGN and different metal-decorated VGN. . . . .	95
5.4	XPS spectra of (a) Au4 <i>f</i> , (b) Ag3 <i>d</i> , (c) Cu2 <i>p</i> and (d) Ni2 <i>p</i> . . . . .	96
5.5	XPS C1 <i>s</i> spectra for as-grown and metal-decorated VGN. . . . .	97
5.6	XPS O1 <i>s</i> spectra for as-grown and metal-decorated VGN. . . . .	98
5.7	A schematic diagram showing the metal-induced formation of oxygen functional groups. . . . .	99
5.8	A schematic diagram of work function dependent charge (e <sup>-</sup> ) transfer at the VGN and metal NP interface. . . . .	100
5.9	(a) A comparison of CVs for as-grown and different NP-decorated VGN, (b) plots of areal capacitance <i>vs.</i> scan rate of as-grown and metal NP-decorated VGN, (c) CVs and, (d) CD data of Ni/VGN, (e) impedance spectra for as-grown and metal-decorated VGN (the inset shows the fitted equivalent circuit), and (f) capacitance retention and coulombic efficiency (inset) for as-grown and metal-decorated VGN. . . . .	102
5.10	The optimized geometries of TM particles adsorbed on a graphene sheet (6×6×1 super-cell): top view (a-d) and side view (e-h). . . . .	107
5.11	Variation of capacitance and the different factors affecting the capacitance. . . . .	109
5.12	FESEM micrograph of as-grown and NiO decorated VGN; (a) as-grown VGN with cross-sectional image in the inset (b) NiO <sub>30s</sub> /VGN (c) NiO <sub>2m</sub> /VGN (c) NiO <sub>5m</sub> /VGN and (d) NiO <sub>10m</sub> /VGN. . . . .	111
5.13	Shows (a) Raman spectra for as-grown and different NiO decorated VGN and (b) full spectra and inset confirms NiO peak. . . . .	112
5.14	Shows (a) CV comparison at 0.1 V/s scan rate, (b) areal capacitance at 0.1 V/s for different NiO/VGN, (d) CV at different scan rates, (e) CD at different current densities for 5m NiO deposited VGN, (e) capacitance stability for different NiO/VGN and (f) capacitance retention for different NiO/VGN (inset shows the coulombic efficiency). . . . .	114

5.15	(a) Magnified FESEM micrograph of TiO <sub>2</sub> decorated VGN (TiO <sub>2</sub> /VGN), (b) O1s spectra of TiO <sub>2</sub> /VGN, (c) CV comparison of as-grown VGN, TiO <sub>2</sub> decorated on carbon paper (TiO <sub>2</sub> /CP) and TiO <sub>2</sub> /VGN (d) CV of TiO <sub>2</sub> /VGN at different scan rates. . . . .	115
5.16	Shows XPS spectra: (a) C1s, (b) O1s and (c) Ni2p spectra for NiO <sub>5m</sub> /VGN.	116
6.1	(a)-(c) SEM micrograph of VGN with different magnifications (d) Magnified image of single nanosheets after KOH activation. . . . .	122
6.2	Raman spectra of as-grown and activated vertical graphene nanosheets. . . . .	123
6.3	Water contact angle of (a) as-grown and (b) activated VGN, contact angle of as-grown VGN in (c) 1M H <sub>2</sub> SO <sub>4</sub> , and (d) 1M TEABF <sub>4</sub> /H <sub>2</sub> SO <sub>4</sub> . . . . .	124
6.4	(a) XPS survey spectra of as-grown and activated VGN and C1s spectra of (b) as-grown and (c) activated VGN. . . . .	125
6.5	CV of (a) VGN in 1M H <sub>2</sub> SO <sub>4</sub> , (b) VGN in 1M TEABF <sub>4</sub> /H <sub>2</sub> SO <sub>4</sub> , and (c) activated VGN in 1M TEABF <sub>4</sub> /H <sub>2</sub> SO <sub>4</sub> ; (d) comparative CV at the 500 mV/s scan rate; CV with an extended potential window of (e) VGN in 1M TEABF <sub>4</sub> /H <sub>2</sub> SO <sub>4</sub> and (f) activated VGN in 1M TEABF <sub>4</sub> /H <sub>2</sub> SO <sub>4</sub> . . . . .	126
6.6	Schematic of the different ion adsorbed VGN electrode in TEABF <sub>4</sub> /H <sub>2</sub> SO <sub>4</sub> .	129
6.7	CD profile of (a) VGN in 1M H <sub>2</sub> SO <sub>4</sub> , (b) VGN in 1M TEABF <sub>4</sub> /H <sub>2</sub> SO <sub>4</sub> , and (c) activated VGN in 1M TEABF <sub>4</sub> /H <sub>2</sub> SO <sub>4</sub> ; (d) variation of the areal capacitance of VGN in 1M H <sub>2</sub> SO <sub>4</sub> , VGN in TEABF <sub>4</sub> /H <sub>2</sub> SO <sub>4</sub> , and activated VGN in TEABF <sub>4</sub> /H <sub>2</sub> SO <sub>4</sub> with respect to current density in the range of 0.05 mA/cm <sup>2</sup> to 0.5 mA/cm <sup>2</sup> . . . . .	130
6.8	(a) Capacitance retention with respect to the CD cycle number and (b) comparison of CV after the cyclability test for activated VGN in TEABF <sub>4</sub> /H <sub>2</sub> SO <sub>4</sub> at 0.1 V/s. . . . .	131
6.9	Impedance responses of VGN in H <sub>2</sub> SO <sub>4</sub> , VGN in TEABF <sub>4</sub> /H <sub>2</sub> SO <sub>4</sub> and activated VGN TEABF <sub>4</sub> /H <sub>2</sub> SO <sub>4</sub> : (a) Nyquist plot and (b) Bode plot. The inset of (a) represents the equivalent circuit used for impedance curve fitting.	131

# List of Tables

2.1	Typical parameters of arc-discharge, radio frequency and microwave plasma used for nanomaterial synthesis. . . . .	26
4.1	Comparison of the areal capacitance values for plasma-treated VGN. . .	59
4.2	XPS C1s spectra fitted parameters for as-grown and plasma-treated VGN.	67
4.3	XPS O1s spectra fitted parameters for as-grown and plasma-treated VGN.	67
5.1	Work functions for VGN, metal and metal oxides from the literature. . .	101
5.2	Electrochemical capacitance comparison of NiO and carbon nanostructure/NiO hybrid electrodes. . . . .	103
5.3	Adsorption energy for different sites of metal decorated adatoms on graphene.	106
5.4	Effective charges on the transition metal and carbon atoms. . . . .	108
5.5	Tabulated $FWHM_D$ , $FWHM_G$ , $FWHM_{G'}$ , $I_D/I_G$ and $I_{G'}/I_G$ for as-grown and different NiO deposited VGN. . . . .	112
5.6	XPS spectra fitted parameters for all NiO/VGN systems. . . . .	117

# Chapter 1

## Introduction

Life exists in the universe only because the carbon atom possesses certain exceptional properties.

-James Jeans

### 1.1 Two-dimensional carbon

Graphene is a two-dimensional allotrope of carbon, having monoatomic thick hexagonal (honeycomb like) lattice structure with a carbon-carbon distance of 1.42 Å. In other words, it is a single layer of graphite having  $sp^2$  hybridized carbon atoms (Figure 1.1(a)) [1]. In 2010, Andre K. Geim and Konstantin S. Novoselov were awarded Nobel prize for their "groundbreaking experiments regarding the two-dimensional material graphene" [1, 2]. They successfully synthesized graphene film for the first time using a mechanical exfoliation method with scotch tape and the silicon substrate. Graphene is the first two-dimensional atomic crystal and it is the representative of other two-dimensional materials such as transition metal oxides, sulphides and boron nitride [3, 4].

Graphene shows  $sp^2$  hybridization with  $\sigma$  and  $\pi$  bonds perpendicular to each other (Figure 1.1(b)). The strong *in-plane*  $\sigma$  bonds work as the rigid backbone of the hexagonal structure and the *out-of-plane*  $\pi$  bonds control interaction between different graphene layers [5]. The primitive lattice of honeycomb lattice structure of graphene can be viewed

as a triangular Bravais lattice with a two-atom basis (A and B) as shown in figure 1.1(a). The three vectors  $\delta_1$ ,  $\delta_2$  and  $\delta_3$  connect a site on the A sublattice with nearest neighbours on the B sublattice and the triangular Bravais lattice is spanned by the basis vectors ( $\mathbf{a}_1$  and  $\mathbf{a}_2$ ) [6].

Due to its outstanding properties, graphene grabbed a tremendous scientific and technological interest in recent years. The properties are listed below,

A. Intrinsic (undoped) graphene is a semi-metal or zero-gap semiconductor (Figure 1.1(c)).

The interesting transport properties of graphene are due to the dispersion around the K points. So, the charge carriers in graphene can be treated as massless Dirac particles and hence excellent electronic property due to high charge carriers (electrons and holes) mobility  $230,000 \text{ cm}^2 \text{ V}^{-1} \text{ s}^{-1}$  at room temperature [7].

B. Thermal conductivity of  $5,000 \text{ W m}^{-1} \text{ K}^{-1}$  due to strong C-C covalent bonds and less phonon scattering [8].

C. Mechanical stiffness of 1 Tpa. The origin of this strength lies in the  $\sigma$  bonds which connect the carbon atoms in a honeycomb packed structure [9].

D. High surface area which is theoretically predicted to be  $2,600 \text{ m}^2/\text{g}$  [10].

E. Graphene is also a transparent material which only absorbs 2.3 % light of the optical region [11].

The largest known allotrope of carbon is 3D graphite and due to its softness and dark color, it was considered as lead (Pb) like material for a long time. Graphite is a stacking of graphene sheets (Figure 1.1(d)) that stick together due to the Van der Waals interaction, which is much weaker than the *in-plane* covalent bonds. Carbon nanotubes, the 1D allotrope, may be viewed as graphene sheets that are rolled up (Figure 1.1(d)), with

a diameter of several nanometers. The 0D graphitic allotrope is fullerene, the prominent representative is  $C_{60}$  molecule which has the form like a football and is also called 'buckyball'. It consists of a graphene sheet, where some hexagons are replaced by pentagons, which cause a crumbling/wrapping of the sheet and forms a graphene sphere.

Thus, graphene is the basic building block of all other graphitic materials. By stacking, rolling and wrapping, graphene can transform into graphite (3D), carbon nanotube (1D) and fullerene (0D), respectively [12].

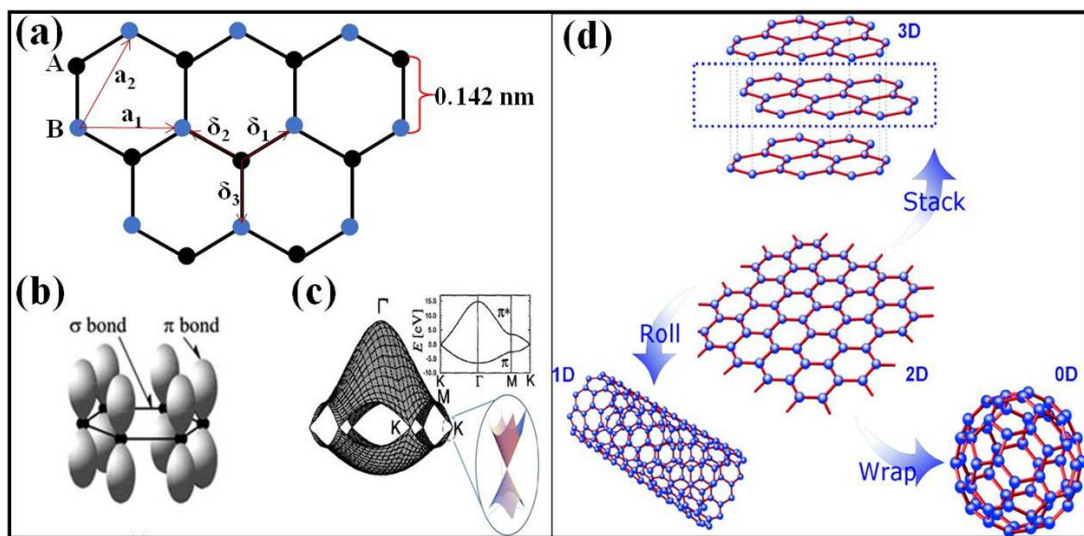


**Figure 1.1** – (a) Graphene crystal structure, (b) schematic of *in-plane*  $\sigma$  and perpendicular  $\pi$  bonds, (c) band-energy diagram of graphene and (d) graphitic allotropes: layered 3D structure of graphite, 0D allotrope:  $C_{60}$  molecule fullerene, 1D allotrope: single-wall carbon nanotube.

The monolayer graphene has been classified based on variations in layer number, lateral dimension and chemical modification. According to this graphene family is classified into: [13, 14]

**Graphene:** a single-atom-thick sheet of hexagonally arranged,  $sp^2$ -bonded carbon atoms. Depending on the number of layers ( $n$ ), planar graphene is classified into bilayer graphene ( $n=2$ ), trilayer graphene ( $n=3$ ), few layer graphene ( $2 < n < 5$ ) or multilayer graphene ( $5 < n < 10$ ).

**Graphene quantum dots (GQDs):** GQDs have microscopic lateral dimensions  $< 10$

nm, which is used in a study like photoluminescence.

**Graphene oxide (GO):** is chemically modified graphene prepared by oxidation and exfoliation *i.e* accompanied by extensive oxidative alteration of the basal plane. Graphene oxide is a monolayer material with a high oxygen content, typically characterized by C/O atomic ratios.

**Reduced graphene oxide (rGO):** is graphene oxide that has been reductively processed by chemical, thermal, microwave, photo-chemical, photo-thermal methods to reduce its oxygen content.

**Graphene nanoribbon:** a single atom thick strip of hexagonal,  $sp^2$  bonded carbon atoms. To be considered as ribbon, the longer lateral dimension should exceed the shorter lateral size by at least an order of magnitude.

**Graphene nanosheet:** a single or few-layer graphene sheets of hexagonally arranged,  $sp^2$  bonded carbon atoms is freely suspended or adhered to a foreign substrate. The orientation and arrangement of the graphene nanosheets will give additional applications to the material.

## 1.2 VGN and its properties

Vertical graphene nanosheets (VGN) is a 3D porous network of inter-connected graphene nanosheets oriented perpendicularly to the substrate [15]. VGN is also known as carbon/graphene nanowalls [16, 17], carbon/graphene nanosheets [15, 18], carbon/graphene nanoflakes [19] and carbon nanoflowers [20]. The sheets are self-supported wall structures with lateral and vertical dimensions of 0.1 to tens of micrometers and a thickness of few nanometers [21]. Each sheet consists of 1-10 number of graphene layers and of 0.34 nm inter-layer spacing [22]. The unique structure of VGN (schematic shown in figure 1.2) possesses amazing properties.

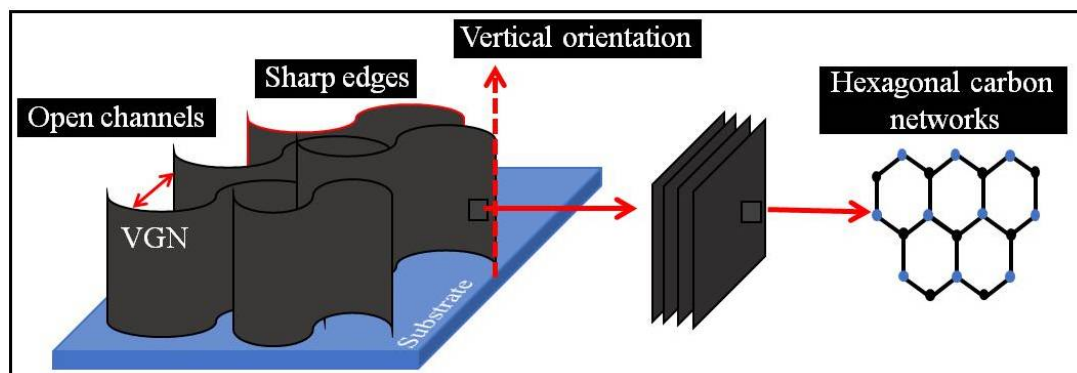


**Figure 1.2** – Schematic representation of VGN structure and its amazing properties.

The vertical orientation on the substrate is the first unique property of VGN, which gives mechanical stability to the structure. This vertical orientation represents a free-standing self-supported structure, which provides rigidity otherwise the structure would collapse. This aligned structure also enables the improvement in electrochemical and electronic applications as both surfaces are actively taking part in the reaction. [23, 24].

Second, VGN is a non-agglomerated morphology with a high surface area nearly  $1800 \text{ m}^2/\text{g}$  [25] and contains open channels between sheets. It is possible to vary the inter-sheet distance from few tens to hundreds of nanometers by changing the growth parameters [16, 26]. Due to this property, the entire surface can easily be accessed by the molecules or ions, which is crucial for enhanced gas sensing and electrochemical capacitor applications [24].

The third feature of VGN is long, exposed, thin and reactive edges. The thickness reduces from few-layered graphene sheets at the base to atomically thin at the top. These active edges boost the electrochemical activity, sensing and field-emission. Also, the functional groups attached to the active edges decide the wetting nature [27, 28]. Generally, the VGN surface is terminated by C-H groups and thus hydrophobic in nature. The water contact angle of VGN is found to be  $130\text{-}140^\circ$ . Fourth, the VGN sheets consists of graphene networks, so gives high *in-plane* electrical conductivity [29].

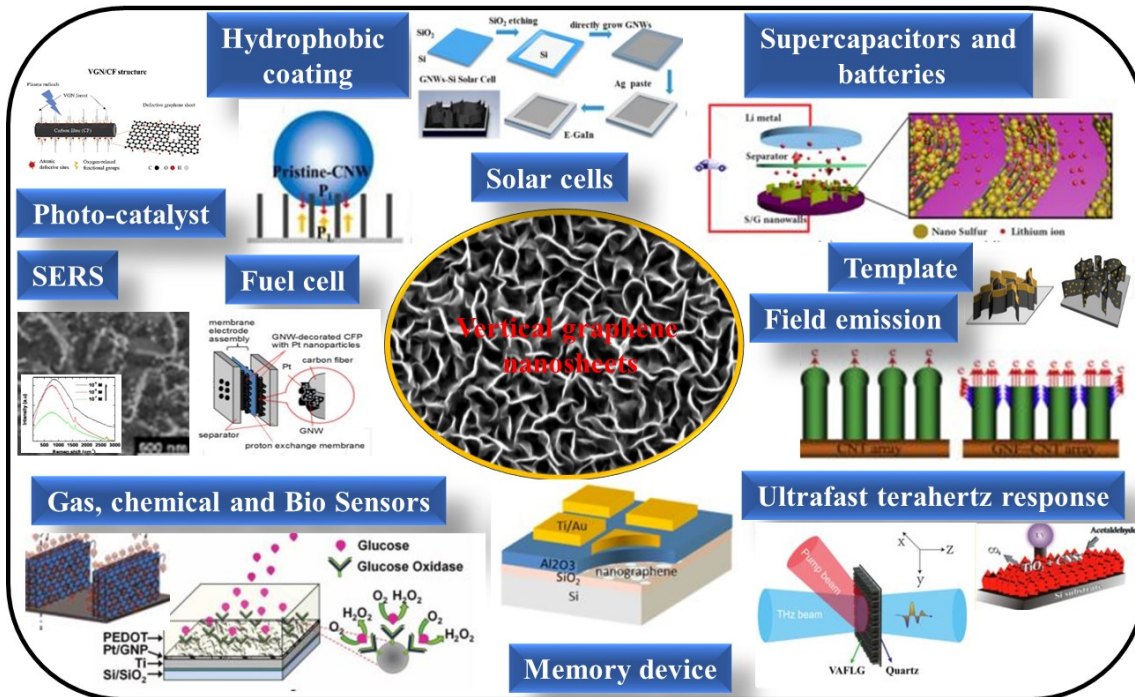


**Figure 1.3** – Schematic of various applications of VGN (images are taken from the corresponding references given in text).

These unique properties make VGN stable and attractive for many applications like electrochemical capacitors [18], batteries [30], fuel cells [31], solar cells [32], field emission [33], gas, bio and chemical sensors [34, 35], ultrafast terahertz response photoelectric device [36], ac line filtering [37], hydrogen absorption [38], black body coating [39], spintronics [40], hydrophobic coatings [41], photo-catalytic activity [42], template for other material growth [43], surface enhanced Raman spectroscopy [44] and memory devices [45]. The schematic in figure 1.3 illustrates various possible applications of the VGN.

Carbon materials in their different forms, such as graphene, carbon nanotubes (CNT) and activated carbon (AC), have emerged as promising electrode materials for supercapacitors due to their excellent electrical conductivity, high surface area, low cost, abundance and chemical stability. Graphene has a high theoretical surface area around  $2630 \text{ m}^2/\text{g}$  and capacitance is up to  $550 \text{ F/g}$  with the utilization of the entire surface [46]. Unlike other carbon materials such as activated carbon, carbon nanotube, etc., graphene doesn't de-

pend on the distribution of pores [47]. Graphene oxide is also used as electrode materials, though it agglomerates upon mixing with the binder.

On the other hand, CNT, categorized as single-walled carbon nanotubes (SWCNTs) or multi-walled carbon nanotubes (MWCNTs), are explored as supercapacitor electrode materials due to their excellent electrical conductivity and large accessible surface area [48]. Additionally, they provide a adequate support for other active materials due to their high mechanical strength and open tubular network.

However, the most widely used supercapacitor electrode material is AC due to its large surface area, good electrical properties, availability, easy synthesis procedure and moderate cost. The activation methods and carbon precursors used for the growth of AC possess surface area up to  $3000 \text{ m}^2 \text{ g}^{-1}$ . The porous structure of AC obtained from different synthesis procedure has a broad pore size distribution that consists of micropores ( $<2 \text{ nm}$ ), mesopores ( $2\text{-}50 \text{ nm}$ ) and macropores ( $>50 \text{ nm}$ ). Also, the pore size distribution of AC plays a vital role in the capacitor performance in addition to its high surface area [49]. Additionally, excessive activation results in large pore volume, which leads to low conductivity and reduction in material density, resulting in low energy density and loss of power capability.

Recently, the VGN, a new derivative of graphene found to be an excellent supercapacitor electrode material due to its unique morphology in combined with the remarkable properties of graphene. VGN electrodes' advantage is that they do not need any binders for electrode fabrication, whose main drawback is reducing the active surface area. Further, the advantage over activated carbon is its capacitive behavior at high-frequency [37]. Thus, the current thesis work is mainly focused on the electrochemical capacitor/supercapacitor application of VGN.

### 1.3 Electrochemical capacitors

Electrochemical capacitors (ECs), supercapacitors (SCs) or ultracapacitors are high capacity capacitors with superior capacitance than that of electrostatic capacitors [50].

Conventional or electrostatic capacitors are energy storage devices that store electric charges in an electric field. A capacitor consists of two metal plates separated by a non-conducting material or an insulating dielectric material. The charged electrodes polarize the dielectric material and its electric field is in the opposite direction to the field produced by the charged electrodes (Figure 1.4). Capacitance is generally defined as the ratio of accumulated charge  $Q$  at the electrode, and the potential difference  $V$ , between electrodes i.e.,  $C = Q/V$  [50].

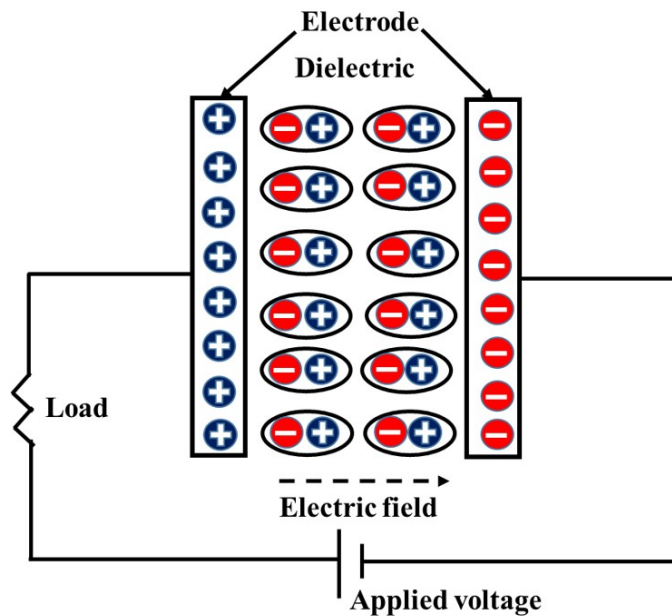


**Figure 1.4** – Schematic of a conventional/electrostatic capacitor.

The capacitance of a parallel plate capacitor is given by the equation 1.1 [50]:

$$C = \epsilon_0 \epsilon_r (A/d) \quad (1.1)$$

where,  $A$  is the area of the charged electrodes,  $d$  is the distance between them,  $\epsilon_0$  is the dielectric constant of free space and  $\epsilon_r$  is the relative dielectric constant of the insulating material between the electrodes. The dielectric constant ( $\epsilon$ ) is the product of  $\epsilon_0$  and  $\epsilon_r$ .

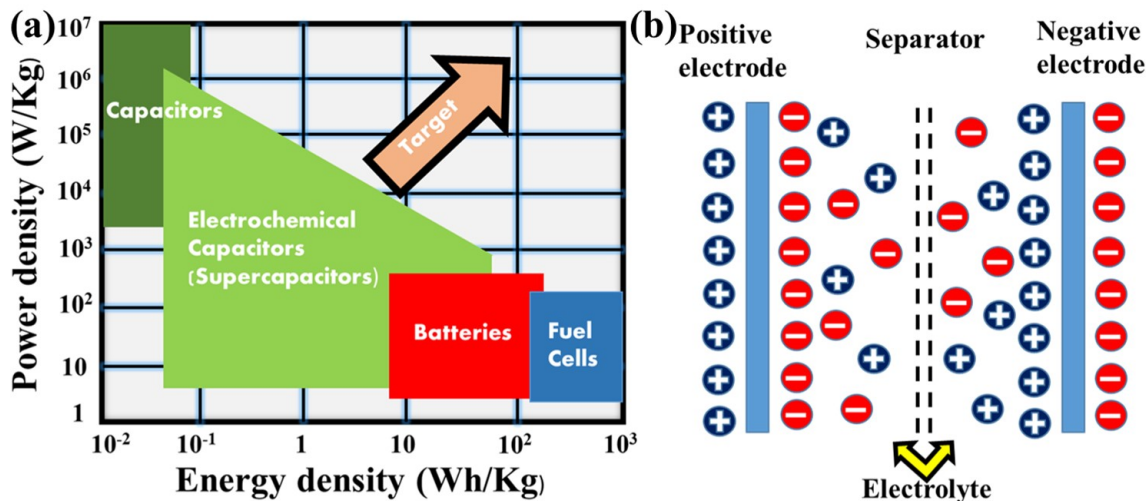
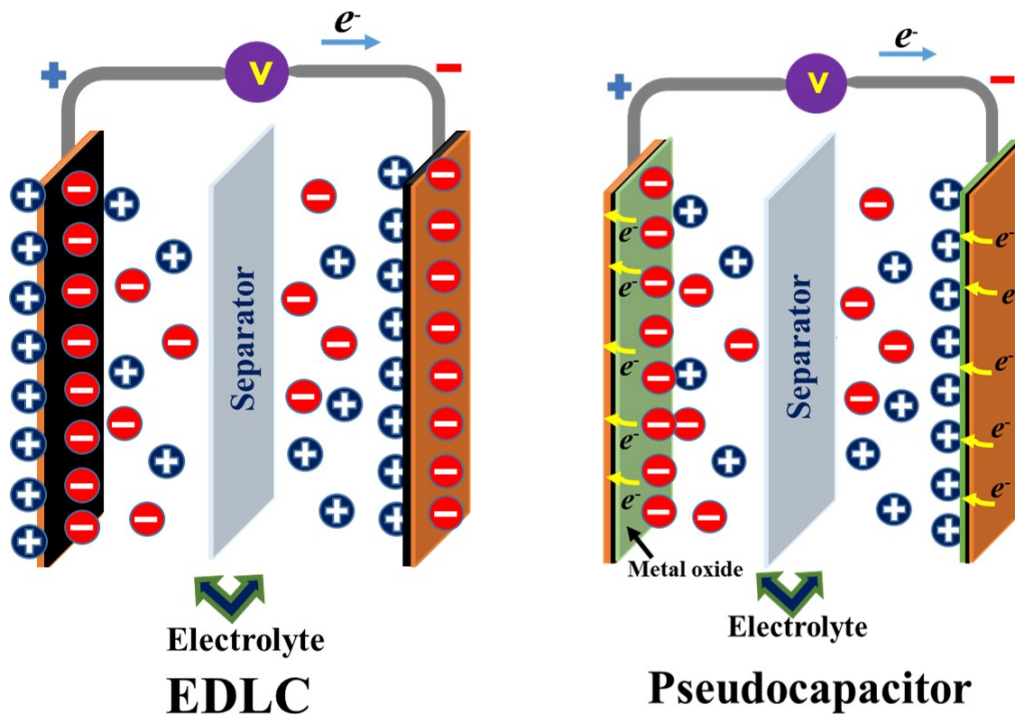


Figure 1.5 – (a) Ragone plot and (b) schematic of the a typical supercapacitor.

To achieve higher capacitance, larger dielectric constants and high surface area are required. The energy density (total energy storage in the device) and power density (time rate of energy transfer) are the two factors that decide the performance of the energy storage devices. Electrostatic capacitors are having high power density and less energy density. Whereas, the batteries are just the opposite and have high energy density and low power density. Supercapacitors are the devices bridges the energy gap between the capacitors and batteries and have high energy and power density [51]. Energy and power density depends on the electrode material's active surface area and electrical conductivity. So, graphene materials are mostly used as the supercapacitor electrode material. Ragone plot of energy density vs. power density for various energy storing devices is shown in figure 1.5(a) [50, 52, 53].

A general electrochemical capacitor consists of two electrodes (positive and negative) separated by a separator and electrolyte. The electrolyte acts as a reservoir of ions in the matrix. Schematic of the configuration for a electrochemical capacitor is shown in



**Figure 1.6** – Schematic of EDLC and pseudocapacitance charge storage.

figure 1.5(b). There are two mechanisms that contribute to the large capacitance in supercapacitors: the electrical double layer capacitance (EDLC) and pseudocapacitance [50, 52]. The EDLC is due to the charge separation at the electrode-electrolyte interface and the capacitance originates due to the charge transfer between the electrolyte/electrode is called pseudocapacitance. The latter is attributed to reversible redox processes [52]. Schematic of the charge storage mechanism is shown in figure 1.6.

### Electric double layer capacitance

In the case of EDLC, the charge is stored at the electrode-electrolyte interface by the electric-double layer mechanism. The charge separation occurs at a distance of 0.3-0.8 nm. Here, the current is independent of potential, as the charge separation is due to the coulombic interaction, once the charge accumulation occurs, further increase in potential does not affect the current.

The EDL concept was first described and modeled by von Helmholtz in 19<sup>th</sup> century, when he investigated the distribution of opposite charges at the interface of colloidal particles

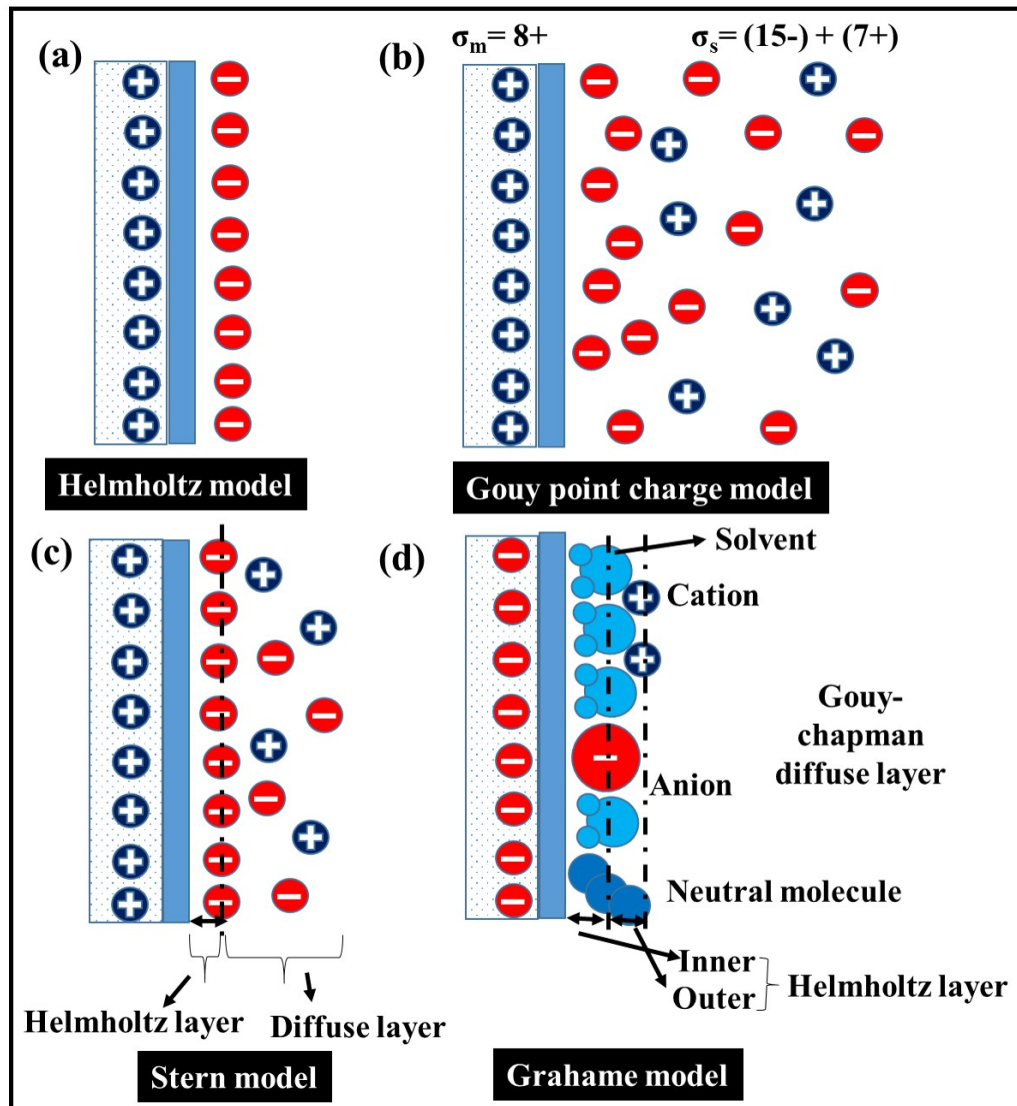


Figure 1.7 – Schematic of the electric double layer charge storage mechanisms.

[54]. The concept of a double layer corresponds to a model consisting of two array layers of opposite charges, separated by a small distance having atomic dimensions (Figure 1.7(a)). It was then realized that ions on the solution side would not remain static in a compact array due to the thermal fluctuation according to the Boltzmann principle. Gouy introduced the thermal fluctuation factor and represented the 3D diffusely distributed population of cations and anions (Figure 1.7(b)). The capacitance associated with this model is commonly referred to as the 'diffuse' double-layer capacitance. The failure of the Gouy-Chapman model is due to the assumptions that ions are assumed to be point

charge. It gives an incorrect potential profile and a local field near the electrode surface [55, 56].

Stern model: Stern combined both these models and the charge distribution was recognized by the inner region of the ion distribution due to the adsorption process and the region beyond the inner layer could be validly treated in terms of a diffuse region distributed ionic charge Figure 1.7(c) [57]. If the ions were recognized as having a finite size, including the annular thickness of their hydration shells, it was easy to define a geometrical limit to the compact region of ions' adsorption at the electrode surface. This corresponds to a Helmholtz type compact double layer having capacitance  $C_H$  and the remaining diffusion layer having capacitance  $C_{diff}$ . So overall capacitance  $C_{dl}$  [58],

$$1/C_{dl} = 1/C_H + 1/C_{diff} \quad (1.2)$$

where,  $C_H$  depends on the electrode potential and  $C_{diff}$  is on the electrolyte concentration. So introducing a distance of the closest approach of finite size ions, the high capacitance arises in the Gouy-Chapman treatment is automatically avoided.

Grahame model: This model gives an important distinction between the inner and outer Helmholtz layer in the interphase, which correspond to the different distances of the closest approach for anions and cations at the electrode surface Figure 1.7(d) [50, 58]. In general, cations are smaller than anions and retain solvent shells due to strong ion-solvent dipole interaction. Grahame model consists of three regions: the inner Helmholtz layer, outer Helmholtz layer and diffuse ion distribution layer. As the anion distance of closest approach is smaller than the hydrated cations, the positive charge electrode's inner layer capacitance is usually twice than that of negative charge electrode.

### **Pseudocapacitance**

Pseudocapacitance (PC) stores electric charges through Faradic redox reactions that in-

involve chemical reactions [50]. As the redox reactions are potential dependent, the current continuously changes with potential. Due to the functional groups present on the surface, there is approximately 1-5 % pseudocapacitance in a typical double-layer carbon capacitor. Several types of materials with significant pseudocapacitance have been investigated: a) electroactive transition metals oxide/hydroxides, such as  $\text{MnO}_2$ ,  $\text{IrO}_2$  and  $\text{RuO}_2$ , and b) conducting polymers, e.g., polypyrrole, polythiophene, polyaniline, and their derivatives [50]. From the charge storage mechanism, the PC normally exhibit higher capacitance but weaker cyclic stability than that of EDLC. So, recently the interest of the scientific community is to combine both porous carbon materials and transition metals into the same electrode (called a hybrid electrode) to exploit both the large surface area of porous electrodes and the higher capacitance of the transition metals to enhance both capacitance as well as cyclability.

Due to these properties, SC finds many applications in the field of energy storage, flexible energy devices, memory backups, automobiles and railways [59, 60]. These applications demand supercapacitor electrode material with high energy density and power density and the flexible electrode is needed for the flexible energy storage devices [53]. Towards this, recently VGN and VGN based hybrids/composites are used in electrochemical capacitors. It is reported that VGN-based EDLCs exhibited a capacitance of nearly  $0.32 \text{ mF/cm}^2$  at 1 kHz, higher than the reported values of EDLCs at the same frequency [61]. Further, The capacitive behaviors of VGN can be enhanced by tuning their morphology and structure. The specific capacitance can be improved by using the VGN-based hybrid structures, e.g., CNT on VGN [62]. Such a combination of 1D and 2D nanostructures further increase the surface area and enhance the electron transport within active materials, leading to a high specific capacitance ( $278 \text{ F/g}$  at  $10 \text{ mV/s}$ ) and good cyclic stability (99 % capacitance retention after 8000 charge-discharge cycles) [62]. Electrochemical capacitor properties of pseudocapacitors based on hybrid  $\text{MnO}_2$ -VGN can compete with

those of EDLC. At a CV scan rate of 10 mV/s, the MnO<sub>2</sub>-VGN electrode is reported to have a high specific capacitance of 1060 F/g [63]. Hierarchical electrodes composed of carbon cloth (CC), VGN and conducting polyaniline (PANI) can further improve the EC performance. At a scan rate of 2 mV/s, the specific capacitance of the CC/VGN/PANI electrode is three times higher than that of the CC/PANI electrode. The CC/VGN/PANI electrode presented a specific capacitance of 2000 F/g [64].

The rapid growth of the popularity of wearable electronics in the past decade has resulted in a strong interest in flexible electronics [65]. Presently, the most commonly employed approach for the transfer of graphene and 2D transition metal dichalcogenide layers relies on the chemical etching of underlying growth substrates and involves protection polymers [66, 67]. Although ECs are available commercially, there is still a need for further improvement of some critical characteristics such as specific capacitance, rate capability, as well as power and energy densities. Also, there is a need for a polymer-free transfer process to retain the morphology of VGN for the fabrication of a flexible electrode. Hence, the motivation of the thesis is to develop VGN based flexible electrode and to enhance the capacitance and extending the potential window of the VGN electrode to increase the energy density without deteriorating the morphology of the structure.

## 1.4 Difficulties in the polymer based transfer process

VGN is an emerging electrode material for the supercapacitor electrode and there is a need for transferring the VGN onto flexible electrodes for flexible electronics applications. However, the high growth temperature (800 °C) of the VGN restricts their direct growth on the flexible substrate as they can't withstand the high temperature. Till now, the lowest growth temperature demonstrated for VGN growth is 225 °C [68]. The general methods used for the transfer are laser-induced transfer technique and polymer-based

transfer process.

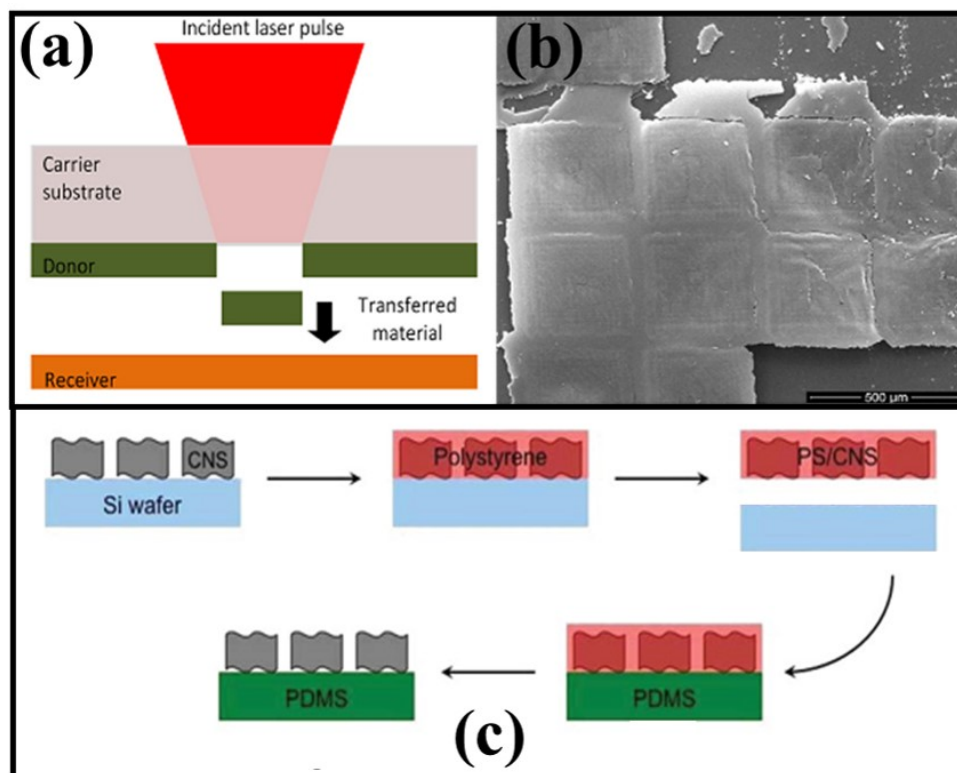


**Figure 1.8** – (a) Schematic of the LIFT technique, (b) Shows the damaged structure after the LIFT transfer and (c) schematic of the polymer based transfer process. Pictures are taken from the literature discussed in text.

The laser-induced forward transfer (LIFT) technique was reported by Constantinescu *et al.*, [69, 70] where, a laser beam is focused on the transparent donor which cut, eject and print pixels/droplets of the films in the desired pattern (Figure 1.8(a)). However, LIFT has the main disadvantage that it damages the sample and needs special handling skills (Figure 1.8 (b)). Quinlan *et al.*, [71] has developed a two-step polymer-based chemical transfer process in which the VGN is spin-coated with polystyrene (PS) solution followed by transfer onto a suitable polydimethylsiloxane (PDMS) substrate. The schematic of the transfer process is shown in figure 1.8 (c). The polymer used in the transfer process is removed by using methyl ethyl ketone (MEK) and N-methyl-2-pyrrolidone (NMP) solvents. This method involves several chemical processes, which can degrade the morphology, sur-

face chemistry, and structure. Also Kim *et. al.*, [67] has developed a two-step chemical process for transferring CVD grown single-layer graphene grown on a metal substrate (Ni) to an insulating substrate. These processes has a difficulty in removing the polymer layer without damaging the graphene morphology. The water soak and peel delamination transfer method is demonstrated to avoid the Ni etching [72]. However, the problem associated with removing polymethyl methacrylate (PMMA) polymer still remains. Since VGN itself is a porous network, the polymer coating can fill the pore structure and it will be much more difficult to remove, unlike in the case of horizontal graphene transfer. Further, VGN is easily peelable, and hence it can be easily damaged. Hence, one should consider the bottom-substrate etching-transfer technique with a slow etching rate, so that the film does not experience any kind of disturbance.

## **1.5 Surface modification: a strategy to enhance electrochemical capacitance**

The second motivation of the thesis is focused on the enhancement of the capacitance of VGN based electrode without alteration of its morphology. The surface of VGN mostly takes part in the electrochemical reaction, hence its suitable modification can enhance the capacitance. The surface modification is carried out in three ways to enhance the capacitance.

### **Plasma activated surface modification**

The 3D interconnected porous network of VGN structures provides easy access to its surfaces on both sides of the sheets for the electrolyte ions to interact, which is an advantage for its application as a supercapacitor electrode material [73, 74]. Further increase in the surface area of VGN can be achieved by changing the inter-sheet distance and by producing secondary walls [75, 76]. The as-grown VGN is hydrophobic due to its interconnected

porous 3D network and hydrogen-terminated edges [27, 28]. The hydrophobic surfaces are the most suitable applications in the field like anti-icing, anti-corrosion, self-cleaning and anti-fogging coatings. Whereas the hydrophobic nature restricts the electrolyte access to the entire surface area for EDL formation. Hence, the transformation of VGN surface to hydrophilic, while retaining its unique morphology is in high demand for high-performance EC applications [77, 78]. The nature and density of defects, inter-sheet spacing and surface functionalization play vital role in deciding the wetting nature of VGN structures [28, 41, 77, 79–82]. Surface modification methods like chemical activation and post-plasma treatment were widely adopted to tune the wetting properties of nanostructures [78, 82, 83]. However, chemical activation is time-consuming and there is a possibility of damaging the morphology [84, 85]. Also, in this process it is very difficult to achieve super-hydrophilic surfaces [85, 86]. Whereas, post-deposition plasma treatment is fast and helps in preserving the morphology.

In the recent past, the post-deposition plasma treatment of carbon nanostructures gained a lot of attention for tuning the surface functionalizations and wettability. The plasma treatment under different plasma mediums like oxygen, hydrogen, nitrogen, fluorine and argon was studied to tune the wetting nature of VGN [79, 82]. Amongst, surface fluorination makes VGN super-hydrophobic and exposure to all other plasmas (hydrogen, nitrogen, argon and oxygen) results in hydrophilic surfaces. A recent study by Vizireanu *et. al.*, [87] reported, growth of super-hydrophilic carbon nanowall, which is different from the most commonly reported intrinsic hydrophobic VGN. But they observed that the hydrophilicity of these carbon structures sustain only for a short time (3-6 days) and then transformed into highly hydrophobic. Furthermore, a few studies confirm that the oxygenated functionalization improves the electrochemical capacitor performance [88, 89]. Whereas, Belova *et.al.*, [90] reported that the oxygen surface functionalization causes low discharge current densities and poor cyclability for battery operation. It is attributed to

the slow oxygen reduction and evolution reaction kinetics and complex multistep reaction pathways. However, O<sub>2</sub> reduction on graphite is found to be influenced by the nature and concentration of active surface groups [91]. Additionally, there are reports on the attachment of specific types of oxygenated functional groups (hydroxyl and carbonyl) found to enhance the EC performance of graphene sheets [88]. Nevertheless, no specific studies on functionalizing VGN surfaces with selective oxygenated groups (hydroxyl or carbonyl) and evaluation of their capacitor performance exist. Also, the stability of the hydrophilic surface has a significant impact on their supercapacitor performance, since the electrode surface is the active participant in the formation of EDLC. As plasma-based surface modification is a non-equilibrium process, studies on the long-term stability of the plasma-induced changes in wettability are need of the hour for potential utilization of the VGN electrodes for supercapacitor applications.

### **Metal/metal oxide nanoparticle decoration**

An improvement in the charge storage capacity of graphene structures by different methods has gained a lot of attention. Numerous methods, like changing wettability [92–94], doping by nitrogen and oxygen [95, 96], polymer coating [64], use of an organic and ionic electrolyte [97, 98] and designing symmetric and asymmetric SC [99], were tried to enhance the capacitance performance of carbon nanostructures. Amidst, hybrid graphene structures decorated with transition metal nanoparticles (NPs) exhibited significant improvement in specific capacitance [100, 101]. It is expected that VGN with a homogeneous decoration of metal NPs will also improve its conductivity and facilitate an easy ion insertion and extraction into the structure. He *et al.* [102] reported that the mismatch in work function between graphene and Ag NPs resulted in a lower resistivity, which is attributed to the increase in carrier concentration of the composite. The charge transfer due to the adsorption of metals NPs on graphene and the metal NP's electrochemical performance decorated carbon nanostructures are reported independently [103, 104]. However, litera-

ture reports on correlating the electrochemical capacitance performance with the charge transfer process are missing.

Also, the researchers focused on exploiting the synergistic effect of both EDLC and PC, by growing hybrid structures of carbon and metal, metal oxides/hydroxides composites [105, 106]. High demand for enhancing the capacitance performance of VGN, entails the growth of VGN based hybrid structures. Variety of metal oxides including  $\text{MnO}_2$ ,  $\text{RuO}_2$ ,  $\text{SnO}_2$ ,  $\text{NiO}$ ,  $\text{Fe}_2\text{O}_3$  and  $\text{Co}_3\text{O}_4$  are used to decorate on VGN structures and their capacitor performances were studied [25, 107–109]. Most of these oxides suffer from high cost, low electrical conductivity, and poor cyclability. The electrochemical performance of some effective metal oxide decorated VGN hybrid structures need to be studied.

### **Hybrid electrolyte with surface activation**

Although the electrode material is crucial, some critical issues for the electrode materials are stability, electrical conductivity, agglomeration, need of binder and current collector [110–112]. Like electrodes, the choice of electrolyte and its concentration play a vital role in capacitor performance. The device's potential window also strongly depends on the electrolyte and its nature of interaction with the electrode material.

Since the VGN are proven to be promising supercapacitor electrode materials, researchers focused on finding a potential electrolyte. Recently, thorough investigation of aqueous electrolytes ( $\text{Na}_2\text{SO}_4$ ,  $\text{H}_2\text{SO}_4$ , and  $\text{KOH}$ ) has demonstrated their suitability to use with VGN [78]. The water-based electrolytes are environmental friendly, safe, and cost-effective. Still, the limitation of the aqueous electrolyte's narrow operational potential window needs to be overcome to develop a high-performance SC device. Even then, the demand for high energy storage capacities propels the research activities to focus on novel electrolytes for further enhancement of capacitance [112]. At present, a lot of research is being focused on organic electrolytes and ionic liquids because of their extended operating potential windows [112, 113]. Recently, considerable attention is devoted to the

use of novel electrolytes in innovative ways. Besides the use of aqueous, organic, or ionic electrolytes, a great deal of research is concentrated on hybrid electrolytes for improving the SC performance. For example, acetate aqueous electrolytes [114], isopropanol added aqueous electrolytes [115], aqueous solution of acidic ionic liquid [116], ionic liquid-added polymer electrolytes [117], and hydro-quinone doped hybrid gel electrolytes [118] are opted for enhanced stability over an extended potential window. It is reported that with an addition of  $10^{-4}$  M KOH to 1M  $\text{Na}_2\text{SO}_4$  electrolyte solution, an extended potential window of 1.07 V was achieved for the VGN electrode [93].

Additionally, the whole electrode surface coverage with an electrolyte also has a crucial role in determining the SC performance. It is mainly controlled by the wetting nature of the electrode surface. Porous carbon nanomaterials including, VGN are, in general, hydrophobic [119] and in this context, hydrophilic electrode materials are more beneficial. The electrode's wetting nature can be altered by surface functionalization, which is another strategy towards improving SC performance [88]. Functionalization by a polar group is used to enhance the wetting nature of the electrode materials. However, the functionalization process should not deteriorate the structure of the electrode. It is reported that KOH is widely used for the activation of graphene oxides and activated carbon to improve SC performance [47, 120, 121]. Also, the chemical activation process by KOH is reported to generate nanoscale pores in carbon nanostructures [121]. Recently, better wetting nature is found for VGN in the 1M KOH medium, leading to a higher capacitance value [78]. Hence, the supercapacitor performance of KOH activated VGN can be studied in a hybrid electrolyte.

Our endeavor here is to combine a novel electrolyte and chemical activation of the electrode surface towards achieving enhanced SC performance.

## 1.6 Research objectives and overview of the thesis

Electrochemical capacitor/supercapacitors are a potential substitute to the conventional batteries for energy storage applications due to their longer cycle-life, high charge-discharge rate and superior power density [53, 122]. However, the poor energy densities limit their commercial utilization and hence, the improvement of energy density for supercapacitors is of high demand. The carbon nanostructures are considered ideal for EDLC and metal oxide/hydrides and nitrides are for pseudocapacitor. Amongst carbon nanostructures, the VGN, a derivative of graphene and an ensemble of vertically standing few-layer graphene sheets of few tens of nanometer-thick, has drawn significant attention of the research community due to its remarkable properties [15]. The VGN has a theoretical charge storage capacity of around  $1.49 \times 10^4$  F/cm<sup>2</sup>, as reported by Zhao *et. al.*, [18]. In contrast, the reported SC values for VGN are found to be in the range of micro to few milli Farad range only. Hence, it offers to improve the charge storage capacity of graphene structures, gained a lot of attention. To increase the energy (E) stored in electrochemical capacitors, we can either increase the capacitance (C) or the operating voltage (V) of the device. The capacitance can be increased by increasing the surface area by surface modification, which allows efficient electrolyte penetration and results in good contact with active sites on the entire surface of the porous electrode. The operating voltage can be increased by adding carbon materials to transition metal electrodes, fabricating asymmetric supercapacitors, changing electrolyte, and connecting several supercapacitors in series. Also, there is a need of the flexible electrodes for flexible electronics applications. Thus, the prime focus of this thesis is to enhance the capacitance by surface modification (plasma activation and metal/metal oxide decoration) of the VGN, while retaining its unique geometry. An effort is made to understand the role of surface functionalization and charge-transfer on the capacitance performance. Further, the capacitance performance of KOH activated

VGN is studied by using a hybrid electrolyte (tetra ethylammonium tetrafluoroborate + sulfuric acid). Also, a simple and polymer-free transfer process is established for the development of VGN based flexible supercapacitor.

The present thesis comprises of seven chapters and the outline of each chapter is as follows:

**Chapter 1** introduces the structure and unique properties of the vertical graphene nanosheets and basic concepts of the electrochemical capacitor (EDLC and PC). An up to date literature survey of the VGN electrode for electrochemical capacitor application is included. This chapter also discusses the need for a polymer-free transfer process towards the development of flexible supercapacitors and the surface modification to enhance specific capacitance. The focus on development of VGN and metal/metal oxides based hybrid electrodes with enhanced capacitance is also discussed. The synergistic effect of both EDLC (from VGN) and pseudocapacitance (from metal/metal oxide) of the hybrid electrode for achieving the enhanced capacitance is described. Further, the chapter also briefs about the importance of hybrid electrolytes on capacitance performance.

**Chapter 2** provides a brief description of the growth techniques used for the synthesis of VGN, surface modification/activation of VGN and metal nanoparticle decoration on VGN. It also discusses, the characterization techniques such as scanning electron microscopy (SEM), transmission electron microscopy (TEM), X-ray photoelectron spectroscopy (XPS) and Raman spectroscopy employed to investigate the morphological, chemical and structural properties, respectively. A detail description about the contact angle measurement and four-point probe method for electrical resistance measurements are presented. A brief introduction to electrochemical measurement, principles for cyclic voltammetry, galvanostatic charge-discharge curve and electrochemical impedance spectroscopy (EIS) are also presented.

**Chapter-3** describes an easy, scalable and polymer-free transfer process for the successful transfer of the VGN onto flexible substrates. Additionally, this process retained the much-needed morphology of the VGN. To ascertain the retention of the structure and morphology, the charge storage performance is evaluated by fabricating a flexible symmetric supercapacitor device using the transferred VGN electrodes free of binder and current collector. The device possesses a capacitance of  $158 \mu\text{F}/\text{cm}^2$  with 86 % capacitance retention after 10,000 charge-discharge cycles are observed.

In **chapter-4**, super-wetting VGN structures are achieved by oxygen plasma treatment, while retaining its morphology. The enhanced charge storage performance of super-wetting VGN structures from  $0.15$  to  $1.7 \text{ mF}/\text{cm}^2$  is demonstrated. Further, *ex-situ* or *in-situ* plasma treatment is carried out, to obtain VGN structures with preferential functionalization by specific type of oxygenated groups. Moreover, the correlation between the type of oxygen functional groups (hydroxyl, carbonyl and carboxyl) with wetting nature, temporal stability of wettability and supercapacitor performance of VGN surfaces is established. The capacitance performance of VGN samples undergone oxygen plasma treatment is also compared with the ones treated with  $\text{H}_2$  and  $\text{N}_2$  plasmas. The significant role of process parameters towards achieving hydrophilic VGN surfaces with long-term stability is brought out. Finally, a device of solid-state symmetric supercapacitor is fabricated and used to light up a blue light-emitting-diode to demonstrate its practicability.

**Chapter-5** is focused on the influence of the transition metal NP (Au, Ag, Cu and Ni) decoration of a VGN structure on its capacitance performance. The energy storage performance is correlated with the charge transfer resulted due to the mismatch in the work function. Amongst, the Ni decorated VGN exhibited highest charge transfer ( $+0.48 e$ ) and capacitance ( $3.04 \text{ mF}/\text{cm}^2$ ). Further, the metal oxide ( $\text{NiO}$  and  $\text{TiO}_2$ ) nanoparticle decoration of VGN is carried out and studied their capacitance performance.

The **chapter-6** demonstrates a novel approach based on the combination of surface activation and utilization of an organo-aqueous hybrid electrolyte, tetraethylammonium tetrafluoroborate (TEABF<sub>4</sub>) in H<sub>2</sub>SO<sub>4</sub>, to achieve significant enhancement in SC performance of VGN. As-grown VGN showed a capacitance of 0.64 mF/cm<sup>2</sup> in H<sub>2</sub>SO<sub>4</sub> electrolyte. This study indicates the potential of hybrid electrolyte in enhancing the areal capacitance to 1.99 mF/cm<sup>2</sup> with excellent retention (94.6 %) after 5000 cycles and coulombic efficiency (93 %). Also, a fivefold enhancement in the capacitance of VGN from 0.64 to 3.31 mF/cm<sup>2</sup> is achieved by the combination of KOH activation with the hybrid electrolyte.

**Chapter 7** summarizes the major findings of the present thesis work and also provides the scope of the work along with future directions.

# Chapter 2

## Experimental techniques

It doesn't matter how beautiful your theory is, it doesn't matter how smart you are. If it doesn't agree with experiment, it's wrong.

Richard P. Feynman

### 2.1 Introduction

This chapter provides a brief description of the growth techniques used to synthesize vertical graphene nanosheets (VGN), surface modification/alteration/activation of VGN and metal nanoparticle decoration on VGN. The Microwave plasma-enhanced chemical vapor deposition (MW-PECVD) technique is used for the synthesis and surface modification of VGN. Metal nanoparticle decoration is carried out using thermal evaporation and DC sputtering unit. The characterization techniques such as scanning electron microscopy (SEM), transmission electron microscopy (TEM), energy dispersive X-ray spectroscopy (EDS), X-ray photoelectron spectroscopy (XPS) and Raman spectroscopy employed to investigate the morphological, elemental and structural analysis, respectively. Surface energy and wetting property of the VGN surface is evaluated using contact angle measurement. The Electrical resistance of the VGN is measured by the four-point probe method. A brief introduction to the electrochemical measurement, principles for cyclic voltammetry, galvanostatic charge-discharge curve and electrochemical impedance spectroscopy (EIS) techniques are also presented.

## 2.2 Growth techniques

### 2.2.1 Electron cyclotron resonance chemical vapor deposition

Chemical vapor deposition (CVD) is a material synthesis method where a solid material is deposited using decomposition of gaseous precursors through a chemical reaction that takes place near the substrate's heated surface. The characteristic feature of the CVD technique is enabling the production of coatings with uniform thickness, non line-of-sight deposition process, localized and selective deposition on the substrates.

Further, the CVD process is classified based on the way the chemical reaction takes place. For example, if the chemical reaction is initiated and maintained by heat, the process is called thermally activated CVD. Photons, electrons, ions and a combination of these, i.e plasma also induce and sustain the CVD reactions [123]. Currently, plasma enhanced CVD (PECVD) is the subject that brings attention from academic and industry sectors because of the level of controllability in the plasma-based nanofabrication. Both the catalytic and non-catalytic PECVD techniques are suitable for fabrication of particularly, various carbon nanostructures including nanotubes and graphene. Compared to conventional CVD techniques in PECVD, the major advantage is growth of pattern designs of vertically oriented nanostructures, lower nucleation temperature and high growth rate.

Parameters	arc-discharge	RF plasma	MW plasma
Discharge power range (kW)	0.1-10	0.01-10	0.1-10
Plasma density ( $\text{cm}^{-3}$ )	$10^{11}$ - $10^{14}$	$10^{10}$ - $10^{13}$	$10^{10}$ - $10^{13}$
Electron energy in discharge (eV)	0.5-1	1-5	5-10
Operating pressure range (mbar)	-	0.01-10	0.1-100
Typical frequency	-	0.46-13.56 MHz	2.45 GHz
Power density ( $\text{W} \times \text{cm}^{-3}$ )	-	0.01-0.5	1-2
Substrate temperature range	-	100-500 °C	100-800 °C
Discharge electrode	Required	Required	Not required

**Table 2.1** – Typical parameters of arc-discharge, radio frequency and microwave plasma used for nanomaterial synthesis.

In this thesis, the synthesis of VGN is carried out by electron cyclotron resonance microwave plasma enhanced chemical vapor deposition (ECR-MW-PECVD) system also known as ECRCVD. In the PECVD technique, the plasma is produced in various ways namely arc discharge, radio frequency (RF) or microwave (MW) systems for the fabrication of various carbon nanostructures [124]. Typical parameters for the different plasma systems are tabulated in the table 2.1. However, the microwave plasma technique enables catalyst free nucleation and high density growth, vertically oriented structures.

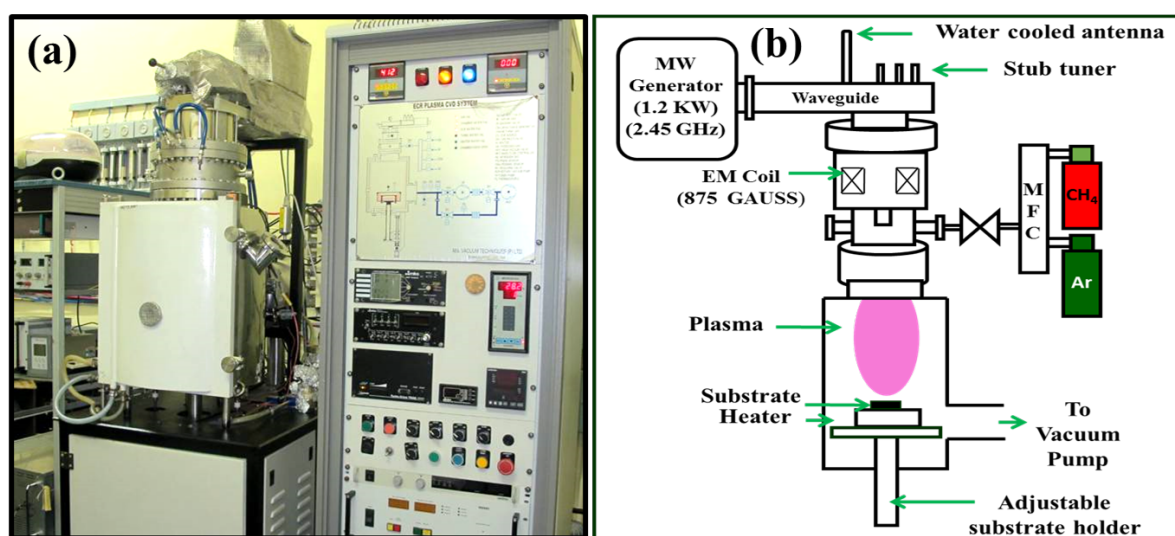


**Figure 2.1** – (a) Photograph and (b) schematic of the ECRCVD.

Figure 2.1 depicts the photographic image and a schematic of ECRCVD used in this work. The important components of ECRCVD are the vacuum pumping system, growth chamber and plasma source. Vacuum pumping system contains rotary pump (350 L/min) and turbo molecular pump (1100 L/s) with Pirani ( $0.5 \cdot 10^{-3}$  mbar) and Penning ( $10^{-3}$ - $10^{-6}$  mbar) vacuum gauges. The growth chamber is 64 cm in height and a diameter of 54 cm. The heating element contains resistive coil heating of the substrate coupled with a programmable PID controller. A thermocouple placed underneath the substrate holder was used to monitor the temperature of the holder. For plasma production, the main components are microwave generator, microwave introduction window and electromagnet.

The frequency of the microwave supply is 2.45 GHz with power up to 1.2 kW. The  $TE_{01}$  mode microwave is radiated by a cylindrical waveguide and is transferred to a circular polarized  $TE_{11}$  mode. The stub tuners is used to adjust the reflected microwave power to match the impedance between the microwave system and plasma. The microwave passed to the chamber through a cylindrical quartz cup with a 90 mm diameter and 30 mm thickness. The magnetic field of 875 Gauss is produced by a magnetic coil system which is powered by DC current.

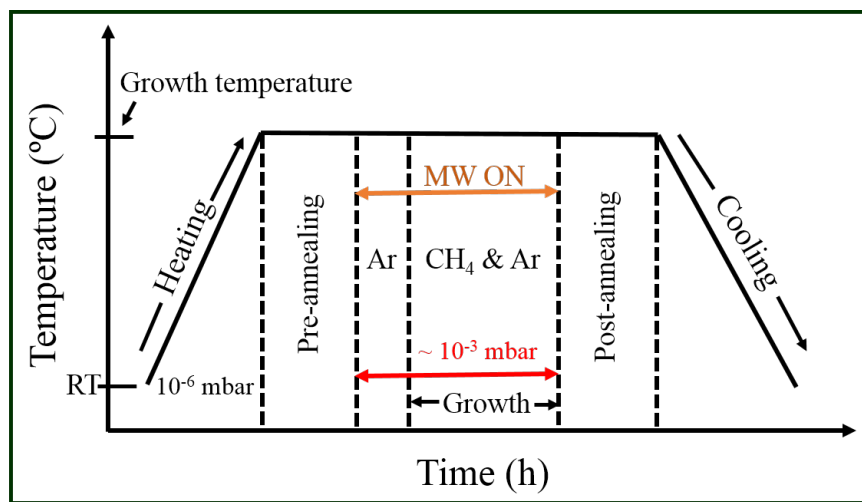


**Figure 2.2** – Typical temperature vs. time growth profile for VGN.

The typical temperature *vs.* time growth profile for VGN is shown in figure 2.2. For this thesis work, VGN are grown on Ni, carbon paper (Avcarb® MGL370) and  $SiO_2/Si$  substrate for different purposes. For the  $SiO_2$  growth, Si(100) substrate is heated up to 1000 °C, kept there for 8 hours in a muffle furnace and cooled naturally to room temperature. Ultra-high pure Ar and  $CH_4$  gases were used as diluent and source, respectively. The steps involved in the growth process are as follows: the substrate is loaded into the chamber and the chamber is evacuated to  $10^{-6}$  mbar by a turbo molecular backed by a rotary pump. Thereafter, the substrate is annealed at 800 °C and afterwards cleaned by Ar plasma at 200 W power. Then the  $CH_4$  gas at 5 sccm with Ar at 20 sccm flow rate are fed into the chamber for growth. The growth temperature is maintained at 800 °C

and growth is carried out by striking plasma at 375 W microwave power at an operating pressure of  $2 \times 10^{-3}$  mbar. After the growth, the plasma is switched off and the film is subjected to post-growth annealing at 800 °C to improve the structural quality of the VGN. Finally, the sample was cooled down to room temperature and removed from the chamber for further characterization.

### 2.2.2 Thermal evaporation unit

The thermal evaporation is one of the essential techniques among the PVD methods used for the deposition of material mainly metals [125]. The three significant steps involved in this technique are the generation, transport, and condensation of the vapor phase of metals on the substrate under a high vacuum ( $10^{-6}$  mbar). The evaporation of the metal is carried out at high temperature through electrical resistive heating. The schematic diagram of a typical thermal evaporation system with components is shown in figure 2.3.

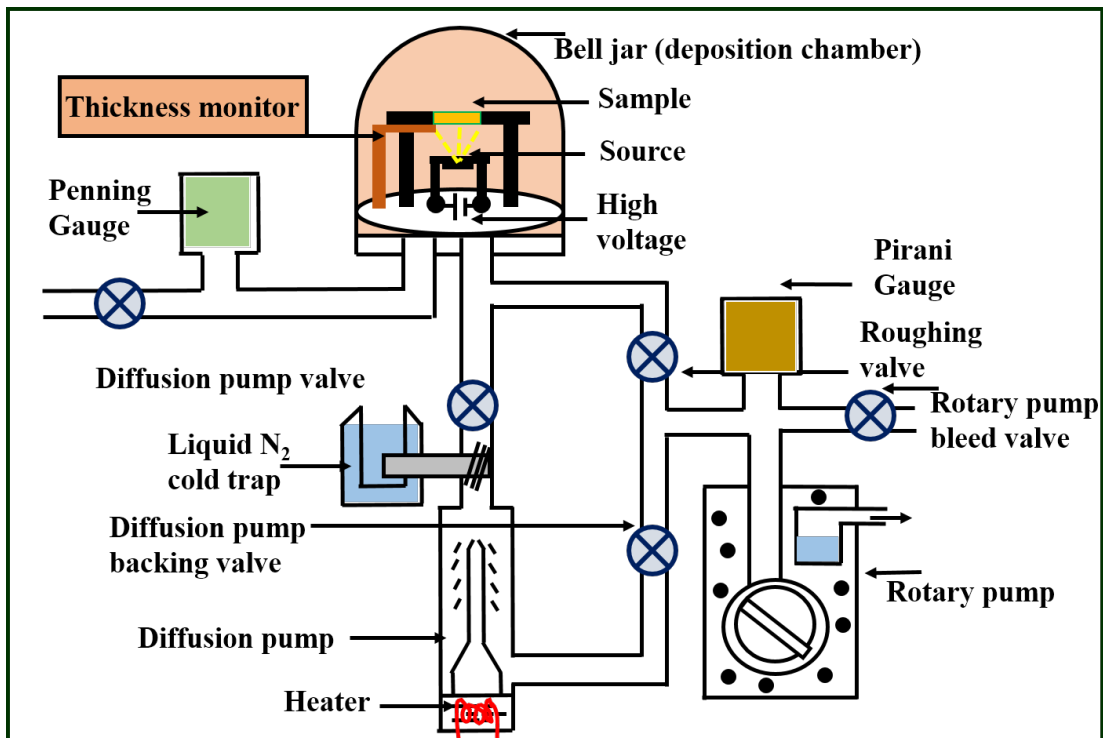


Figure 2.3 – Schematic of thermal evaporation unit.

The deposition of metal and metal oxide on VGN film in this thesis were carried out using

a high vacuum thermal evaporation system (12A4D, HINDHIVAC, India) with the multisource evaporation and in-situ thickness monitor facilities. The important components of the system are listed below.

- A. Vacuum chamber: Bell jar type
- B. Substrates: SiO<sub>2</sub>/Si(100), VGN/CP, VGN/SiO<sub>2</sub>
- C. Vacuum pumping system:
  - a) Rotary pump (ED-15, 250 L/min,  $1 \times 10^{-3}$  mbar)
  - b) Diffusion pump (OD-114D, 280 L/s,  $1 \times 10^{-6}$  mbar)
  - c) Vacuum gauges (Pirani and Penning gauges); maximum vacuum:  $1 \times 10^{-6}$  mbar
  - d) Primary current (Maximum): 100 A
- D. Digital thickness monitor: quartz crystal thickness monitor, 0.1 Å/s resolution

### 2.2.3 DC sputtering

In this thesis, a DC sputtering unit was used for the deposition of Ni(OH)<sub>2</sub> clusters onto VGN and gold thin film coating for electrical contact. The sputtering is one of the physical vapor deposition techniques routinely used for thin-film growth [126]. A schematic of the sputtering process is illustrated in figure 2.4(a).

In DC sputtering system, the vacuum chamber is evacuated to  $1 \times 10^{-2}$  mbar. The chamber pressure is maintained at 0.08 mbar by leaking high pure (99.999%) argon gas. The potential is applied between the cathode and anode to accelerate electrons between the electrodes. These accelerated electrons then collide with Ar atoms and produce Ar<sup>+</sup> ions along with secondary electrons which creates the glow discharge. The electrons are attracted by the anode, whereas the Ar<sup>+</sup> ions are accelerated towards the cathode.

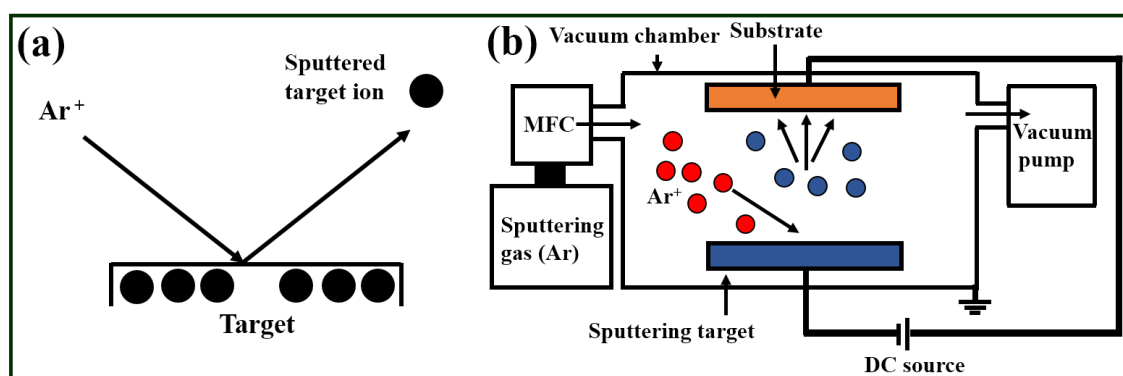


**Figure 2.4** – Schematic of (a) sputtering process and (b) DC sputtering unit.

The energetic  $\text{Ar}^+$  ions upon impinging produce secondary electrons and sputter atoms from the surface of the cathode (target). These secondary electrons are useful to sustain the glow. The sputtered atoms finally condense on the substrate. A sketch of the DC sputtering system is shown in figure 2.4(b).

## 2.3 Characterization techniques

### 2.3.1 Morphological characterization

The morphology of the VGN structures was analyzed by field emission scanning electron microscope (FESEM, Supra 55, Carl Zeiss, Germany) and high-resolution transmission electron microscopy (HRTEM, LIBRA 200FE, Zeiss, Germany). FESEM is used to analyze surface morphology and height of the VGN. HRTEM is used for high-resolution image of the VGN to find out the number of graphene layers present in the vertical graphene sheets.

### 2.3.2 X-ray photoelectron spectroscopy (XPS)

X-ray photoelectron spectroscopy is used for the elemental and chemical composition analysis. The XPS works on the process of photoemission [Figure 2.5(a)] in which electron is ejected from a core level of an atom in the specimen by an incident X-ray photon of

energy  $h\nu$  [127]. The energy of the emitted photoelectrons is then analysed by the electron spectrometer and the data is presented as a graph of intensity (counts) versus electron energy. The photoelectrons are ejected with discrete kinetic energy ( $E_k$ ) given by:

$$E_k = h\nu - E_B - W \quad (2.1)$$

Where  $E_B$  is the binding energy of the atomic orbital from which electron originates and  $W$  is the work function of the material.

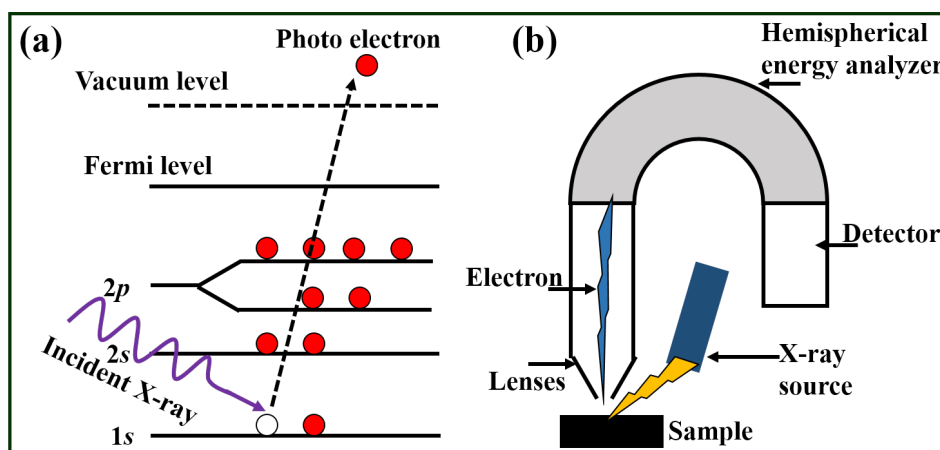


**Figure 2.5** – Schematic view of X-ray photo electron emission process and (b) block diagram of XPS.

The energy of the photoelectron is characteristic of the element from which it is ejected, thus enabling the identification of the atomic species. The photoelectrons that we measure that are characteristic energies for the atoms of interest come from the region around 10 nanometers or less. So, XPS is very surface sensitive. Also, the chemical shift happens as a change in the binding energy of a core electron of an element due to a change in the chemical bonding of that element. The peak shift in XPS spectra is mostly related to chemical shifts due to the presence or absence of the chemical states of the element having different formal oxidation state. The major components of an XPS system (figure 2.5(b)) are X-ray source/gun: A twin anode configuration providing Al  $K_\alpha$  (1486.6 eV)

or Mg  $K_\alpha$  (1253.6 eV), hemispherical electron energy analyzer and an electron detector. In the present thesis, x-ray photoelectron spectroscopy (XPS, Surface Nano Analysis SPECS, GmbH, Germany) studies of VGN were carried out using an x-ray source of nonmonochromatic Al  $K_\alpha$  (1486.6 eV). The spectra were analyzed by applying Shirley type background and curve fitted with a mixture of Gaussian-Lorentzian line shape.

### 2.3.3 Raman spectroscopy

The scattering of light due to interaction with matter can be classified as elastic (Rayleigh scattering) or inelastic (Raman or Brillouin scattering) [Figure 2.6] [128].

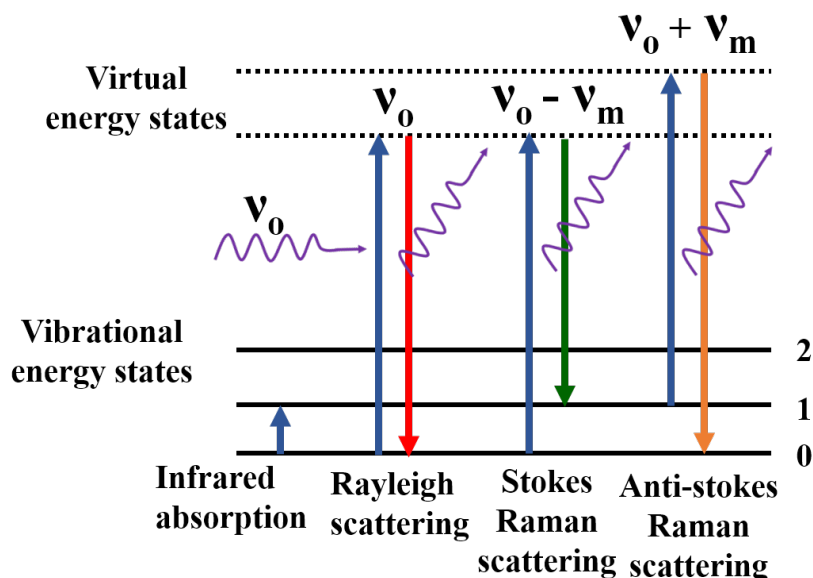


Figure 2.6 – Schematic of scattering process in Raman spectroscopy.

In the first case, the scattered light of the same frequency as the incident light ( $h\nu_0$ ). The inelastically scattered light detected at different frequencies than the incident constitutes the Raman or Brillouin signals. The Raman effect results from the change in molecule's polarizability induced by the interaction of vibrational and/or rotational motions of molecules with electromagnetic radiation [129]. The Raman scattering of the incident beam has frequencies  $\nu_0 \pm \nu_m$ , where  $\nu_m$  is a vibrational frequency of a molecule.

The  $\nu_0 - \nu_m$  and  $\nu_0 + \nu_m$  lines are called the Stokes and anti-Stokes lines, respectively.

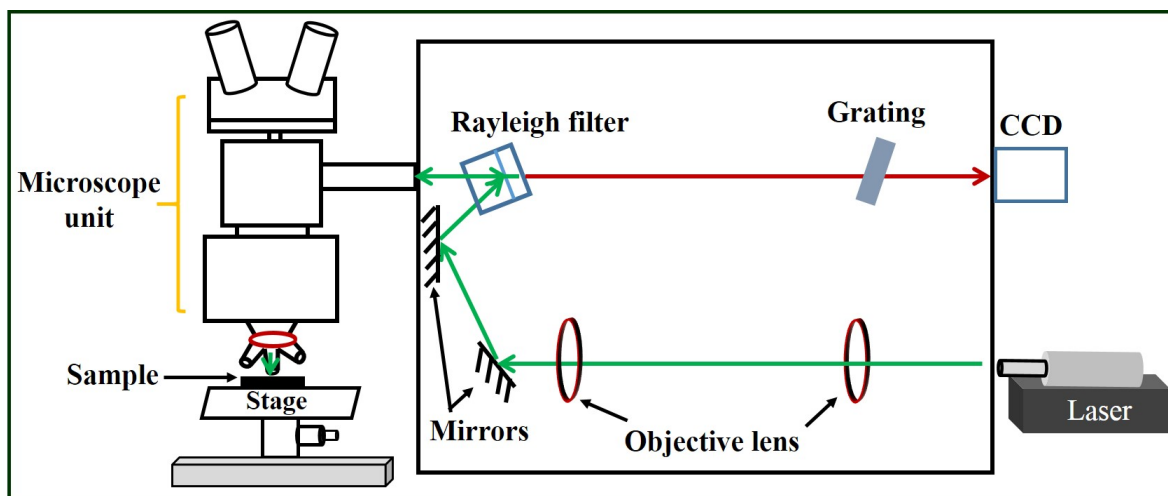


Figure 2.7 – Schematic of the Raman spectrometer.

The major components of a Raman spectrometer are listed below:

- A. Excitation source: continuous wave lasers  $\text{Ar}^+$  with 514.5 nm (power 150 mW).
- B. Sample illumination and collection system: set of lenses or microscope backscattering configuration, standard and confocal mode,  $\times 5$ ,  $\times 20$ ,  $\times 50$ ,  $\times 100$ .
- C. Rayleigh rejection filter: Notch/edge filters.
- D. Wavelength selector: monochromator gratings; 1800 and 2400  $\text{gr}\cdot\text{mm}^{-1}$ .
- E. Detector and computer control/processing system: photomultiplier tube/charged coupled detector (CCD). Thermoelectrically cooled CCD and InGaAs detectors.

In this thesis, the Raman scattering studies on VGN were carried out using a micro-Raman spectrometer (inVia, Renishaw, UK). All the major components along with available facilities of the system are reported below along with its block diagram [Fig. 2.7].

### 2.3.4 Contact angle measurement

The surface energy, one of the important parameters to affect the wetting property of the materials (thin films/ nanostructures), is subject of matter for their potential application. The wetting nature and surface energy of the material's surface can be evaluated by the contact angle of a fluid droplet of a constant volume on the solid surface [130].

When a drop of liquid is placed on the solid surface, it experiences both adhesive and cohesive forces. The adhesive force acting between the liquid/solid surface helps for spreading the liquid and the cohesive force counteracts the spreading. Young's equation 2.2 describes the balance between these forces which relates the contact angle to the surface free energy of a system containing solid (s), liquid (l), and vapor (v) phases, as shown in figure 2.8(a),

$$\gamma_{sv} - \gamma_{sl} = \gamma_{lv} \cos \theta_c \quad (2.2)$$

Where,  $\gamma_{sv}$ ,  $\gamma_{sl}$  and  $\gamma_{lv}$  represent the surface free energy of solid, solid/liquid interface and liquid, respectively. Where  $\theta_c$  is the contact angle.

Depending on the value of contact angle, the wetting nature surface can be classified into four categories: hydrophilic ( $\theta_c < 90^\circ$ ), super-hydrophilic ( $\theta_c = 0^\circ$ ), hydrophobic ( $\theta_c > 90^\circ$ ) and super-hydrophobic ( $\theta_c > 150^\circ$ ). In addition to that, the substrate's surface energy can also be calculated from contact angle measurement by using different liquids in addition to the water. In general, the higher the contact angle, the lower the surface energy. The contact angle measurement set up is shown in figure 2.8(c). The major components of the set up are as follows: light source, microsyringe connected with screw gauge, CCD camera interfaced with a computer.

The contact angle of the VGN surface were measured by the sessile drop method with the

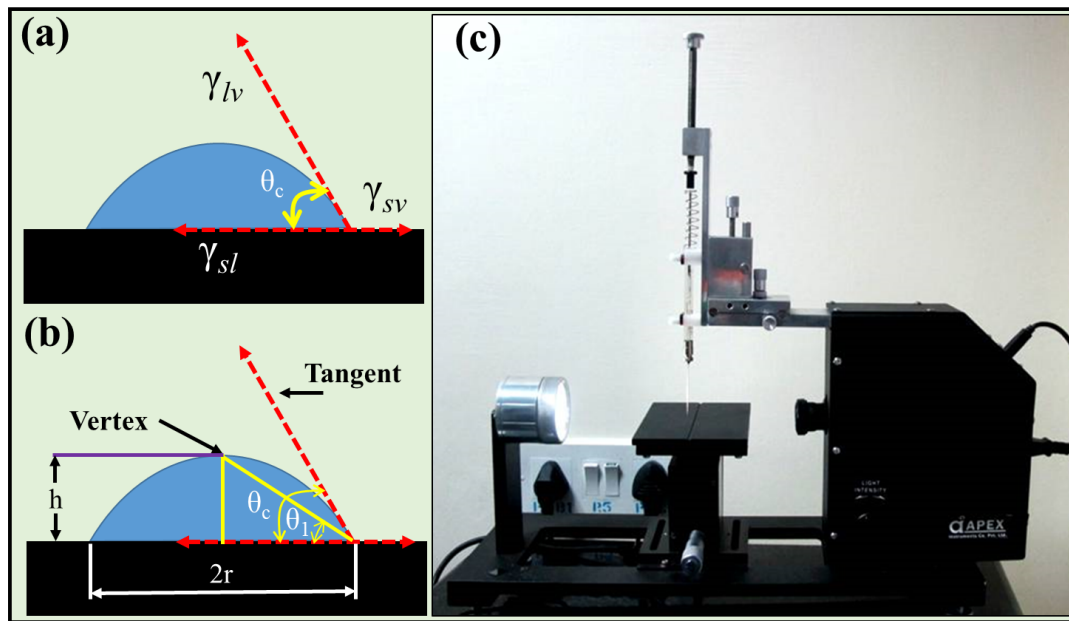


**Figure 2.8** – Schematic (a) of the contact angle by a liquid droplet, (b) illustration of relation between angles and (c) contact angle set up in our lab.

help of a CCD camera (D1N01, Acam, India). All the measurements were carried out in ambient conditions and the volume of the droplet was kept about  $1 \mu\text{l}$ . The contact angle value was evaluated by half-angle fitting method provided with the instrument equation 2.3 and verified by ImageJ software calculation. The angle between the vertex and the baseline is calculated using trigonometry [Fig. 2.8(b)]. The surface was assumed to be a part of a circle. The following relation was used to measure the contact angle, where  $\theta_c = 2\theta_1$ ,

$$\tan\theta_1 = \frac{h}{r} \Rightarrow \theta_c = 2\tan^{-1}\left(\frac{h}{r}\right) \quad (2.3)$$

### 2.3.5 Four-probe point method

The sheet resistance is one of the parameters for evaluating the electrical properties of the material [131]. The four-point probe method is commonly used to measure the sheet resistance by using the Van der Pauw method. The advantage of the Van der Pauw method is that it requires tiny, irregular shaped samples and also less surface area for

resistivity measurement. Figure 2.9 shows the arrangement for the measurement that requires four small contacts around the edge of a homogeneous and uniform thickness ( $t$ ) sample.

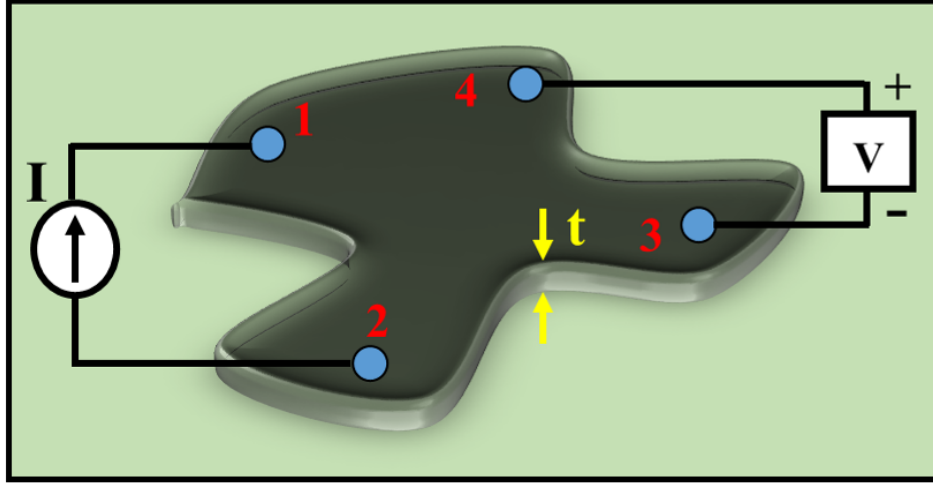


**Figure 2.9** – Schematic of four point probe contact on the arbitrary shape of the material.

The sheet resistance ( $R_{sh}$  in  $\Omega/\square$ ) can be expressed as,

$$R_{sh} = \frac{\rho}{t} = \frac{\pi}{\ln 2} \left( \frac{R_{12,34} + R_{23,41}}{2} \right) F \quad (2.4)$$

Where  $\rho$  is the resistivity of the material,  $t$  is the layer thickness, resistance  $R_{12,34}$  is defined as,

$$R_{12,34} = \frac{V_{34}, \text{ voltage difference between contacts 3 and 4}}{I_{12}, \text{ current flows between contact 1 and 2}} \quad (2.5)$$

Similarly  $R_{23,41}$  and  $F$  is van-der Pauw correction factor, which is satisfying the relation,

$$\frac{R_{12,34} - R_{23,41}}{R_{12,34} + R_{23,41}} = \frac{F}{\ln 2} \operatorname{arccosh} \left[ \frac{\exp(\ln 2 / F)}{2} \right] \quad (2.6)$$

The sheet resistance of VGN structures in the current thesis was measured using the Agilent B2902A precision source/measure unit. The electrical contacts in this study were made by attaching a thin Cu wire to the material using conducting Ag paste.

### 2.3.6 Electrochemical measurement

The electrochemical performance of the single electrode and devices were carried out by 3-electrode and 2-electrode setup, respectively. A schematic of the 3-electrode system is depicted in figure 2.10(a). The major components of the 3-electrode system are:

*Working electrode:* Working electrode (WE) is the electrode on which the primary reaction takes place. The area of the electrode affects the electrochemical capacitance and very influential depending on the applications.

*Counter electrode:* The counter electrode (CE) is made of generally from inert materials like Au, Pt, glassy carbon and graphite. This electrode does not participate in the chemical reaction and only closes the current circuit in the electrochemical cell. Generally, a higher area of the counter electrode is dipped into the electrolyte to avoid the surface area not to be a limiting factor in the kinetics of the reaction process.

*Reference electrode:* This electrode has a stable potential and is used as a reference point for potential measurement in the electrochemical cell. There are several standard reference electrodes (RE) like standard hydrogen electrode, saturated calomel electrode, silver chloride electrode and pH-electrode. The high stability of these electrodes is maintained by providing a redox system with saturated concentration. The current through the reference electrode kept nearly zero by keeping a very high input impedance in the circuit between RE and CE. Figure 2.10(b) shows the basic block diagram of potentiostat/galvanostat (PGSTAT) of AUTOLAB, Metrohm, which was used for evaluating the electrochemical performance of VGN structures.

The potential is controlled between the WE and CE in potentiostatic (PSTAT) mode whereas, in case of galvanostatic (GSTAT) mode, the current is controlled between the WE and the CE. The potential difference between the RE and WE and the current flowing between the CE and WE are continuously monitored. By using a PGSTAT, the potential

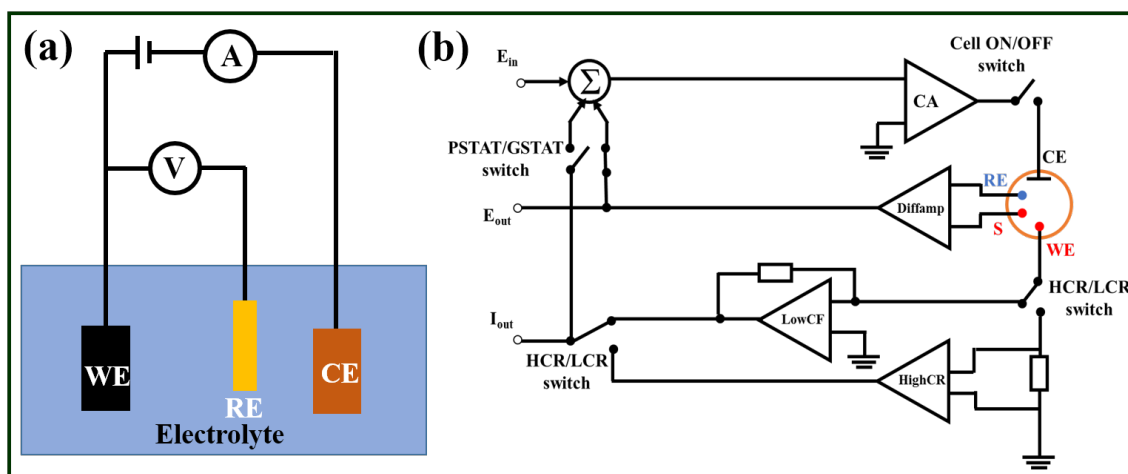


**Figure 2.10** – (a) Schematic of three electrode system, and (b) block diagram of potentiostat/galvanostat.

or current is controlled by a negative feedback mechanism. The control amplifier (CA) forces current to flow through the cell and the value of the current is measured by a current follower (LowCF) or HighCR, for low and high currents, respectively. The differential amplifier (Diffamp) measures the potential difference between the RE and shunt (S). The PSTAT/GSTAT switch is set depending on the mode (potentiostatic or galvanostatic) of use. The input signal is then fed to the Summation Point ( $\Sigma$ ) with the waveform ( $E_{in}$ ) set by the digital-to-analog converter. The cell cables of the Autolab PGSTAT contain five connectors marked as WE, CE, RE, S and ground.

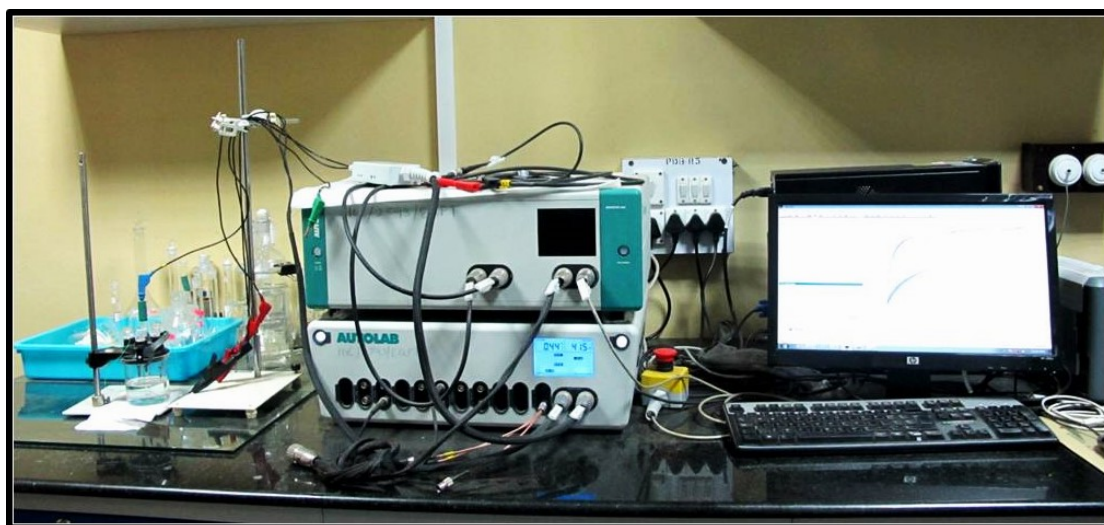


**Figure 2.11** – Photograph of electrochemical setup.

Always, the potential is measured between RE and S. Whereas, the current is measured between WE and CE. The ground connector is used to connect external devices to the same ground of the PGSTAT. The autolab system used is shown in figure 2.11. Three different techniques measure the electrochemical performance:

### 2.3.6.1 Cyclic voltammetry

Cyclic voltammetry (CV) is extensively used to study the redox reaction reversibility and determine the voltage window of electrodes or devices. The CV principle is to measure the resulting current simultaneously when applying a linear voltage to an electrode or a device between two preset voltage limits. The CV experiments are carried out at different scan rates, for example from 0.1 V/s to 0.5 V/s for conventional supercapacitors and from 0.1 V/s to 0.8 V/s for symmetric supercapacitors.

### 2.3.6.2 Galvanostatic charge-discharge curve

Galvanostatic cycling charge-discharge (CD) is widely used to calculate the capacitance and cycling stability of electrodes or devices. The principle of CD is to measure the resulting voltage simultaneously while applying a constant current to an electrode or a device between two preset voltage limits. CD experiments are carried out at different current densities, for example from 0.1 mA/cm<sup>2</sup> to 0.5 mA/cm<sup>2</sup> for conventional supercapacitors and symmetric device.

### 2.3.6.3 Electrochemical impedance spectroscopy

The equivalent series resistance, charge transfer resistance and diffusion impedance of electrochemical devices can be studied by electrochemical impedance spectroscopy (EIS). The main difference between EIS and CV is that in EIS a sinusoidal voltage signal is imposed at a range of frequencies and the resulting current is measured, while a linear voltage is applied in CV. EIS experiments were carried out in the frequency range from 100 kHz to 0.01 Hz by applying 10 mV amplitude of the sinusoidal voltage. The impedance

spectra are fitted by EIS spectra analyzer software by using an appropriate equivalent electric circuit.

For this thesis work, the electrochemical performance of the VGN based materials were carried out by Metrohm-Autolab electrical work station (model PGSTAT302N, Netherland). The Platinum foil, Ag/AgCl (3M KCl) and VGN based material were used as counter, reference and working electrodes, respectively.

## **2.4 Summary**

The experimental techniques used to synthesize VGN and modified VGN structures are discussed in detail with principle and block diagrams.

# Chapter 3

## Growth of vertical graphene nanosheets and scalable transfer for flexible supercapacitor applications

Equipped with his five senses, man explores the universe around him and calls the adventure science.

-Edwin Hubble

### 3.1 Introduction

The demand for flexible electronic devices stimulated the rapid development of flexible supercapacitors. Towards this vertical graphene nanosheets (VGN) emerge as the material of choice for a flexible electrode for supercapacitor applications [132, 133]. However, the growth of VGN requires high temperatures ( $> 300$  °C), which limits the choice of substrate materials as most of the flexible substrate does not withstand such high temperatures. This brings in the demand for growth of VGN at lower temperature. Nevertheless, high growth temperatures are required to obtain VGN with high structural quality, good electrical conductivity and the unique interconnected 3D open porous network [75]. The growth of VGN on a variety of substrates that can withstand the high growth temperatures is reported. The difficulty associated with direct growth of VGN on flexible substrates can be overcome by adopting an effective strategy of transferring

the well-grown VGN onto arbitrary flexible substrates through the chemical route. Some literature addressed the issues by transferring graphene using methods like laser-induced transfer technique (LIFT) and polymer-based transfer process [67, 69, 71]. However, these methods give rise to morphological damage and surface alteration after the transfer process. Since most of the transfer processes use polymer, which gets filled inside the porous network of VGN and will be difficult to remove. Moreover, the VGN is easily peelable, so it can be damaged very easily while removing the polymer in the post-cleaning processes. Hence, one should consider the etching of the bottom substrate with a slow etching rate and then transfer, so that the film should not experience any disturbance.

In this chapter, a single-step, polymer-free and simple technique is adopted to transfer scalable VGN onto any arbitrary substrate without disrupting its morphology, structure and properties. Furthermore, the charge storage capacity is studied by fabricating a flexible symmetric supercapacitor device using the transferred VGN without any binder and current collector. An excellent capacitance of  $158 \mu\text{F}/\text{cm}^2$  with capacitance retention of 86 % is observed after 10000 charge-discharge cycles .

## 3.2 Growth and transfer of VGN

### 3.2.1 Growth of VGN

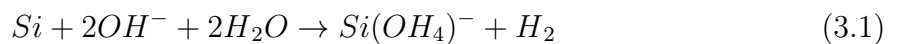
VGN are grown on Ni, SiO<sub>2</sub>/Si substrate by ECRCVD technique, where high pure Ar and CH<sub>4</sub> were used as the diluent and source gas, respectively. The substrate is then loaded to the chamber, which was evacuated to  $10^{-6}$  mbar using a turbo molecular pump backed by a rotary pump. Thereafter, the substrate was annealed at 800 °C and subsequently cleaned by Ar plasma at microwave power 200 W for 10 min. After the substrate cleaning, hydrocarbon gas (CH<sub>4</sub>) at 5 sccm and Ar of 20 sccm flow rate was fed into the synthesis chamber for the growth of the VGN. The substrate temperature at 800 °C,

microwave power at 375 W and  $2 \times 10^{-3}$  mbar operating pressure was maintained during the growth. After the growth, plasma was turned off and the as-grown film was subjected to a post-growth annealing at 800 °C to improve the structural and morphological quality [134]. Finally, the sample was cooled down to room temperature and taken out for characterization.

There are several studies reported on the growth mechanism of VGN [15, 75]. The commonly accepted growth mechanism for VGN is (i) adsorption of  $\text{CH}_3$  radicals and amorphous carbon layer formation on the substrate, (ii) formation of nucleation sites at the defect areas, (iii) appearance of nanoislands at the nucleation sites with dangling bonds, (iv) growth of small graphene nanosheets, and (v) formation of nanographene sheets with arbitrary orientation. The growth of VGN in the vertical direction is mainly due to the electric field, residual stress and an-isotropic growth effects [15]. The localized electric field at the substrate controls the orientation and density of the VGN network. The temperature gradient and lattice mismatch produce internal stress, causing buckling of the amorphous layer that serves as a nucleation site for vertical growth. Also, the anisotropic growth rate in the perpendicular and parallel directions is one reason behind the vertical growth.

### 3.2.2 Transfer of VGN

The transfer of VGN was carried out by soft chemical routes. The first attempt towards the polymer-free transfer of VGN was carried out by dipping VGN grown on Si in a 1M KOH solution. The sample was dipped for 2 hours in the KOH solution for Si etching. The reaction for etching of Si by KOH is given by equation 3.1. After the Si substrate was etched away, the floating VGN film was fished on to an overhead projector sheet.



The photographic image of the transferred film by this process is shown in figure 3.1. Degradation of the sample during the transfer process is due to poor stability of the film after wetting by KOH.

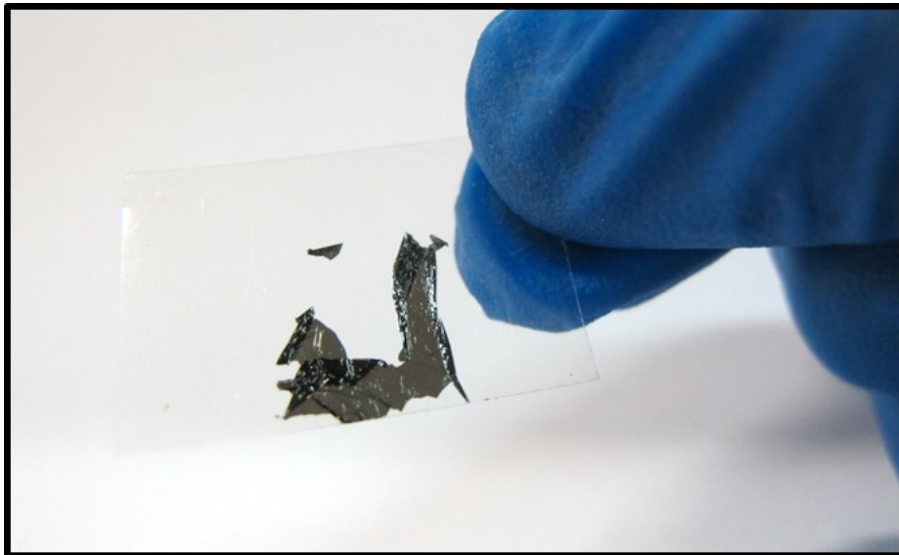
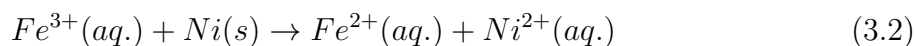


**Figure 3.1** – Photograph of transferred VGN to overhead projector (OHP) sheet.

In order to avoid surface damage, the transfer process adopted in the present study is a modified and simple form of the process reported by Kim *et. al.*, [67] for CVD grown single-layer graphene on metallic substrate. Polymers use in the transfer process were excluded to avoid the tedious job of its removal. The as-grown VGN on Ni (VGN/Ni) was annealed at 80 °C for 10 min to increase the etching rate and for easy detachment from the substrate surface [135]. To etch Ni, the VGN/Ni was floated in 1M FeCl<sub>3</sub> solution for 90 min. The Ni ion etching reaction without the formation of gaseous products is given here:



The floating VGN film in figure 3.2(d) confirms the complete etching of the Ni substrate. Then the FeCl<sub>3</sub> solution and etched Ni were removed using a syringe and the remaining part was diluted by adding deionized (DI) water. This procedure of FeCl<sub>3</sub> solution removal and dilution with DI water was repeated many times until the concentration of FeCl<sub>3</sub>

reduced and entirely removed from the solution. The floating film was then transferred to glassware containing DI water. Subsequently, the desired flexible substrate was cleaned by sonicating it in isopropyl alcohol and dried in nitrogen gas. The floating film was then transferred onto the clean desired substrate (OHP sheet) by carefully scooping it out and dried for 30 min to remove the water at the interface.

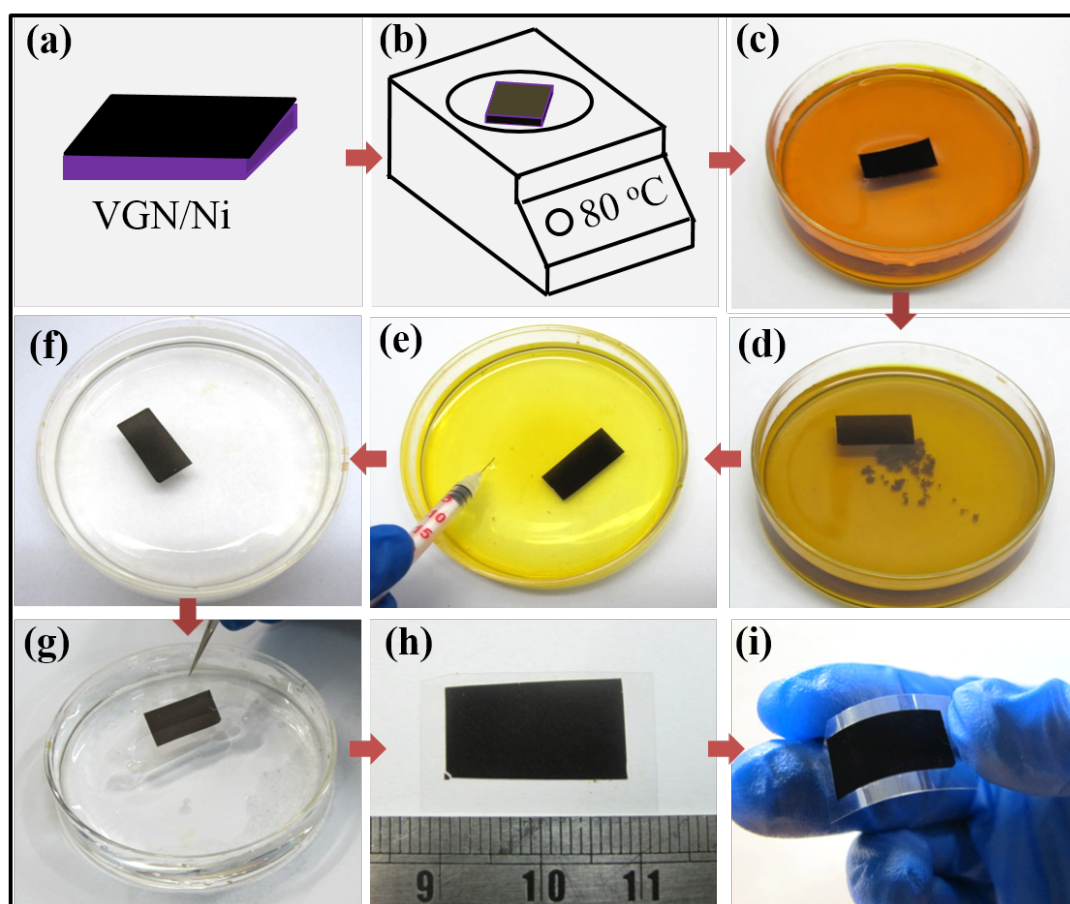


**Figure 3.2** – Schematic of the transfer process of VGN onto flexible substrate. (a) VGN/Ni, (b) baked VGN/Ni, (c) floated VGN/Ni in  $\text{FeCl}_3$  solution, (d) freely floating VGN after Ni etching, (e) dilution of  $\text{FeCl}_3$  solution by DI water, (f) free floating VGN on DI water, (g) scooped out VGN to flexible substrate and (h), (i) optical image of  $2 \times 1 \text{ cm}^2$  VGN on flexible substrate with scaling.

The schematic of the transfer process and photograph of the transferred film are depicted in figure 3.2. From figure 3.2(h) and (i), it is clear that the transferred VGN (VGN/OHP) is uniform, wrinkle and crack-free and well adherent to substrate. The whole procedure was repeated many times to ensure reproducibility. It is noteworthy that the transfer

procedure does not need any polymer support, removal step and helpful for the current collector free electrode fabrication. The complete transfer process takes almost 2 hours and requires careful handling. The transfer of VGN was also carried out onto a variety of substrates like glass slide, paraffin and carbon cloth. The advantages of this procedure are its high reproducibility, single-step process and simplicity.

### 3.3 Morphology and structural analysis

Scanning electron microscopy and Raman spectroscopy are carried out for the morphological and structural study, respectively for the as-grown VGN/Ni and transferred VGN/OHP. The SEM micrographs of the as-grown VGN/Ni and transferred VGN/OHP are shown in figures 3.3(a) and (b), respectively. The observed results confirm the retention of morphology after the transfer process. Figure 3.3(c) shows the typical cross-sectional FESEM image of the VGN, which ensures the vertical orientation of the structure. The nanographitic layer at the interface of the substrate supports the vertical orientation. The non-agglomerated and porous 3-D network of VGN is also evident from the SEM micrographs. The structure helps easy access for the electrolyte ions and makes it beneficial for supercapacitor performance.

Raman spectroscopy is a general technique used for structural confirmation of graphene materials which also gives information about defects, disorders, doping, number of layers and strain of the graphene materials [136]. Figure 3.3(d) depicts the obtained Raman spectra for as-grown VGN/Ni and transferred VGN/OHP. Typical Raman spectra consist peaks corresponding to D'' (1100  $\text{cm}^{-1}$ ), D (1350  $\text{cm}^{-1}$ ), G (1580  $\text{cm}^{-1}$ ), D' (1620  $\text{cm}^{-1}$ ), D+D'' (2460  $\text{cm}^{-1}$ ), G' (2700  $\text{cm}^{-1}$ ), D+D' (2950  $\text{cm}^{-1}$ ) and 2D' (3240  $\text{cm}^{-1}$ ). The D, G and G' are the signature peaks of the VGN structure [75]. Where the G peak is due to the first-order Raman scattering of the doubly degenerate (iTO and LO) phonon

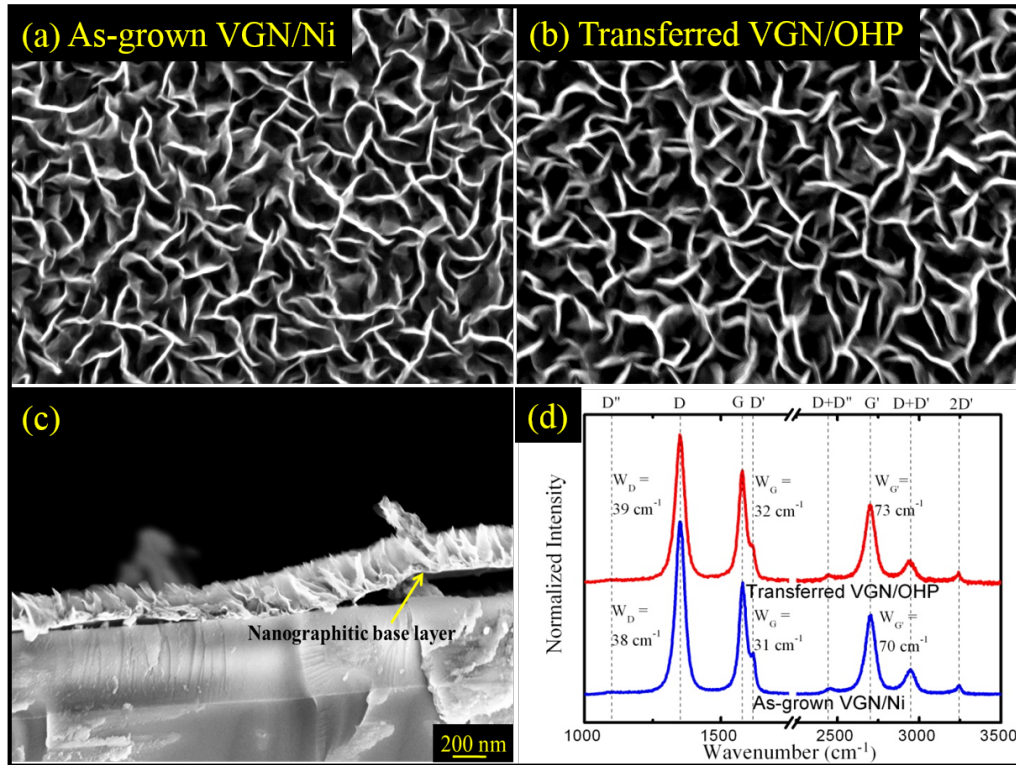


**Figure 3.3** – FESEM micrograph of (a) as-grown VGN/Ni and (b) transferred VGN/OHP ; 1 cm = 500 nm, (c) cross sectional image of VGN with NG layer and (d) Raman spectra of as-grown and transferred VGN.

modes ( $E_{2g}$  symmetry) at the zone center and it reflects  $sp^2$  nature of the graphitic planes [129, 136]. The  $G'$  peak originates from a second-order process involving two iTO phonons and gives information about the number of graphene layers [129, 136]. The  $D''$ ,  $D$ ,  $D'$ ,  $D+D''$ ,  $D+D'$  and  $2D'$  are disorder-induced peaks due to random orientation of the structure, nanographitic base layer with  $sp^3$  content, presence of C-H bonds, a large amount of unsaturated edges, fullerene-like structure and pentagon-heptagon carbon rings etc. [136, 137].

Low full width at half maximum (FWHM) of  $D$ ,  $G$  and  $G'$  indicates the higher degree of crystallinity. The Raman spectra are recorded for both the samples at several places.

The average FWHM of the  $D$ ,  $G$  and  $G'$  peak of the as-grown VGN/Ni is found to be 38, 31, and 70  $\text{cm}^{-1}$ , respectively. However, for transferred VGN/OHP 39, 32, and 73  $\text{cm}^{-1}$ , respectively. The slight increase in FWHM of  $G'$  after the transfer process can be

due to the substrate effect and trapped water in the interface of the transferred VGN and OHP sheet. A shift in the peak position is the signature of strain, change in surface chemistry and disorder [136]. An almost negligible shift in peak position and unchanged FWHM affirm that the surface chemistry and crystalline quality are maintained after the transfer process. Hence, the transfer procedure does not introduce any significant structural degradation and alteration in surface morphology.

### 3.4 Surface chemistry analysis

To study the surface chemistry after the transfer process, water contact angle (WCA) measurement and X-ray photoelectron spectroscopy (XPS) are carried out. Wetting is an important property that gets significantly influenced by any alteration of the surface chemistry and roughness. The WCA measurement of as-grown VGN/Ni and transferred VGN/OHP are shown in figures 3.4(a) and (b), respectively.

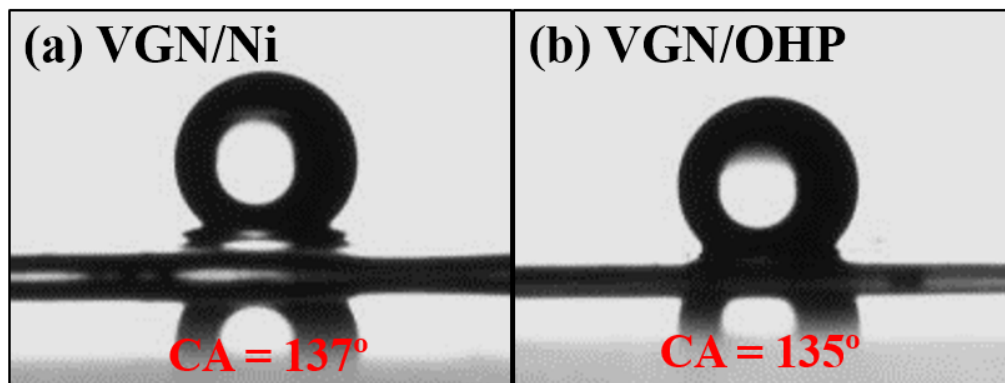


**Figure 3.4** – WCA of (a) as-grown VGN/Ni and (b) transferred VGN/OHP.

A similar WCA value of  $135^\circ \pm 2$  before and after the transfer process confirms the unaltered morphology and surface chemistry. The intrinsic hydrophobic nature of the VGN film has a suitable application in anti-corrosion, self-cleaning coating and anti-biofouling.

XPS is carried out for transferred VGN/OHP to investigate the surface chemistry and

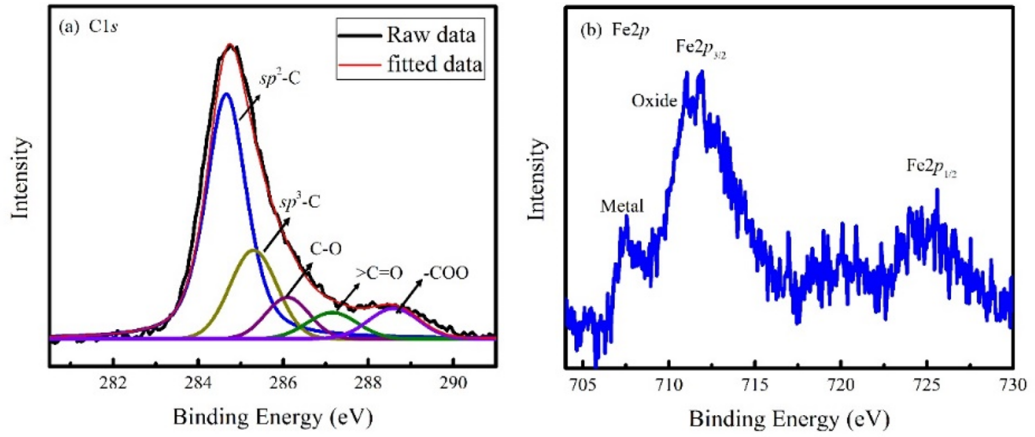


**Figure 3.5** – XPS spectra of (a) C1s and (b) Fe2p spectrum of transferred VGN/OHP.

contamination of Fe during transfer process. High resolution C1s spectrum of the transferred VGN is shown in figure 3.5(a). The C1s spectrum shows a prominent peak around 284.5 eV, assigned as  $sp^2$  C-C bonds. Also, less intense peaks at 285 eV ( $sp^3$  C-C), 285.9 eV (C-O), 287.4 eV (C=O) and 288.3 eV (-COO) are also observed [138, 139]. After several steps of dilution also, an unpreventable Fe content of 3.5 % is observed from the high resolution Fe2p spectrum shown in figure 3.5(b).

### 3.5 Electrical property study

Apart from structural quality, the material's surface carrier conductivity plays a vital role in the electrochemical capacitor as the electrical conductivity affects the charge transport, reaction kinetics at the electrode surface and charge-discharge behavior.

Therefore, the electrical resistance of the transferred VGN was measured using the four-probe method, as shown in the inset of figure 3.6, assuming continuous film thickness in the macroscopic scale. The linear  $I$ - $V$  relationship of VGN (figure 3.6), for both the configurations (i.e. when current is supplied between contacts 1 and 2 and voltage measured across 4 and 3 as well as current supplied between 1 and 4 and voltage measured across 2 and 3) ensure Ohmic contact. The sheet resistance of VGN is calculated from

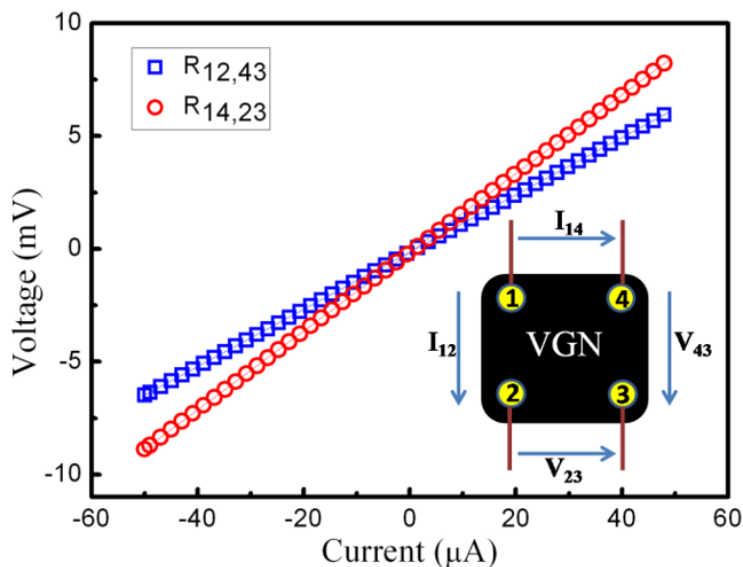


**Figure 3.6** –  $I$ - $V$  characteristic of transferred VGN/OHP. Inset shows the schematic of electrical contacts on VGN for measurement.

the slopes of the  $I$ - $V$  curves using the Van der Pauw equation and is found to be  $670 \Omega/\text{cm}^2$ . The observed low resistance is helpful for faster charge transport on the surface of the VGN.

### 3.6 Electrochemical capacitance study

The electrochemical capacitor characterization of as-grown and transferred VGN are carried out in a 3-electrode setup using Ag/AgCl as the reference electrode and 1M KOH as the electrolyte. Platinum is used as the counter electrode. For electrochemical capacitance study, out of  $2 \times 1 \text{ cm}^2$  geometrical area of the sample, only  $1 \times 1 \text{ cm}^2$  area only is exposed to the electrolyte to keep the electrical contact away from the electrolyte. The transferred VGN/OHP is the current collector and binder-free. Figures 3.7(a) and (b) show the cyclic voltammogram (CV) of the as-grown VGN/Ni and transferred VGN/OHP, at different scan rates ranging from 100-500 mV/s, respectively.

The potential window is confined to 0.5 V (-0.25 V to 0.25 V) for electric double layer formation and to exclude the possibility of faradic contribution from hydrogen storage,

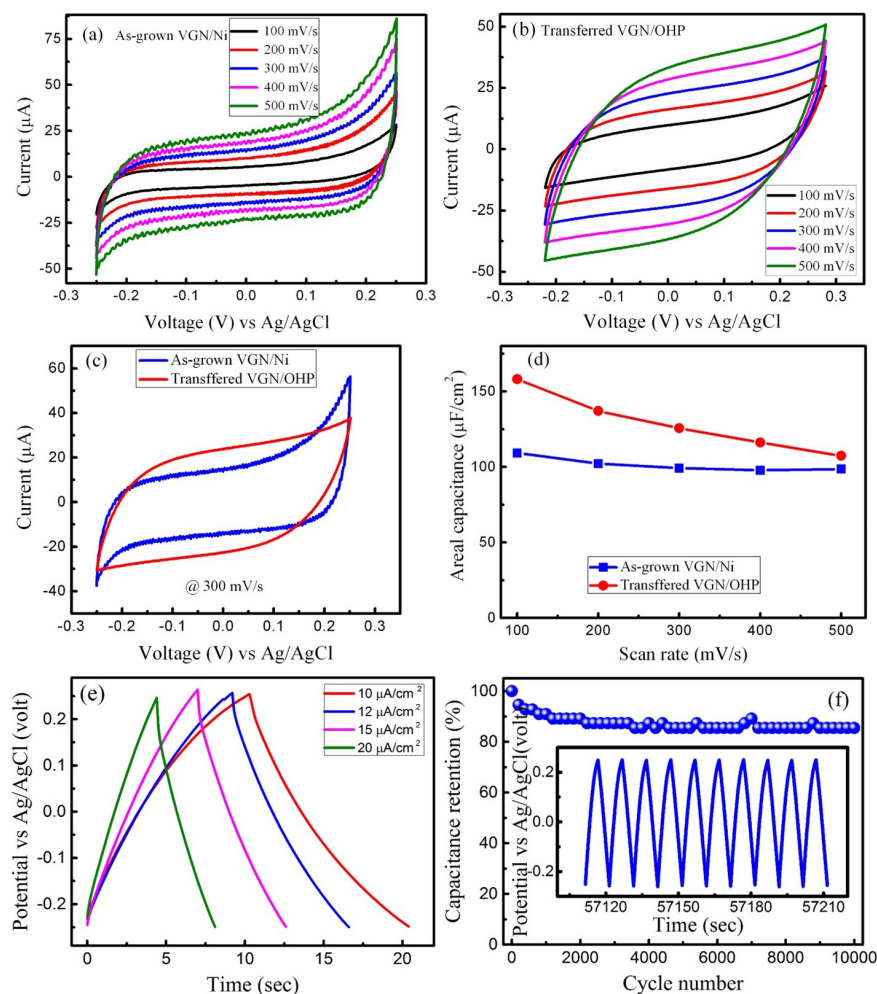


**Figure 3.7** – CV of (a) as-grown VGN/Ni and (b) transferred VGN/OHP in the 3-electrode system at different scan rates, (c) comparative CV of VGN/Ni and VGN/OHP at a scan rate of 300 mV/s, (d) plot of areal capacitance of VGN/Ni and VGN/OHP as a function of scan rate, (e) charge-discharge profile of transferred VGN at different current densities and (f) capacitive retention versus cycle number; inset shows few charge/discharge cycles.

electrode oxidation and electrolyte decomposition [140]. A similar range potential window is also reported in the literature [18, 81]. However, the potential window can be extended by improving the vertical structure's quality and using different electrolytes, which is not the focus of the current research. A near rectangular CV and its un-altered shape with scan rate confirm good supercapacitor performance. The areal capacitance is calculated from the CV using the equation 3.3. Where,  $\int idV$  represents the area under the CV curve,  $\Delta V$  is the potential window,  $s$  is the scan rate and  $A$  is the active area of the

electrode dipped in the electrolyte.

$$C_A = \frac{\int idV}{\Delta V \times A \times s} \quad (3.3)$$

The calculated areal capacitance for as-grown VGN/Ni is  $109 \mu\text{F}/\text{cm}^2$  and  $158 \mu\text{F}/\text{cm}^2$  for transferred VGN/OHP, at  $100 \text{ mV}/\text{s}$  scan rate. After the transfer, this increase in capacitance is due to the Fe contamination, as confirmed from XPS analysis. The residual Fe contamination has been proven to enhance the electrochemical capacitance of graphene [141]. For comparison, the CV plot of the as-grown VGN/Ni and transferred VGN/OHP at  $300 \text{ mV}/\text{s}$  scan rate is shown in figure 3.7(c).

Figure 3.7(d) represents the areal capacitance *vs.* scan rate for both the as-grown and transferred samples and is found to decrease with scan rate. This can be attributed to the inaccessibility of the electrolyte ion to the electrode surface at higher scan rates. The galvanostatic charge-discharge of the transferred VGN/OHP represents the symmetric and linear profile at different current densities with trivial voltage drop, which is depicted in figure 3.7(e). The obtained result indicates ideal supercapacitor behaviour for both as-grown and transferred VGN. Another property of supercapacitor is stability during large charge-discharge cycles. Hence, the charge-discharge experiment is carried out for 10000 cycles at  $12 \mu\text{A}/\text{cm}^2$  scan rate to probe the electrochemical stability of the transferred VGN and the results are shown in figure 3.7(f). The capacitance retention of the transferred VGN is found to be 86 % even after 10,000 charge-discharge cycles.

The practicability of the transferred VGN is validated by fabricating a symmetric device. The device was assembled by sandwiching KOH soaked laboratory filter paper (Whatman®41) in between two transferred VGN electrodes. The edges were then sealed using a suitable insulating polymer blend. The schematic of the fabricated device and photographic image of the electrodes are depicted in figure 3.8(a) and (b).

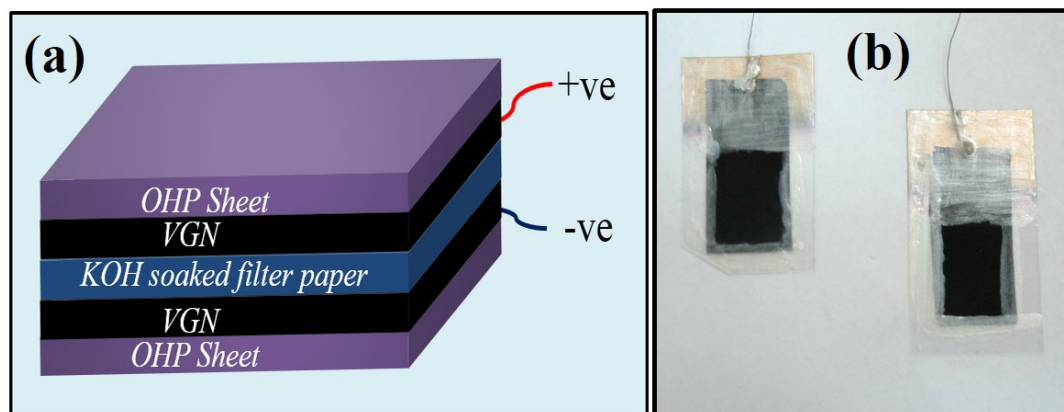


**Figure 3.8** – (a) Schematic of symmetric VGN supercapacitor device (b) Photograph of the transfer electrode for device.

The electrochemical investigation of the fabricated symmetric flexible VGN supercapacitor is carried out in a 2-electrode configuration. The CV profile of the symmetric device is shown in figure 3.9(a). The areal capacitance  $C_A$  is calculated from the CV using the following equation,

$$C_A = \frac{2 \int idV}{\Delta V \times A \times s} \quad (3.4)$$

Where,  $\int idV$  represents the area under the CV curve,  $\Delta V$  is the potential window,  $s$  is the scan rate and  $A$  is the active area of the one electrode.

The device offers a capacitance value of  $85 \mu\text{F}/\text{cm}^2$  at a scan rate of  $100 \text{ mV}/\text{s}$ . The obtained capacitance value matches the existing reports, where Al was used as the current collector [142]. Excellent charge storage stability is observed with for different scan rates (figure 3.9(b)). The linear charge-discharge profile (figure 3.9(c)) reveals good capacitive characteristic of the device. Capacitance retention of 77% is observed after 10000 cycles (figure 3.9(d)) and few continuous charge-discharge curves in inset of figure 3.9(d) shows the behaviour at high cycle number. The obtained experimental results support the suitability of VGN as a promising supercapacitor electrode material.

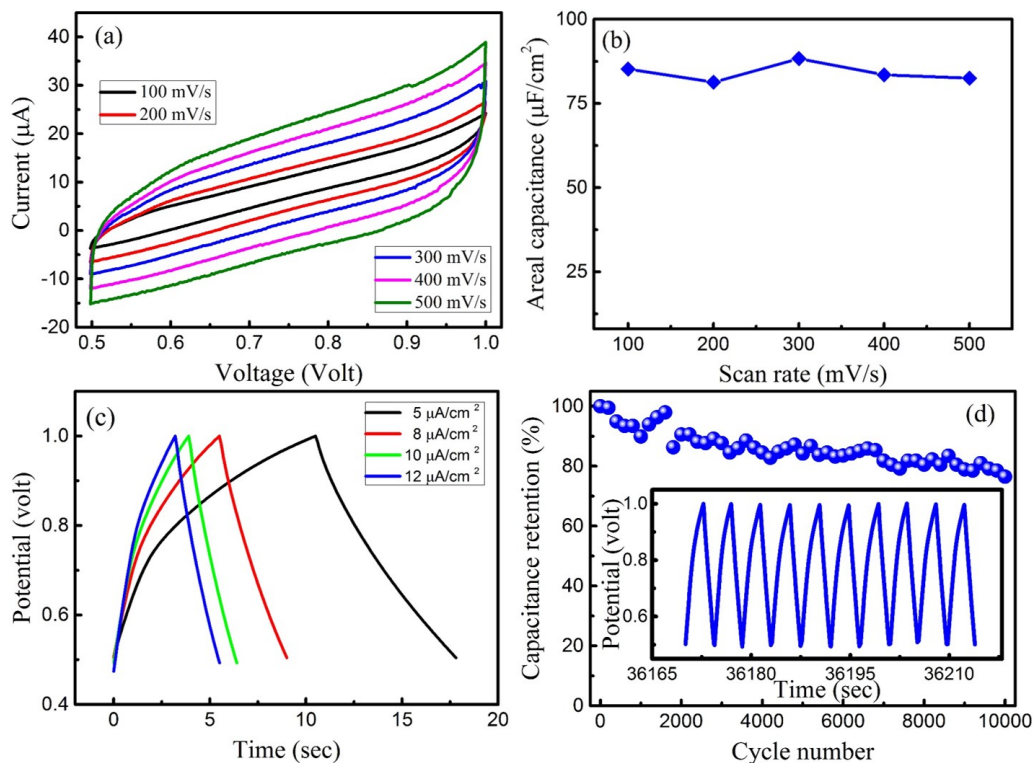


**Figure 3.9** – Electrochemical capacitance performance of the symmetric device in 2-electrode setup; (a) CV at different scan rates, (b) plot of areal capacitance *vs.* scan rate, (c) charge-discharge profile at different current densities and (d) capacitance retention *vs.* cycle number, inset of (d) represents few charge-discharge cycles.

### 3.7 Conclusion

An efficient and easily scalable, polymer-free transfer process of VGN onto the flexible substrate is presented. The preservation of morphology, structural quality and surface chemistry of the VGN is confirmed after the transfer process. The developed transfer process is straightforward to implement and highly reproducible. The meager sheet resistance makes VGN as potential candidates for electrode materials. Fabrication of the flexible supercapacitor device and electrochemical characterization results proved to use the transferred VGN electrode without additional binder and current collector. In addition to flexible device fabrication, the present scalable transfer procedure holds great promise for future applications.

# Chapter 4

## Plasma activated VGN for enhanced electrochemical capacitance

I'm convinced that art and science activate the same parts of the brain.

-Frank Wilczek

### 4.1 Introduction

Electrochemical capacitors or supercapacitors (ECs/SCs) are a potential substitute to the conventional batteries for energy storage applications due to their high charge-discharge rate, longer cycle-life and power density [53, 122, 143]. Supercapacitors are classified into two categories namely, electric double-layer capacitors (EDLCs) and pseudocapacitors (PCs), where the charge storage mechanism is due to the formation electric double layer and redox reactions at the electrode surface, respectively [144]. The EDLC has more importance than pseudocapacitors due to its better chemical stability and cyclic stability. However, the EDLC materials exhibit a few orders of lesser capacitance than the pseudocapacitors. This brings in many scopes to enhance the capacitance of EDLC materials by adapting innovative strategies which is a prime focus of current research.

Different carbon materials have been extensively studied as EDLC electrodes due to their remarkable properties like high surface area, electrical conductivity and electrochemical stability [145–148]. Vertical graphene nanosheets (VGN) are a derivative of graphene,

have drawn significant attention among the research community due to its outstanding physical and chemical properties [15, 63, 73]. Generally, VGN are 3D ensemble of interconnected vertically standing few-layer graphene sheets of few tens of nanometer-thick [21, 149]. The 3D interconnected porous network of VGN structures offers easy access to both the sides of its surface to the electrolyte ions to interact with, which is a big advantage for utilization as an electrode material [73, 74].

As-grown VGN is intrinsically hydrophobic due to its interconnected porous 3D network and hydrogen-terminated edges [27, 28]. This hydrophobic nature restricts the entire surface area to interact electrolyte. Whereas hydrophilic surfaces are most desired for better electrode wettability, which improves the interaction with electrolyte and in-turn the energy storage performance [77, 78, 150]. Hence, the VGN surface transformation to hydrophilic while retaining its unique morphology is in demand to develop a high-performance electrochemical capacitor. The density of defects, inter-sheet spacing and surface functionalization also affects the wetting nature of VGN structures [28, 41, 77, 79–82, 92]. Surface modification/activation methods like chemical activation and post-plasma treatment are widely adopted to tune the wetting properties of nanostructures, by altering the nature of defects and surface functional groups [78, 82, 83, 86]. However, chemical activation is time-consuming and there is a possibility of damaging the morphology [84, 85]. Whereas post-plasma treatment is fast and it also helps in preserving the geometry. Some research groups have reported on the SC behavior of oxygen plasma-treated VGN and explained the role of surface oxygen groups on capacitance [79, 89, 150–152]. Additionally, there are reports on the attachment of specific types of oxygenated functional groups (hydroxyl and carbonyl) found to enhance the capacitance [88, 89, 152]. Nevertheless, no detailed studies on tailoring VGN surfaces with selective oxygenated groups (hydroxyl or carbonyl) and evaluating their capacitor performance exist. A comparison of the capacitance for plasma-treated VGN from literature is tabulated in table 4.1.

Also, long-term stability of the wetting nature and surface functionalization have a significant impact on supercapacitor performance, since the electrode surface plays a vital role in the EDL formation. Yet, only a few studies are available on detailing the ageing behavior of wettability for carbon structures [153, 154]. Since plasma surface modification is a non-equilibrium process, studies on the long-term stability of the plasma-induced changes in wettability are need of the hour for potential utilization of the VGN electrodes towards supercapacitor applications.

Reference	Areal capacitance (mF/cm <sup>2</sup> )	Electrolyte
[150]	0.12 (as-grown) 0.96 (O <sub>2</sub> plasma)	1M Na Acetate and 1M MgSO <sub>4</sub>
[93]	0.16 (as-grown) 0.92 (H <sub>2</sub> plasma)	1M Na <sub>2</sub> SO <sub>4</sub>
This work	0.15 (as-grown) 1.7 (O <sub>2</sub> plasma)	1M KOH

**Table 4.1** – Comparison of the areal capacitance values for plasma-treated VGN.

In this chapter, super-hydrophilic VGN are achieved by oxygen plasma treatment, while retaining its morphology. The enhanced charge storage performance of super-hydrophilic VGN is demonstrated. Further, the significant role of oxygen plasma treatment and VGN with preferentially functionalized with specific type of oxygenated groups by *ex-situ* and *in-situ* plasma treatment is studied. Moreover, the correlation between type of oxygen functional groups (hydroxyl, carbonyl and carboxyl) with wetting nature, change in wettability with ageing and supercapacitor performance of VGN surfaces is established. The capacitance performance of VGN samples undergone oxygen plasma treatment is also compared with those treated with H<sub>2</sub>, N<sub>2</sub> plasmas. The role of the process parameters towards achieving hydrophilic VGN surfaces with long-term stability is brought out. Finally, a solid-state symmetric supercapacitor device is fabricated and used to light up a light-emitting-diode to demonstrate its practicability.

## 4.2 Tuneable oxygen plasma activation of VGN and capacitor performance

For this work, VGN were grown on SiO<sub>2</sub>/Si and carbon paper (CP) using a plasma-enhanced chemical vapor deposition technique. The detailed growth process is discussed in the previous chapter.

Post oxygen plasma treatment was carried out in two ways: (i) *ex-situ* and (ii) *in-situ* manner. In *ex-situ* treatment, the samples were exposed to ambient conditions for a few days after growth and then plasma treatment was carried out. Whereas, *in-situ* plasma treatment was carried out immediately after the growth without exposing the samples to ambient. It is to avoid the contamination by atmospheric absorbents upon exposure to ambient conditions. Plasma treatment was carried out by allowing high pure (99.99%) oxygen gas into the vacuum chamber at a flow rate of 20 sccm and the chamber pressure was  $1.2 \times 10^{-3}$  mbar. Plasma exposure studies (*ex-situ* and *in-situ*) were carried at different microwave (plasma) powers 100, 300 and 600 W, at a constant exposure time of 2 minutes. The optimum treatment time of 2 min was chosen based on our studies to achieve super-hydrophilic VGN surfaces without reducing their height [155]. The samples are named as 100 W *ex-situ*, 100 W *in-situ*, 300 W *ex-situ*, 300 W *in-situ*, 600 W *ex-situ* and 600 W *in-situ*.

### 4.2.1 Morphological analysis

Figure 4.1(a-c) illustrate the morphology of as-grown and oxygen plasma-treated VGN 600 W *ex-situ* and *in-situ* samples, respectively. The insets show respective cross-sectional FESEM images. The retention of morphology after oxygen plasma treatment is evident except a reduction of height from 1.9 to 1.1  $\mu\text{m}$  for both *ex-situ* and *in-situ* cases. The morphology and cross-sectional FESEM images of VGN treated at 100 and 300 W *ex-*

*situ* and *in-situ* are also maintained the structure unaffected [156]. The reduction in height is due to the etching of graphene edges by reactive oxygen species. However, the morphology of VGN is preserved after the oxygen plasma treatment, which is vital for its use as an electrochemical capacitor electrode material.

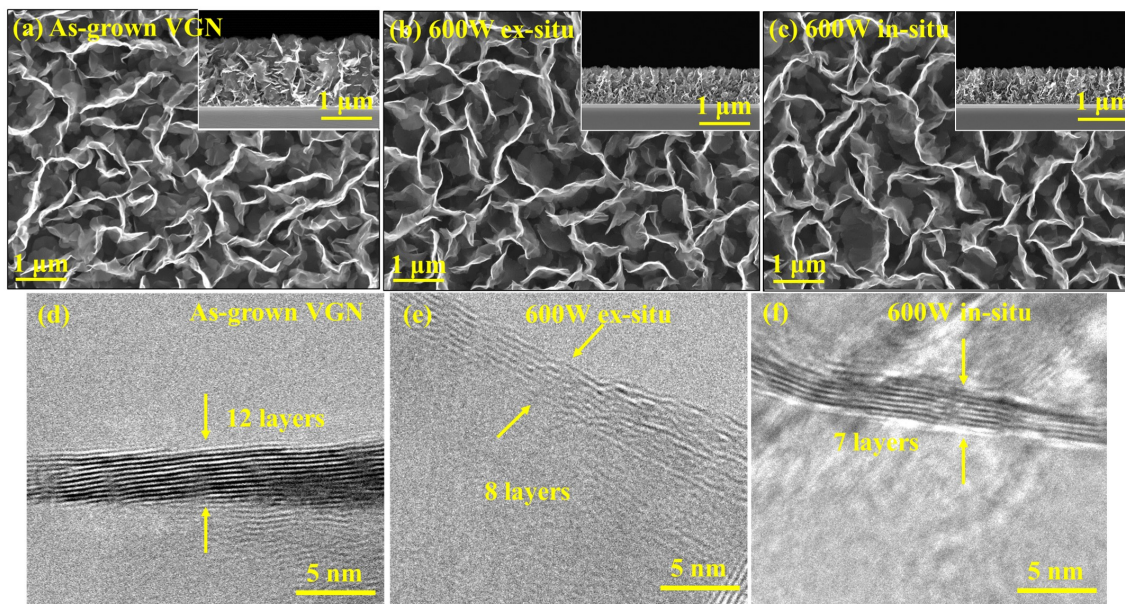


**Figure 4.1** – FESEM micrograph of (a) as-grown VGN (b) 600 W *ex-situ* and (c) 600 W *in-situ* plasma-treated VGN. Insets show the respective cross-section images. HRTEM micrograph of (d) as-grown VGN (e) 600 W *ex-situ* and (f) 600 W *in-situ* plasma-treated VGN.

In general, for the interconnected, networked structures like VGN, the inter-sheet distance is considered as pore size. In this study, the inter-sheet distance is obtained from SEM images using ImageJ software. The distribution plot is shown in figure 4.2 and an increase in the mean of inter-sheet distance is evident after plasma treatment.

The HRTEM micrographs illustrated in figure 4.1(d-f) affirm that the layered structure of the as-grown is retained in the plasma-treated VGN. A reduction in the number of layers per sheet after plasma treatment is also evidenced. For the as-grown VGN, the number of graphene layers is about twelve and reduced to nearly eight layers after the plasma treatment. It confirms the etching of the VGN by the reactive oxygen radicals during the plasma treatment.

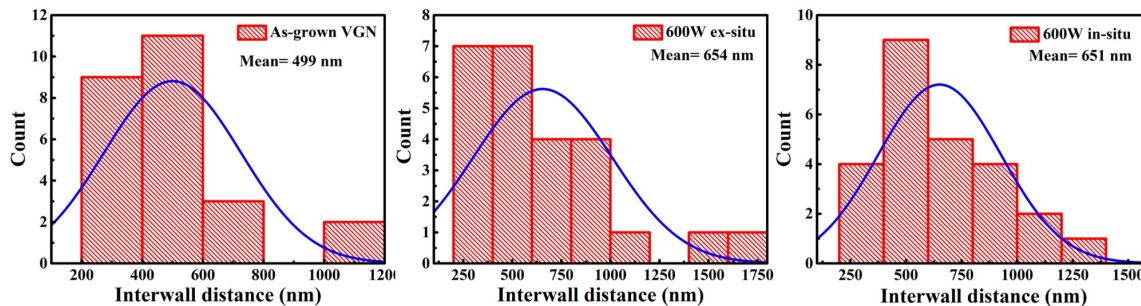


**Figure 4.2** – Inter-sheet distance distribution for as-grown VGN, 600 W *ex-situ* and 600 W *in-situ* plasma-treated VGN.

### 4.2.2 Structural analysis

Raman spectroscopy is a non-destructive technique to probe the structural properties of carbon materials [129, 136]. It gives information like structural disorder, defects, doping and strain in the investigated materials.

Figure 4.3(a) depicts the Raman spectra of VGN consisting of peaks at 1105, 1355, 1583, 1621, 2460, 2706, 2950 and 3230  $\text{cm}^{-1}$ . D (1355  $\text{cm}^{-1}$ ), G (1583  $\text{cm}^{-1}$ ), and G' (2706  $\text{cm}^{-1}$ ) are the characteristic peaks of VGN structures [83, 137, 157]. The presence of G (1583  $\text{cm}^{-1}$ ) and G'(2706  $\text{cm}^{-1}$ ) confirms the graphitic nature of the structure. Whereas, other peaks D'' (1105  $\text{cm}^{-1}$ ), D (1355  $\text{cm}^{-1}$ ), D' (1621  $\text{cm}^{-1}$ ), D+D'' (2460  $\text{cm}^{-1}$ ), D+D' (2950  $\text{cm}^{-1}$ ) and 2D' (3230  $\text{cm}^{-1}$ ) correspond to the defects induced peaks [136]. The detailed reason behind the origin of each peak is discussed in **chapter-3** section 3.3. Normalized Raman spectra of all the plasma-treated VGN are plotted with the as-grown VGN (Figure 4.3(b)). A trivial change in peak positions of D, G and G' are observed which affirms the stability of graphitic structure after the plasma treatment.

The Raman spectra are further fitted to obtain detailed information about the structural changes. The  $\text{FWHM}_D$ ,  $\text{FWHM}_G$  and  $\text{FWHM}_{G'}$  are shown in figure 4.3(c). The broadening of D, G and G' peaks indicates an increase in defect density after plasma treatment [83, 136, 158]. Further increase of FWHM in case of *in-situ* than *ex-situ* plasma-treated VGN is observed. This is attributed to the surface passivation by the atmospheric ab-

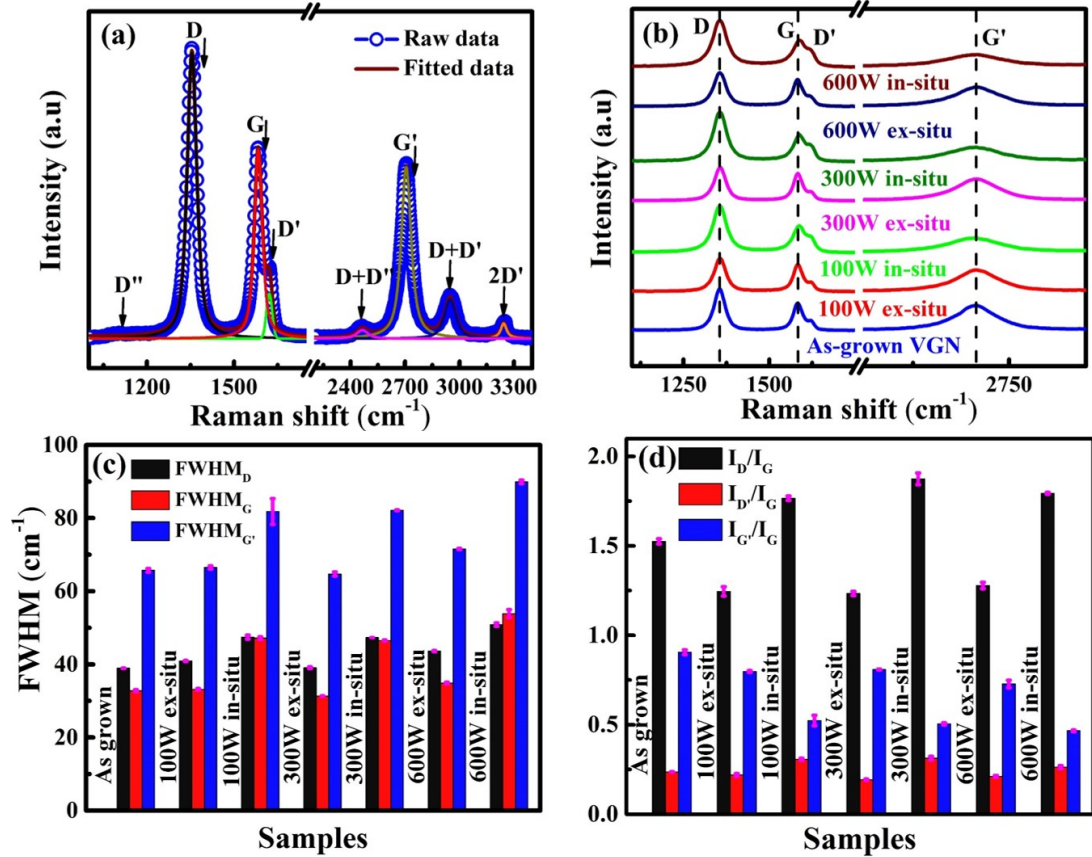


**Figure 4.3** – Raman spectra of (a) typical as-grown VGN and (b) plasma-treated VGN at different plasma powers; the variation of (c)  $\text{FWHM}_D$ ,  $\text{FWHM}_G$  and  $\text{FWHM}_{G'}$  as well as (d)  $I_D/I_G$ ,  $I_{D'}/I_G$  and  $I_{G'}/I_G$  for as-grown and plasma-treated VGN.

sorbents in case of *ex-situ* plasma-treated VGN. Whereas, *in-situ* plasma treatment is the instant extension of the growth process, resulting in less surface passivation and more unsaturated defects. Figure 4.3(d) depicts higher  $I_D/I_G$  ratio for *in-situ* than *ex-situ* plasma-treated VGN irrespective of plasma power, which confirms higher disorder formation in *in-situ* case.

Additionally, the higher  $I_{D'}/I_G$  ratio in case of *in-situ* treated samples, irrespective of the plasma power further confirms that *in-situ* plasma exposure results in higher defected VGN than *ex-situ*.  $I_{G'}/I_G$  less than one in case of *in-situ* and *ex-situ* confirm few layer graphene in the vertical sheets. So, Raman spectra results shows that the structural disorder, which is more for *in-situ* than *ex-situ* plasma-treated VGN. Moreover, the disorder found to increase with increase in plasma power.

### 4.2.3 Water contact angle measurement

The water contact angle (WCA) of as-grown and plasma-treated VGN is measured to investigate the role of plasma treatment in the wetting nature. All the WCA measurements are carried out immediately after the plasma treatment. Both the VGN grown on SiO<sub>2</sub> and CP exhibited nearly the same contact angle. For a better representation, measurement on VGN/SiO<sub>2</sub> are shown in figure 4.4(a) and (b).

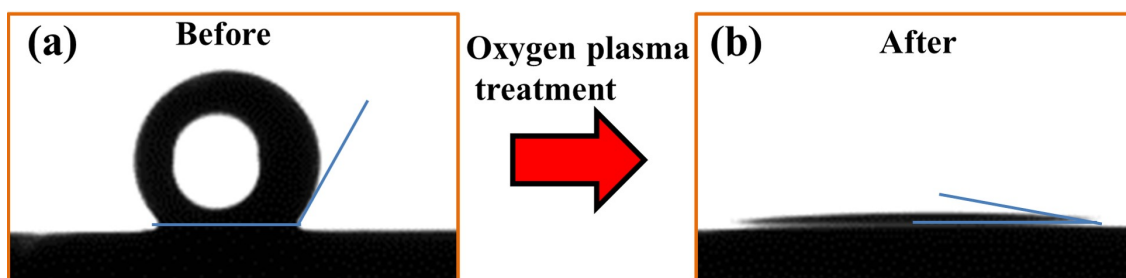


**Figure 4.4** – Water contact angle photograph of VGN (a) before and (b) after plasma treatment.

Figures 4.4(a) and (b) depict the photographic image of WCA for as-grown and plasma-treated VGN, respectively. The measured WCA for as-grown VGN is 134° (Figure 4.4(a)), which affirms the intrinsic hydrophobic nature due to its unique morphology and hydrogen-terminated bonds (C-H). Also, It is reported that the structures with 3D porous network geometry possess hydrophobic nature irrespective of the height and structural quality [76]. Whereas, oxygen plasma-treated VGN surfaces are super-hydrophilic with a WCA close to zero, regardless of the plasma power (Figure 4.4(b)). The change in wetting property is correlated to the oxygenated functional groups attached to the VGN surface due to plasma treatment. However, these findings need to be validated by quantifying oxygen content on the surface, discussed in the latter part of the chapter.

### 4.2.4 Surface chemistry analysis

A detailed XPS analysis of as-grown and plasma-treated VGN samples are carried out to evaluate and quantify the type of oxygen functional groups attached to the surface.

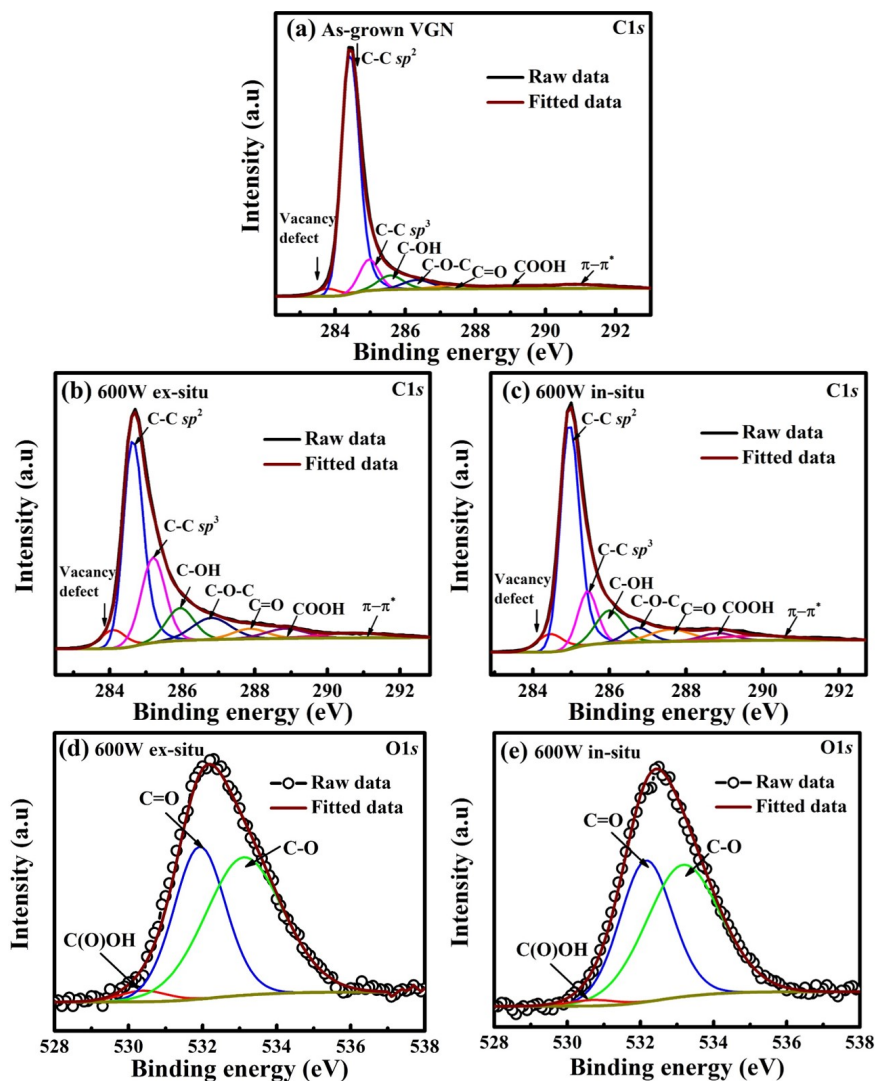


**Figure 4.5** – XPS C1s spectra for (a) as-grown VGN, (b) 600 W *ex-situ* and (c) 600 W *in-situ* plasma-treated VGN; XPS O1s spectra for (d) 600 W *ex-situ* and (e) 600 W *in-situ* plasma-treated VGN.

Figure 4.5(a) describes the high resolution C1s peak of as-grown VGN. The deconvoluted C1s spectra consists of main peaks at 283.8, 284.4 and 285 eV corresponding to the structural defects,  $sp^2$  C-C and  $sp^3$  C-C, respectively [79, 138, 139]. Alongside, less intense peaks at 285.5, 286.3, 287.3 and 288.9 eV corresponding to hydroxyl (C-OH), ether/epoxy group (C-O-C), carbonyl group (C=O) and carboxyl group (COOH), respectively are observed [79, 138, 139]. The  $\pi-\pi^*$  transition at 291 eV, that originates from the conjugated delocalized electrons indicate a higher graphitic  $sp^2$  carbon contribution.

Figures 4.5(b) and (c) show the high resolution C1s spectra for 600 W *ex-situ* and *in-situ* plasma-treated VGN, respectively. The percentage of vacancy defects is found to increase from 2.8 to 5.5 % after plasma treatment and found to be higher in *in-situ* case. Which is attributed to the increase in chemical etching and ion bombardment at higher plasma powers. An increase in  $sp^3$  C-C content is also observed after plasma treatment and it is higher in the case of *ex-situ* treated VGN samples.

Additionally, an increase in hydroxyl and carbonyl type oxygenated functional groups on VGN surface is evident after plasma treatment, and is found to be higher in case of *in-situ* treated sample. The total oxygen content increased from 1.3 to 9.7 % after the plasma treatment and is similar for all the samples. The details of the fitted data are provided in the table 4.2. It clearly shows that the higher absorbed oxygen content immediately after plasma exposure makes the surface highly polar and resulted in super-hydrophilic nature. Therefore, the structural defects and oxygenated functional groups are responsible for the change in wettability.

To validate the above findings a detailed analysis of O1s spectra of plasma-treated VGN are carried out. The O1s spectra are fitted with three peaks at 530.8, 532 and 533.7 eV corresponding to carboxyl, carbonyl and hydroxyl or epoxy/ether groups, respectively. The deconvoluted O1s spectra parameters from fitting of plasma-treated VGN (both *ex-situ* and *in-situ*) are given in table 4.3. It is also evident from figure 4.5(d) and (e) and table 4.3 that the intensity of peak corresponds to carboxyl groups at 530.8 eV, reduced and other peak increased after plasma treatment. However, the reduction is high in the case of *in-situ* plasma-treated samples. The percentage of carboxyl groups (COOH) found to reduce with an increase in plasma power and the lowest is measured to be 1.6 % for the 600 W *in-situ* VGN.

In the *in-situ* plasma treatment process, the VGN gets exposed to the highly active oxygen species immediately after growth, which saturates all the unsaturated dangling

Samples	Vacancy defect (%)	$sp^2$ C-C (%)	$sp^3$ C-C (%)	C-OH (%)	C-O-C (%)	C=O (%)	COOH (%)
As-grown	2.78	69.68	9.59	5.68	4.31	2.04	1.64
100 W <i>ex-situ</i>	4.54	55.01	16.22	7.67	5.91	2.63	4.27
100 W <i>in-situ</i>	4.62	64.52	7.35	7.98	3.99	3.46	4.09
300 W <i>ex-situ</i>	4.43	52.45	19.91	7.3	4.64	3.76	4.2
300 W <i>in-situ</i>	4.73	60.48	10.95	8.28	3.36	4.42	3.8
600 W <i>ex-situ</i>	4.81	43.09	21.62	9.49	8.76	3.6	4.1
600 W <i>in-situ</i>	5.54	52.91	12.60	10.83	4.53	6.04	3.02

**Table 4.2** – XPS C1s spectra fitted parameters for as-grown and plasma-treated VGN.

Samples	COOH (%)	C=O (%)	C-O (%)
100 W <i>ex-situ</i>	4.97	49	46.03
100 W <i>in-situ</i>	4.1	49.3	46.6
300 W <i>ex-situ</i>	2.9	49.85	47.25
300 W <i>in-situ</i>	2.73	49.99	47.28
600 W <i>ex-situ</i>	2.75	49.95	47.3
600 W <i>in-situ</i>	1.61	50.37	48.02

**Table 4.3** – XPS O1s spectra fitted parameters for as-grown and plasma-treated VGN.

bonds of as-grown VGN with the oxygen species. Thus, higher hydroxyl or epoxy/ether groups than the carboxyl groups attached to the *in-situ* plasma-treated VGN surfaces, as these groups are stable in the plasma environment.

On the other hand, in case of *ex-situ* plasma treatment, the VGN gets exposed to ambient conditions for a few days before oxygen plasma treatment. During this period the dangling bonds of as-grown VGN get saturated with carboxyl groups upon exposure to ambient conditions. This is due to the moisture in the ambient, which supplies the hydroxyl ions (-OH) to the unsaturated dangling bonds and results in further oxidation of the already attached oxygen groups and converts them into carboxyl groups (-COOH) [159, 160]. Thus, higher percentage of carboxyl groups existed in *ex-situ* plasma-treated samples than the *in-situ* treated ones. So, from the XPS analysis, an variation in surface chemistry of VGN is observed by oxygen plasma treatment under different conditions (*ex-situ* and *in-situ*).

### 4.2.5 Electrochemical capacitance study

Supercapacitive performance of as-grown and plasma-treated VGN are studied by exposing a  $1 \times 1 \text{ cm}^2$  area to 1M KOH electrolyte in a 3-electrode setup.

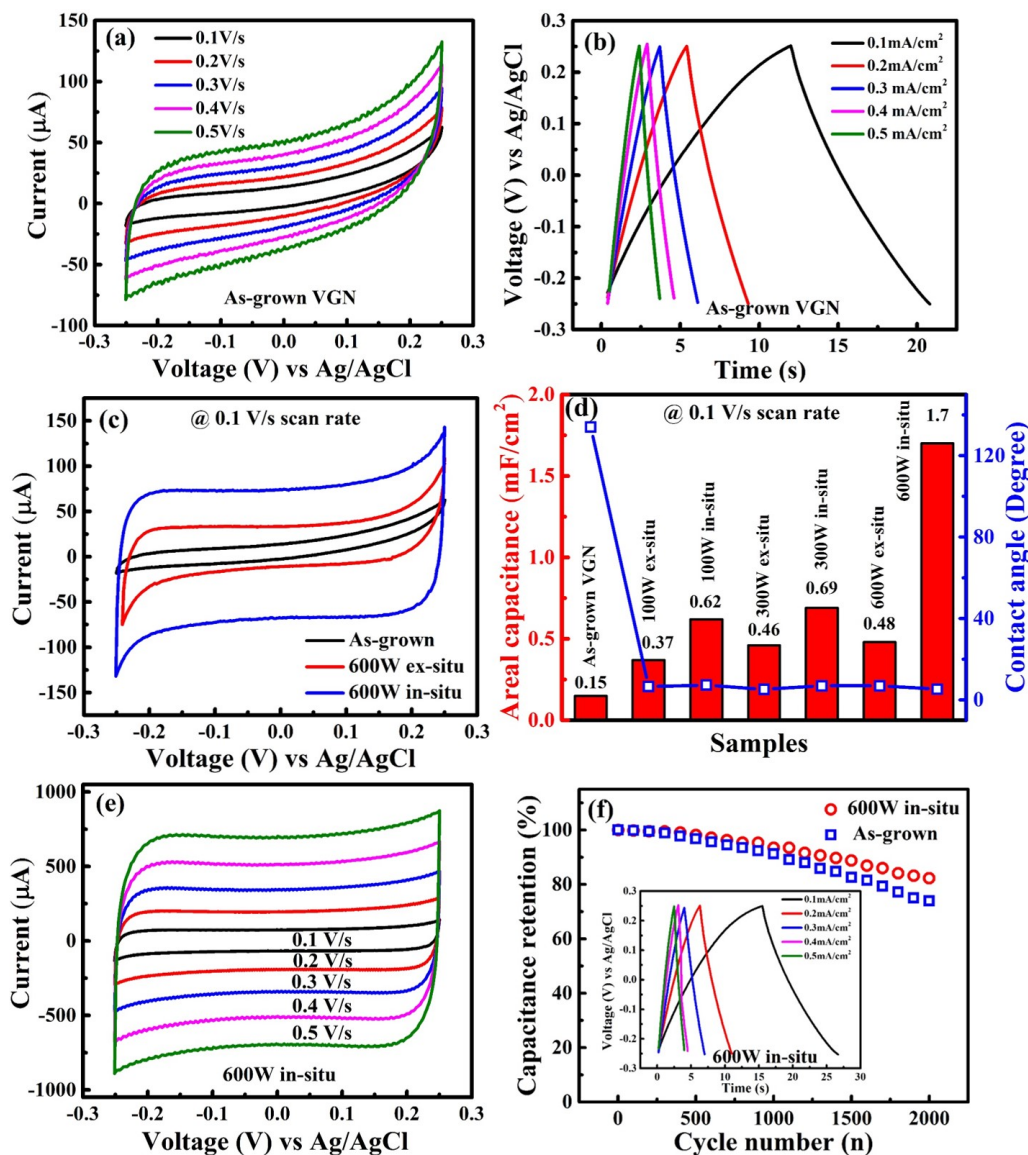


**Figure 4.6** – (a) CV and (b) CD curve of as-grown VGN, (c) CV comparison of as-grown and 600 W *ex-situ* and *in-situ* plasma-treated VGN, (d) areal capacitance of all the samples, (e) CV of 600 W *in-situ* plasma-treated VGN, and (f) capacitance retention for as-grown and 600 W *in-situ* plasma-treated VGN, inset shows the CD for 600 W *in-situ* plasma-treated VGN.

The areal capacitance is calculated from the cyclic voltammogram (CV) using the following equation,

$$C_A = \frac{\int idV}{\Delta V \times A \times s} \quad (4.1)$$

where,  $\int idV$  represents the area under the CV curve,  $\Delta V$  is the potential window,  $s$  is the scan rate and  $A$  is the active area of the electrode exposed to the electrolyte.

Figures 4.6(a) and (b) represent the CV measured at different scan rates and the charge-discharge (CD) profile at different current densities of the as-grown VGN. A near rectangular CV profile and linear CD curve signify a good capacitive characteristic. Figure 4.6(c) represents CV comparison of as-grown VGN and both *ex-situ* and *in-situ* 600 W plasma-treated VGN at 0.1 V/s. *In-situ* plasma-treated VGN shows high area under the CV than *ex-situ* plasma-treated VGN indicating higher capacitance value. CV comparison of other plasma-treated VGN (100 W and 300 W) also follows the similar behaviour, the areal capacitance plot is depicted in figure 4.6(d). The highest capacitance value 1.7 mF/cm<sup>2</sup> is obtained for 600 W *in-situ* plasma-treated VGN. Figure 4.6(d) also shows the super-hydrophilic nature in plasma-treated VGN irrespective of the plasma power. Figure 4.6(e) represents the CV measured at different scan rates from 0.1 to 0.5 V/s and inset of figure 4.6(f) shows the CD profile of the . A rectangular CV profile and the linear CD curve signify ideal capacitive characteristic of the 600 W *in-situ* plasma-treated VGN. The capacitance retention increased after the plasma treatment from 73 to 85% for 2000 CD cycles, shown in figure 4.6(f). The increase in capacitance is attributed to the super-hydrophilic nature of plasma-treated VGN surface.

The oxygen functionalization or hydrophilicity also can be achievable by a simple alcohol bath. So for the comparison sake, alteration of the wetting nature of the hydrophobic as-grown VGN structures is carried out by simply soaking in ethyl alcohol for one day and then cleaned it by dipping in de-ionized (DI) water for several times. The as-grown VGN also possessed super-hydrophilic nature after alcohol soaking. The measured capacitance

of the alcohol soaked VGN is  $1.16 \text{ mF/cm}^2$ , but found to reduce rapidly to  $0.49 \text{ mF/cm}^2$  after 1000 cycle, the corresponding CV plots are shown in figure 4.7. The reduction in capacitance after 1000 CV cycles is attributed to the decrease in oxidation/reduction reactions reagent. Whereas, the plasma-treated VGN samples possess a stable CV profile even after 2000 CD cycles and a higher capacitance value of  $1.7 \text{ mF/cm}^2$ . It confirms that the oxygen functionalization of VGN is more stable through plasma-treated than alcohol treatment.

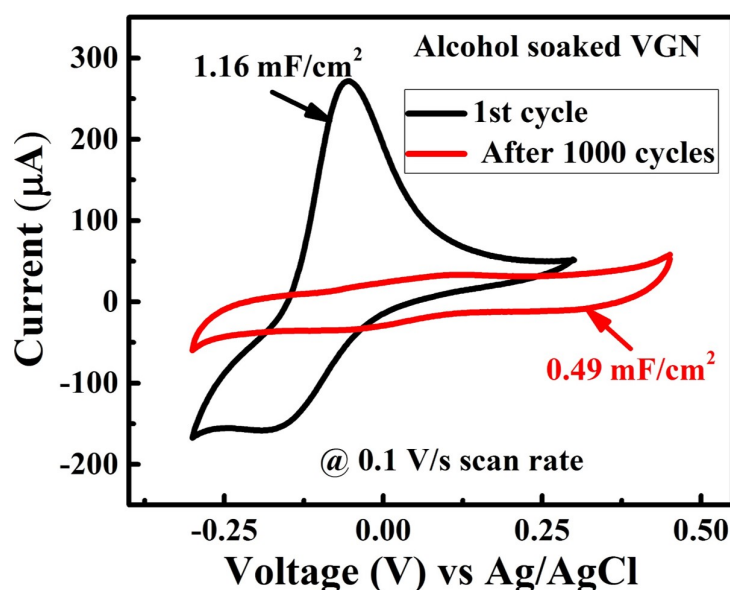


**Figure 4.7** – CV of 1<sup>st</sup> and 1000<sup>th</sup> cycles for alcohol soaked VGN at 0.1 mV/s.

The electroactive surface area is more important for the EC electrodes than the electrode's entire surface area. Hence, the electrochemically active surface area from capacitive current ( $I_{dl}$ ) vs. scan rate (V/s) is calculated to know the significant role of wetting nature/surface functionalities towards enhancing the interacting surface area, which in turn influence the capacitance value [161, 162]. The corresponding plot of ( $I_{dl}$ ) vs. scan rate (V/s) are shown in figure 4.8. It is evident from the linear variation of current with scan rate that the EDLC is the dominant charge storage mechanism. Here, we adopted the widely used 'Jellium model' to obtain the electrochemically active surface area [50]. The calculated active surface area values are found to be  $8 \text{ m}^2/\text{g}$  for as-grown VGN,  $60$

$\text{m}^2/\text{g}$  for 600 W *ex-situ* and 157  $\text{m}^2/\text{g}$  for 600 W *in-situ* plasma-treated VGN. So, it is evidenced that the increase in active surface area after the plasma treatment.

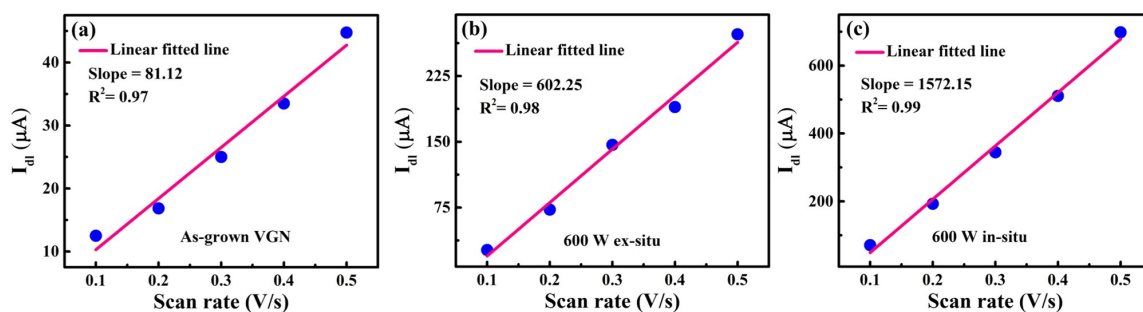


**Figure 4.8** – Mean current passed during anodic/cathodic scan for (a) as-grown VGN, (b) 600 W *ex-situ* and (c) 600 W *in-situ* as a function of scan rate.

In order to obtain information about electrode-electrolyte interaction, electrochemical impedance spectroscopy (EIS) was carried out [93]. Figure 4.9 depicts the impedance responses of as-grown and plasma-treated VGN, at a perturbation of 10 mV in the frequency range of 100 kHz to 10 mHz. The  $Z'$  intercept in the Nyquist plot is the measure of equivalent series resistance ( $R_s$ ). Equivalent circuit used to fit the impedance spectra is shown in the inset of figure 4.9(a). The components of the equivalent circuit are the equivalent series resistance ( $R_s$ ), double layer capacitance ( $C_{dl}$ ), charge transfer resistance ( $R_{ct}$ ), and Warburg element/distributed charge storage component ( $Z_w$ ) due to the porous nature of the electrode.

The  $R_s$  values measured are 2.2, 1.7, and 1.2  $\Omega$  for as-grown VGN, 600 W *ex-situ* and 600 W *in-situ* plasma-treated VGN, respectively. It is observed that the  $R_s$  value is found to reduce after the plasma treatment. The lowest  $R_s$  of *in-situ* plasma-treated VGN ensures less resistance to ionic current. Figure 4.9(b) illustrates the phase angle versus frequency. The maximum phase angle values obtained for as-grown VGN, 600 W *ex-situ* and 600 W *in-situ* plasma-treated VGN are 79.7°, 81°, and 87.5°, respectively. In general, the phase angle of 90° indicates an ideal capacitor behavior. The increase in phase angle close to 90° after the plasma treatment emphasizes an improved capacitor behavior.

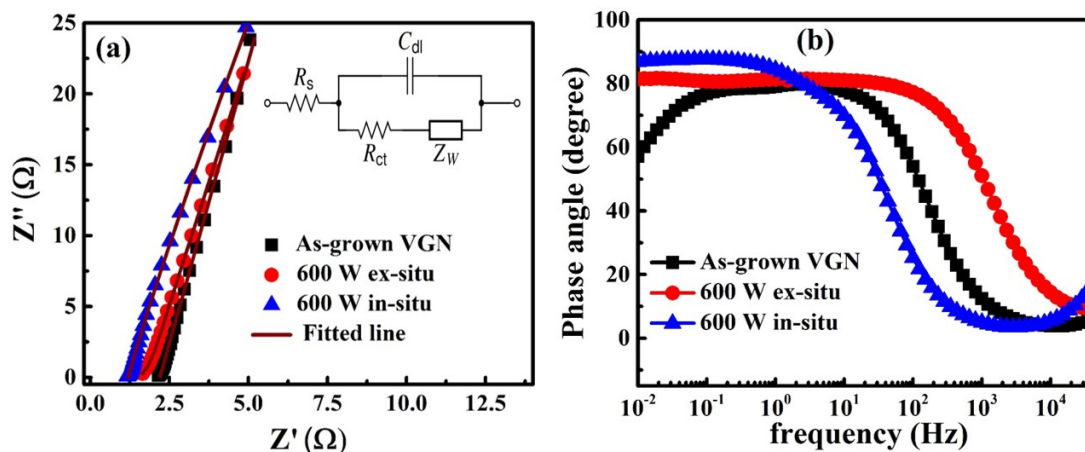
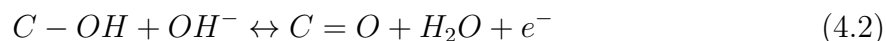


**Figure 4.9** – Impedance responses of as-grown VGN, 600 W *ex-situ* and 600 W *in-situ* plasma-treated VGN: (a) Nyquist plot, inset represents the equivalent circuit of fitted impedance spectra and (b) Bode plot

#### 4.2.6 Discussion

It has been reported that both the hydroxyl and carbonyl type of oxygen functionalization increase pseudocapacitance in addition to the electric double layer capacitance because of the reversible redox reactions [88, 163, 164]. The reactions are given below [146, 165, 166],



In addition, the oxygenated functional groups are found to increase electrode's wettability and gives highly access for the electrolyte ions to interact with interior surfaces. On the other hand, the carboxyl type of oxygen functional groups cause a reduction in capacitance. As the carboxyl groups are thermally less stable, they are detrimental for achieving higher capacitance through Faradic reactions. Whereas, the hydroxyl and carbonyl groups are thermally more stable and thus, they are the most preferred functional groups to enhance the capacitance [88, 163].

A schematic representation of the plasma-treated VGN surfaces with different oxygen

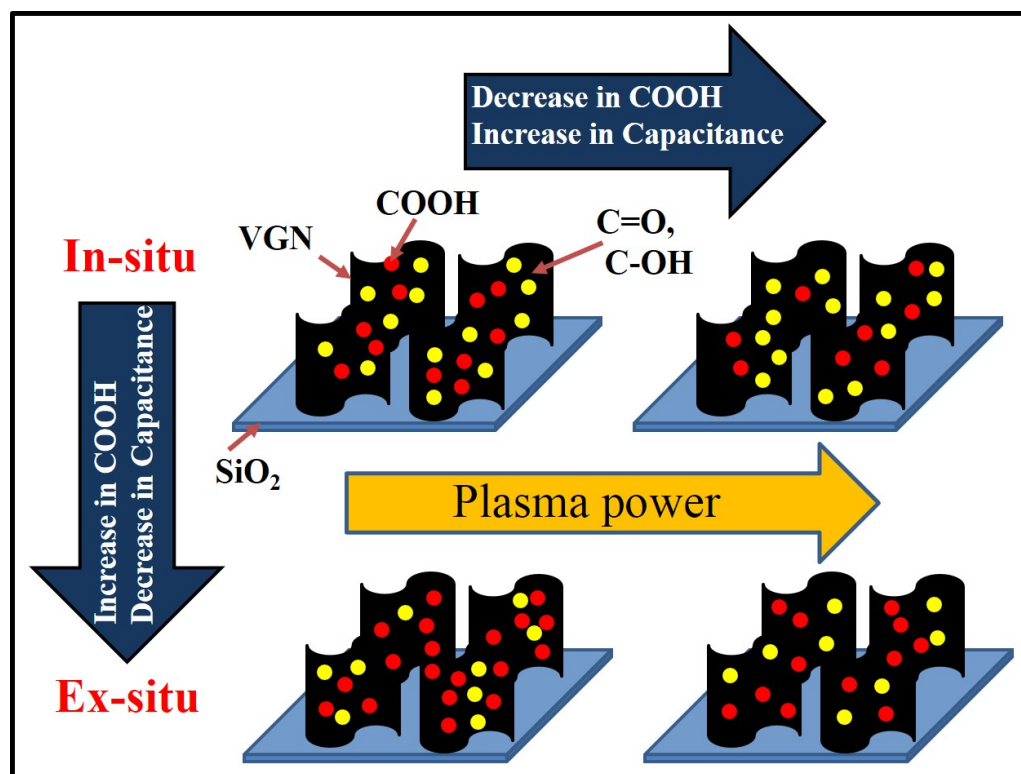


**Figure 4.10** – Schematic representation oxygenated functional groups attached to the plasma-treated VGN surfaces and dependence on capacitance.

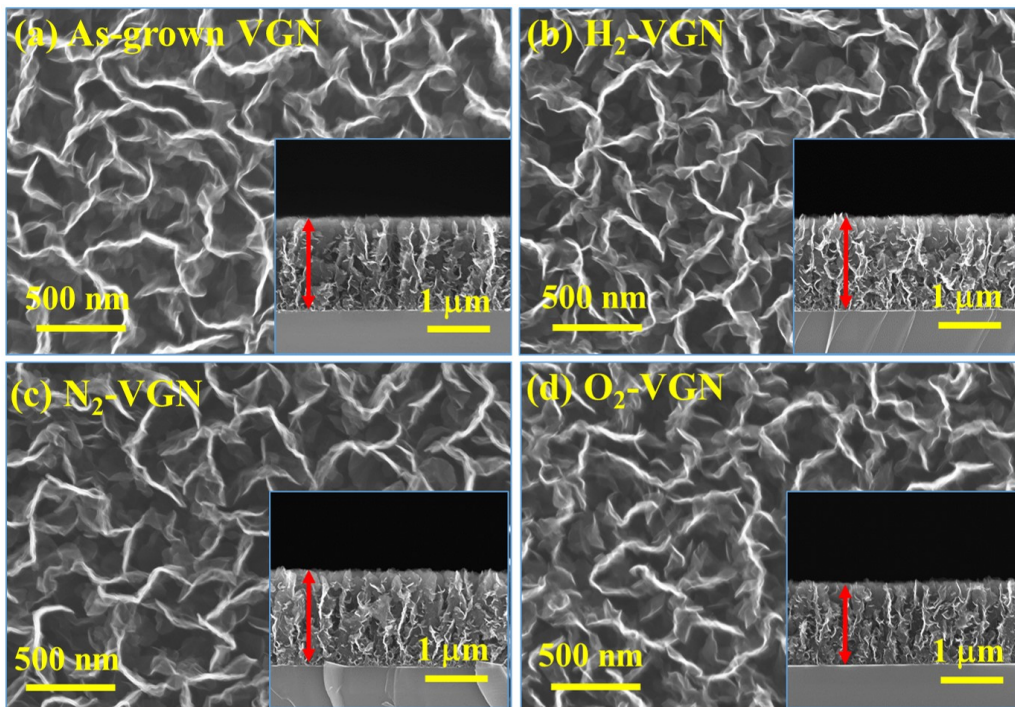
functional groups determined by the plasma treatment conditions is illustrated in figure 4.10 to understand the whole mechanism. It is evident that the capacitance increased with plasma power regardless of how the plasma treatment is conducted. Additionally, *in-situ* plasma-treated VGN exhibited higher capacitance than *ex-situ* treated one, regardless of the plasma power. However, at a given plasma power, *in-situ* plasma-treated VGN is found to consist of higher hydroxyl and carbonyl groups and hence more capacitance.

Therefore, a strong correlation between capacitance performance, WCA and oxygenated functional groups (hydroxyl, carbonyl) is evident. The obtained results affirm that the *in-situ* oxygen plasma treatment of VGN is advantageous than *ex-situ* one towards achieving higher capacitor performance.

### 4.3 Different plasma activation of VGN and capacitor performance

The previous study confirms that oxygen plasma treatment transforms the VGN to hydrophilic and improves the wettability of the electrode. Also, the *in-situ* manner of plasma treatment is preferable than *ex-situ* to achieve higher capacitance. For a comparison sake *in-situ* H<sub>2</sub> and N<sub>2</sub> plasma treatment of VGN is performed and its influence on both wettability and capacitance are studied. The plasma treatments were carried out at 600 W microwave power for 2 minutes of exposure time. The samples are named as as-grown VGN, H<sub>2</sub>-VGN, N<sub>2</sub>-VGN and O<sub>2</sub>-VGN.

#### 4.3.1 Morphological analysis



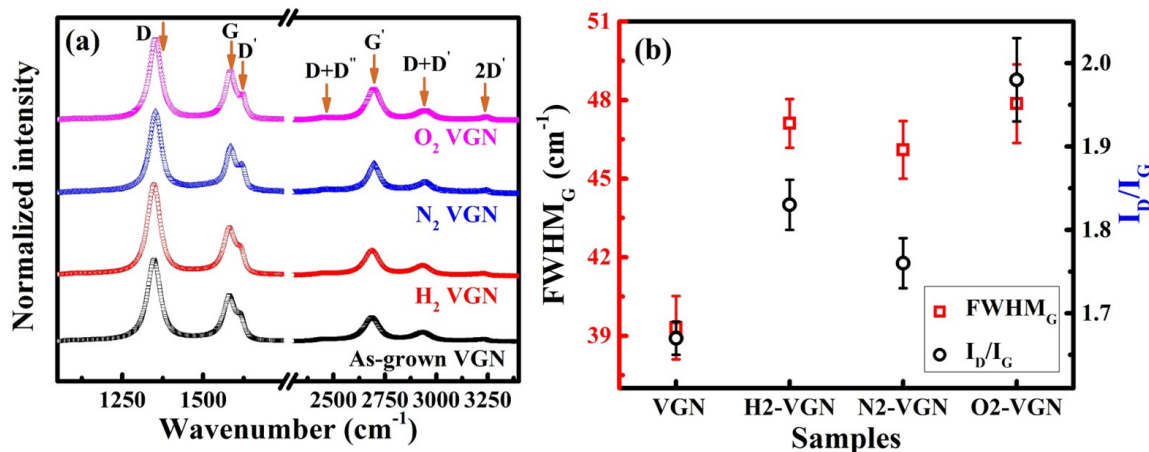
**Figure 4.11** – FESEM micrographs of (a) as-grown VGN (b) H<sub>2</sub>-VGN (c) N<sub>2</sub>-VGN and (d) O<sub>2</sub>-VGN.

Figure 4.11 illustrates the FESEM morphology with the respective cross-sectional images

of as-grown and plasma-treated VGN. The unique 3D-interconnected morphology of the VGN is retained after the plasma treatment. Apparently, a significant reduction in vertical height (from 1.8 to 1.2  $\mu\text{m}$ ) of the graphene sheets under oxygen plasma treatment and a trivial change in height under hydrogen and nitrogen plasma is observed. This is attributed to the chemical etching caused by the reactive nature of oxygen ions compared to the hydrogen and nitrogen ions.

### 4.3.2 Structural analysis

The structural characterization of as-grown and plasma-treated VGN are carried out by Raman spectroscopy to find the structural change after plasma treatment [129, 158]. Figure 4.12(a) depicts the Raman spectra for as-grown VGN and plasma-treated VGN. The peak details and their origins are discussed in **chapter-3** section 3.3.



**Figure 4.12** – (a) Raman spectra of as-grown and different plasma-treated VGN and (b) change in  $\text{FWHM}_G$  and  $I_D/I_G$  after plasma treatment.

Figure 4.12(a) shows the presence characteristic peaks which confirm the stability of VGN after the plasma treatment. The obtained full width at half maxima of G ( $\text{FWHM}_G$ ) peak and ratio of D and G peak intensities ( $I_D/I_G$ ) from the fitted Raman spectra are plotted in figure 4.12(b). The increase in  $\text{FWHM}_G$  and  $I_D/I_G$  confirm increase in defect density after the plasma treatment [129, 158]. This increase in defect density is due to the etching of VGN in the plasma atmosphere, which leads to a change in local structure.

### 4.3.3 Contact angle measurement and surface energy calculation

To signify the role of plasma treatment in tuning the wetting nature of VGN by modulating its surface energy, contact angle measurements of these samples are carried out. Further, quantification of the surface energy of plasma-treated VGN samples is carried out by measuring the contact angle using two different liquids, namely water and glycerol. Figure 4.13(a) and (b) illustrates the contact angle images of the as-grown and plasma-treated VGN samples in water and glycerol.

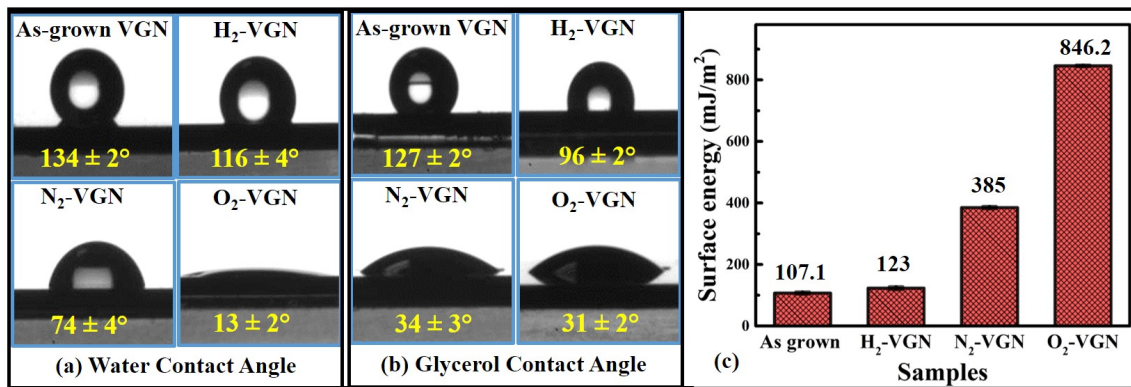


**Figure 4.13** – (a) Water contact angle (WCA) and (b) Glycerol contact angle (GCA) of as-grown and different plasma-treated VGN samples; and (c) Bar graph representing the calculated surface energy of the as-grown and plasma-treated VGN.

Transformation in the wetting nature of the O<sub>2</sub>-VGN from hydrophobic to hydrophilic is evident from the WCA images. The as-grown VGN found to be hydrophobic with contact angles of 134±2°, 127±2° in water and glycerol, respectively. Apart from the as-grown VGN, the H<sub>2</sub>-VGN also possesses a hydrophobic (WCA= 116±4°) nature. It is attributed to the surface passivated non-polar C-H bonds caused by the hydrogen plasma treatment. On the other hand, both N<sub>2</sub>-VGN and O<sub>2</sub>-VGN are found to be hydrophilic. Amongst, the O<sub>2</sub>-VGN possesses an inclination to more hydrophilic nature. This is attributed to the absorbed polar oxygen functional groups of the O<sub>2</sub>-VGN samples. Additionally, both the nitrogen and oxygen are highly electronegative, which shows a high affinity towards

water molecules and hence the hydrophilic nature.

To substantiate the role of surface functionalities in influencing the wetting characteristics of the plasma-treated VGN, the surface energy of these samples are calculated using Fowkes model by the following equation [130],

$$\frac{\gamma_l(\cos\theta + 1)}{2} = (\gamma_l^d)^{1/2}(\gamma_s^d)^{1/2} + (\gamma_l^p)^{1/2}(\gamma_s^p)^{1/2} \quad (4.4)$$

where  $\gamma_l$  is the liquid free surface energy and  $\gamma_l^d$ ,  $\gamma_s^d$ ,  $\gamma_l^p$ ,  $\gamma_s^p$  are the dispersive and polar components of liquid and solid, respectively. The obtained surface energy values are plotted and shown in figure 4.13(c). Surface energy for as-grown VGN, H<sub>2</sub>-VGN, N<sub>2</sub>-VGN and O<sub>2</sub>-VGN is found to be 107.1, 123, 385 and 846.2 mJ/m<sup>2</sup>, respectively. The surface energy of as-grown VGN is found to increase up to nearly eight times after the oxygen plasma treatment. Amongst, the H<sub>2</sub>-VGN exhibited the lowest variation in surface energy. The observed surface energy, reflects on the wetting nature of the as-grown and plasma-treated VGN.

#### 4.3.4 Surface chemistry analysis

The chemical structure and bonding of the plasma-treated VGN are evaluated using XPS.

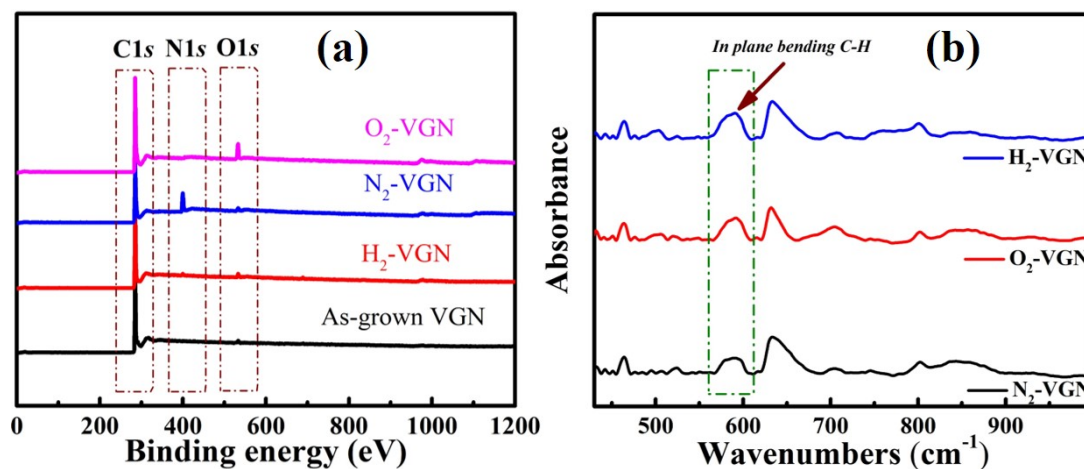


**Figure 4.14** – (a) XPS spectra of as-grown and different plasma-treated VGN and (b) FTIR spectra for different plasma-treated VGN.

Figure 4.14(a) shows the XPS survey spectra of these samples consist of peaks corresponding to C1s, N1s and O1s. It is clearly evident that the peak corresponds to oxygen (O1s) is significantly increased for O<sub>2</sub>-VGN, which indicates the increase in oxygen content. This is attributed to i) plasma functionalization and ii) chemical absorption of oxygen by the plasma etched VGN edges upon exposure to the ambient atmosphere. Among the samples, the O<sub>2</sub>-VGN possessed higher oxygen content of 9.5 % compared to H<sub>2</sub> (4.53 %) and N<sub>2</sub> (6.52 %) VGN samples. In addition to the oxygen, a 15 % nitrogen content is also evident in the case of N<sub>2</sub>-VGN. Fourier-transform infrared spectroscopy (FTIR) spectra show an increase in the in-plane C-H bending mode, confirming more hydrogen termination after H<sub>2</sub> plasma treatment (figure 4.14(b)).

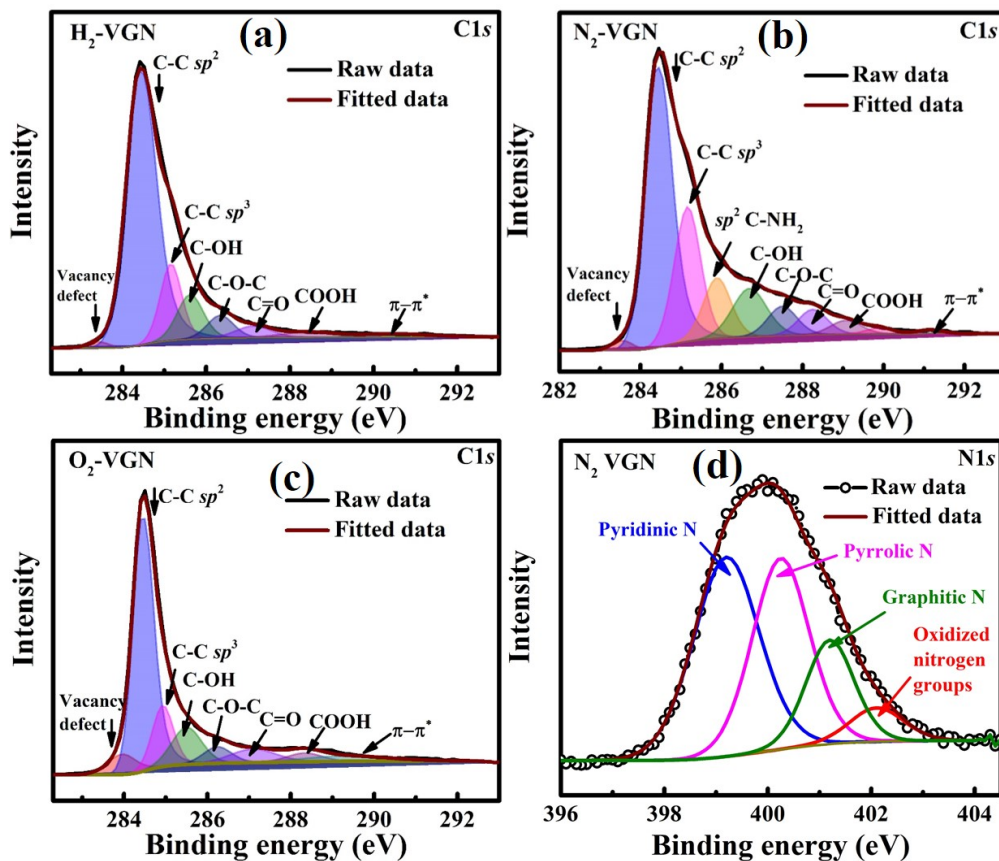


**Figure 4.15** – C1s XPS spectra for different plasma-treated VGN (a-c) and N1s XPS spectra of N<sub>2</sub> plasma-treated VGN.

Furthermore, the C1s spectra of the samples are deconvoluted to substantiate the vari-

ation in chemical bonding of the VGN that occurred with various plasma treatments (figure 4.15). The fitted C1s spectra consists of major peaks corresponding to C-C  $sp^2$ , C-C  $sp^3$ , C-OH, C-O-C, C=O and COOH [79, 138, 139]. The  $\pi-\pi^*$  peak originates from the conjugate delocalized electrons, indicates higher graphitic contribution. It is also evident that the C-C  $sp^3$  bonding has increased after plasma treatment and is higher in the case of  $N_2$  plasma-treated ones. Also,  $sp^2$  C-NH<sub>2</sub> i.e., the nitrogen incorporation to the graphene matrix, is observed. Furthermore, the  $N_2$  plasma-treated VGN possessed pyrrolic and pyridine dominated N-doping (figure 4.15(d)). The observed changes are attributed to the local variation in bonding due to opening up of the carbon rings by the plasma treatment.

### 4.3.5 Electrochemical capacitance study

The electrochemical performance of as-grown and plasma-treated VGN are carried out using a three-electrode configuration, where 1M KOH is used as the electrolyte.

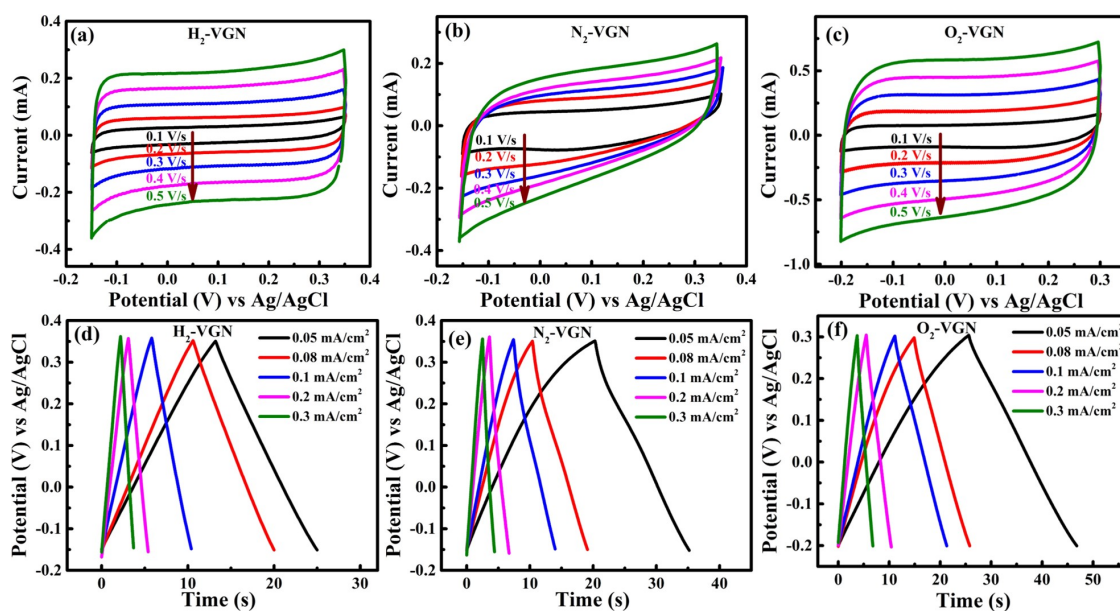


**Figure 4.16** – CV and CD for (a, d) H<sub>2</sub>-VGN, (b, e) N<sub>2</sub>-VGN and (c, f) O<sub>2</sub>-VGN.

Figure 4.16 illustrates the cyclic voltammogram (CV) and charge-discharge (CD) curve at different scan rates (0.1 to 0.5 V/s) and current densities (0.05 to 0.3 mA/cm<sup>2</sup>) respec-

tively. The CV and CD of these samples are carried out over 0.5 V potential window. A near rectangular CV and triangular CD profiles of these samples confirm a good capacitive behavior. The CD shape deviation from linear in case of N<sub>2</sub> VGN confirms the presence of pseudocapacitance due to pyrrolic and pyridine dominated N-doping, which was observed from the XPS.

A comparative CV profiles of these samples are given in figure 4.17(a). It is evident that the area under the CV curve is significantly increased after plasma treatment and is found to be highest in the case of O<sub>2</sub>-VGN followed by N<sub>2</sub>-VGN and H<sub>2</sub>-VGN. This confirms an enhancement in specific capacitance of VGN with the plasma treatment and is highest for oxygen plasma-treated VGN.

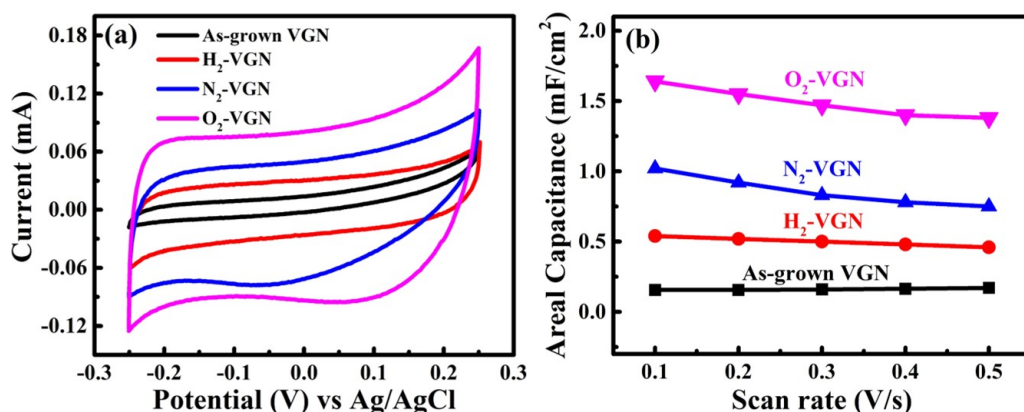


**Figure 4.17** – (a) CV comparison at 0.1 V/s and (b) areal capacitance *vs.* scan rate profile, for as-grown and different plasma-treated VGN.

Figure 4.17(b) depicts the rate capability of the as-grown and plasma-treated VGN samples at different scan rates indicating high stability. The value of capacitance for as-grown, H<sub>2</sub>-VGN, N<sub>2</sub>-VGN and O<sub>2</sub>-VGN at 0.1 V/s are 0.15, 0.56, 1.04 and 1.7 mF/cm<sup>2</sup>, respectively. All the plasma-treated VGN showed enhancement in capacitance. This is attributed to the change in wetting nature due to the different functionalization of the VGN surface. A ten-fold increase in capacitance is evident in O<sub>2</sub>-VGN. While, both N<sub>2</sub>-VGN, H<sub>2</sub>-VGN are also showed an enhancement in capacitance of VGN but lower compared to O<sub>2</sub>-VGN.

### 4.3.6 Discussion

The change in capacitance with plasma treatment is attributed to the change in surface chemistry and wetting, which is specific to the type of plasma treatment ( $H_2/N_2/O_2$ ). The XPS analysis clearly showed the variation in surface functionalization of the VGN treated in different plasma. Since, oxygen functionalization is evident in all the plasma-treated samples, it could have contributed to the capacitance enhancement. However, the amount of absorbed oxygen is higher for  $O_2$ -VGN and followed by  $N_2$ -VGN,  $H_2$  VGN and pristine. This trend confirms a correlation between oxygen content and capacitance values. Furthermore, among the  $N_2$ -VGN and  $H_2$ -VGN the former possesses almost double the capacitance than the later. It is attributed to the difference in oxygen content and the N-doping (dominated by pyrrolic and pyridinic) in  $N_2$ -VGN, which contributes to the pseudocapacitance. The deviation of the CD curve from the triangular shape in  $N_2$ -VGN confirms the pseudocapacitance nature of charge storage. The above facts attribute the augmented capacitance of VGN after plasma treatment and the significant role of wetting in the capacitance performance.

## 4.4 Temporal stability of oxygen plasma activated VGN

The previous study shows that the *in-situ* plasma turns the surface hydrophilic and enhances the capacitance. Also, oxygen plasma treatment is most suitable for capacitance enhancement. Since plasma activation is a non-equilibrium process, studies on the hydrophilic surface's long term stability is needed for the potential utilization of VGN electrodes towards energy applications. Therefore the WCA for 100, 300, 600 W *in-situ* plasma-treated VGN is measured over a long time. The samples are named as 100 W, 300 W and 600 W.

### 4.4.1 Water contact angle measurement

In order to verify the stability of the wetting nature, which is an important characteristic of a good supercapacitor electrode material, the water contact angle (WCA) of both as-grown and plasma-treated VGN surfaces are measured in an interval of 7 days, over a period of 90 days. The water contact angle versus ageing time is illustrated in figure 4.18 for as-grown and different plasma-treated VGN (100 W, 300 W and 600 W).

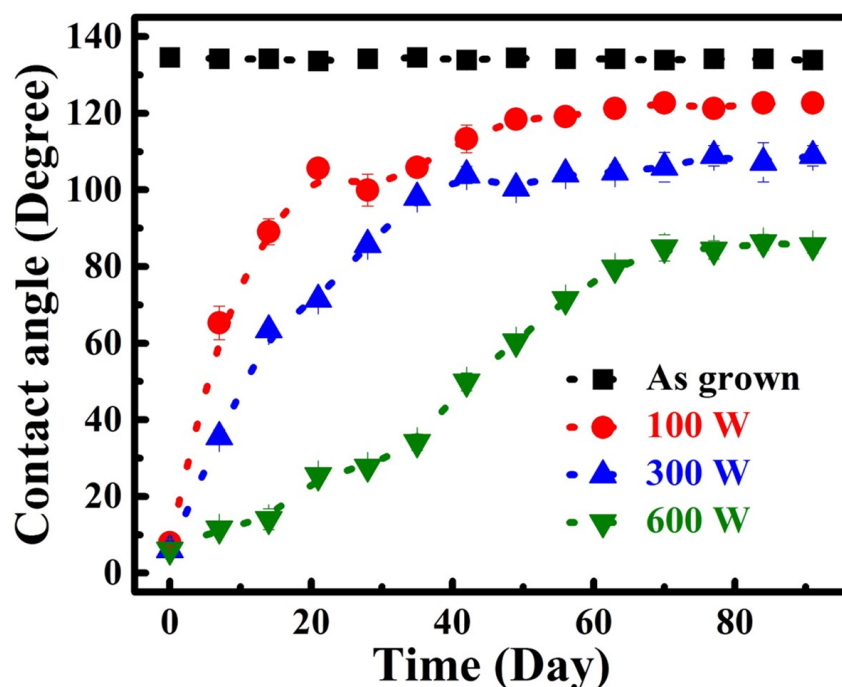


**Figure 4.18** – Contact angle *vs.* ageing time of as-grown and plasma-treated VGN at different powers.

As-grown VGN exhibited excellent stability of WCA at  $134^\circ$  throughout the period (90 days). On the other hand, a significant transformation from super-hydrophilic to hydrophobic is observed in plasma-treated VGN surfaces at different plasma power. However, the rate of change in wettability, from super-hydrophilic to hydrophobic, is slowed down with the increase in microwave power. Amidst, the slowest ageing rate is observed for the VGN treated at 600 W microwave power, for which WCA is found to be stable at  $80^\circ$  even after 90 days of ageing.

#### 4.4.2 Surface chemistry analysis

To investigate the difference in rate of change of wetting, XPS measurements are carried out for the aged samples after 90 days of ageing. It is found that there is a decrease in O/C percentage with the aging process and among all the samples, the 600 W *in-situ* one shows a less reduction in O/C percentage (figure 4.19(a)).

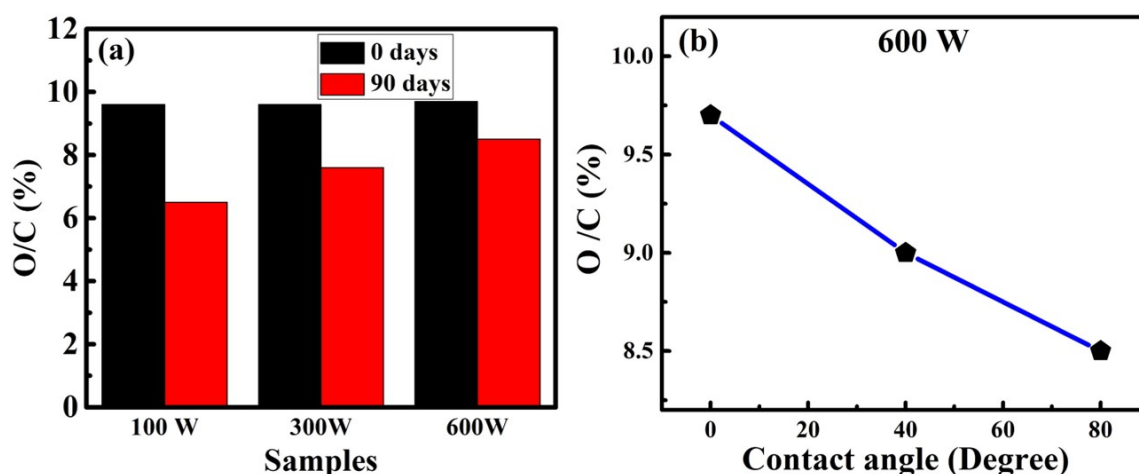


**Figure 4.19** – O/C percentage variation (a) for plasma-treated VGN after 90 days and (b) for 600 W at different WCA.

To further emphasize the correlation between surface chemistry with super-hydrophilic nature and its ageing in plasma-treated VGN surfaces, XPS analysis is carried out on the plasma-treated VGN surface at 600W with WCA 0° (0 days), WCA 80° (90 days) and an intermediate position with WCA of 40°.

The measured O/C values for the samples with WCA 0°, 40° and 80° are 9.7, 9 and 8.5 % respectively (figure 4.19(b)). The higher oxygen content in case of immediately after plasma exposure made the surface highly polar and resulted in super-hydrophilic with WCA nearly 0°. This confirms that a reduction in oxygen content happens on the plasma-treated VGN surfaces as the number of days passed, which indicates the desorption of oxygen from the VGN surface with time. It gives concrete evidence for the change in wetting nature with time.

### 4.4.3 Electrochemical capacitance study

Figure 4.20(a) illustrates the cyclic voltammogram (CV) of as-grown and 600 W plasma-treated VGN at different WCA such as  $0^\circ$ ,  $60^\circ$  and  $80^\circ$  at a scan rate of 0.1 V/s.

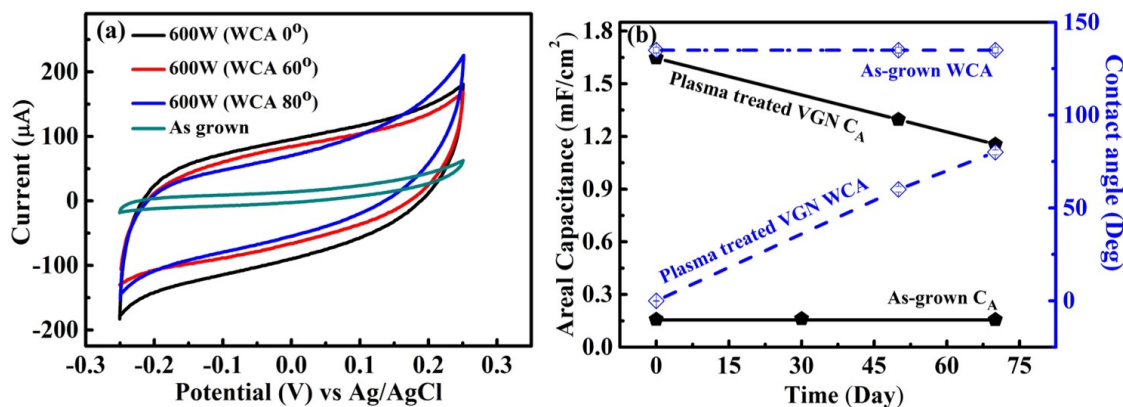


**Figure 4.20** – (a) CV of as-grown and 600 W plasma-treated VGN for WCA  $0^\circ$ ,  $60^\circ$  and  $80^\circ$  at 0.1 V/s scan rate (b) Change in areal capacitance and WCA with ageing time for as-grown and 600 W plasma-treated VGN.

A near rectangular CV for all samples confirms good supercapacitor performance. Figure 4.20(b) depicts the measured areal capacitance and WCA as a function of aging time. The plasma-treated VGN surface with WCA of near  $0^\circ$  exhibits a maximum areal capacitance of 1.7 mF/cm<sup>2</sup> and it is found to reduce with ageing due to increase in WCA. For the 90 days aged sample with stable WCA  $80^\circ$ , the measured capacitance value is 1.2 mF/cm<sup>2</sup>. In contrast, the hydrophobic as-grown VGN surface possesses an areal capacitance of about 0.15 mF/cm<sup>2</sup> through out the aging period. The findings are attributed to the reduction in the oxygen content, as confirmed from XPS results.

### 4.4.4 Discussion

Based on the investigations mentioned above, a plausible mechanism is established to explain the change in wetting nature, as described by the schematic image shown in figures 4.21(a) and (b).

The hydrophobic nature of the as-grown VGN surface is due to the 3D interconnected

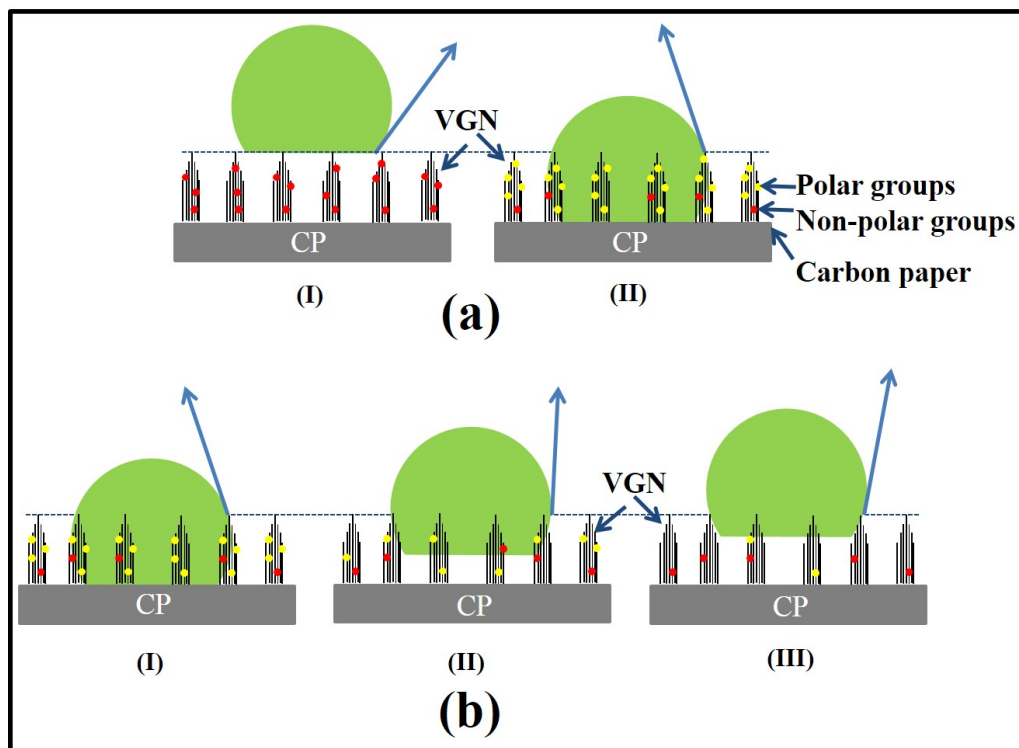


**Figure 4.21** – Structural models for change in WCA (a) before and after plasma treatment and (b) with ageing.

porous structure and the non-polar C-H bonding as illustrated in figure 4.21(a). Subsequently, after the oxygen plasma treatment, fresh dangling bonds are created due to chemical etching and it can also oxidize the C-H bonds and transform them into hydroxyl, epoxy and carbonyl (C-OH, O-C-O or C=O) groups, as shown in figure 4.21(b), that leads to hydrophilic nature. However, some of the oxygen groups are not chemically bonded to the surface, its desorption affects the wetting nature of VGN with ageing and hence not stable for longer time.

This study on atmospheric ageing of VGN electrodes shed light on the significant role of oxygen functional groups to enhance the longevity of hydrophilic nature in VGN structures. It also emphasizes the role of methodological optimization of the plasma-treatment parameters to achieve VGN electrodes with preferential oxygen functionalities for superior energy storage performance.

## 4.5 Symmetric supercapacitor fabrication and performance

A symmetric VGN electrode based coin-type device was fabricated by assembling two electrodes of 600 W *in-situ* plasma-treated VGN grown on carbon paper. The polyvinyl alcohol (PVA) and KOH based gel polymer electrolyte is used as the separator between them. The gel polymer electrolyte was prepared by the continuous stirring of 1 g PVA in 10 ml DI water at 80 °C till it completely dissolved and forms a homogeneous solution. Followed which 10 ml of 1M KOH was added drop by drop to the solution with continuous stirring and then cooled down to room temperature.

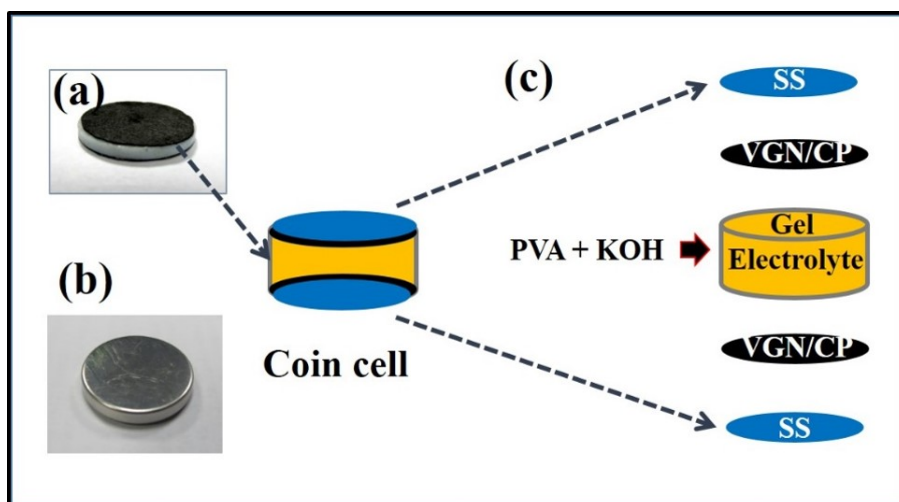


**Figure 4.22** – Schematic of the symmetric electrochemical capacitor device.

The photographs in figure 4.22(a) and (b) depict the fabricated VGN based coin-type device before and after sealing, respectively. The pictorial representation of the coin-type device assembly is illustrated in figure 4.22(c).

The electrochemical investigation of fabricated symmetric electrochemical capacitor device from 600 W *in-situ* plasma-treated VGN is carried out in a two-electrode configuration. A solid gel electrolyte served as the separator-cum-electrolyte reservoir between

the two symmetric electrodes. The CV profile of the device, as shown in figure 4.23(a), exhibits a stable potential window of 0.8 V and a nearly rectangular shape profile.

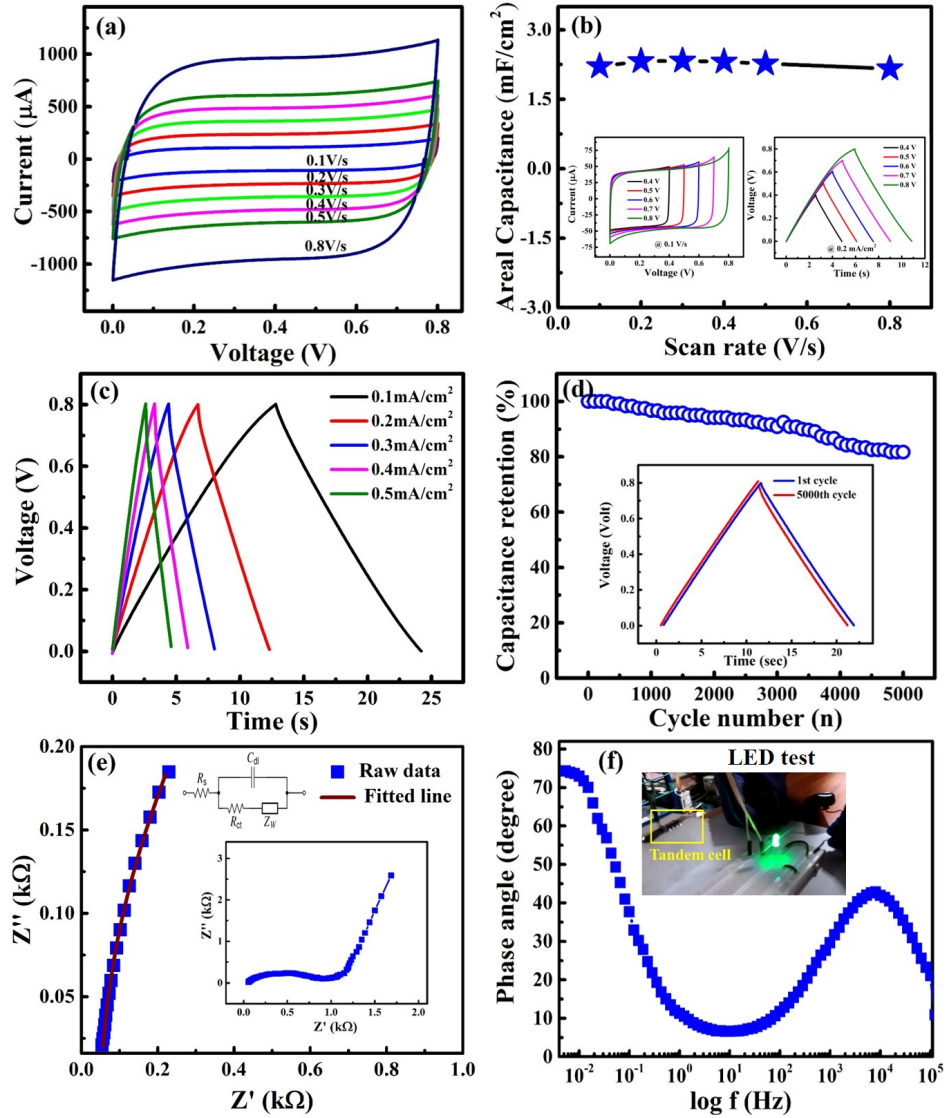


**Figure 4.23** – (a) CV of coin-type device at different scan rates, (b) change in areal capacitance with scan rate, inset shows the CV and CD at different potential window, (c) CD at different current densities and (d) capacitance retention for 5000 cycles at 0.1 mA/cm<sup>2</sup>, inset shows the CD curve comparison for 1<sup>st</sup> and 5000<sup>th</sup> cycle. Impedance responses of coin-type device (e) Nyquist plot (inset shows the entire range of frequency and Randles circuit) and (f) Bode plot, inset shows the discharge of the device through LED.

The areal capacitance of the symmetric coin-type device is calculated from the CV using the equation as follows,

$$C_{cell} = \frac{\int idV}{\Delta V \times A \times s} \quad (4.5)$$

where,  $\int idV$  represents area under the curve,  $\Delta V$  is the potential window,  $s$  is the scan rate and  $A$  is the total area of the two-electrode exposed to electrolyte ( $2.26 \text{ cm}^2$ ). The radius of the electrode was 0.6 cm.

The device offers a capacitance value of  $2 \text{ mF/cm}^2$  at a scan rate of  $0.1 \text{ V/s}$ . The device's calculated energy density and power density are  $0.17 \text{ }\mu\text{Wh/cm}^2$  and  $60 \text{ }\mu\text{W/cm}^2$ , respectively. An excellent charge storage stability is observed with respect to the scan rate (figure 4.23(b)).

Figure 4.23(c) shows the CD profile of the electrochemical capacitor device. The linear CD profile reveals the good capacitive characteristic of the device. The CV and CD of the symmetric device are carried out at different potential windows for  $0.1 \text{ V/s}$  scan rate and  $0.2 \text{ mA/cm}^2$  current density, respectively (insets of figure 4.23(b)). Both the CV and CD are consistent for  $0.4\text{-}0.8 \text{ V}$  potential window. An excellent cycle stability with capacitance retention of 80% is observed for 5000 charge-discharge cycles (figure 4.23(d)). Inset in figure 4.23(d) shows the comparison of CD curve for 1st and 5000<sup>th</sup> cycle.

Figure 4.23(e) and (f) shows the Nyquist plot and Bode plot of the symmetric device over the frequency range of  $100 \text{ kHz}$  to  $0.01 \text{ Hz}$ , respectively. The impedance is presented from high to low (from left to right) frequency in the Nyquist plot (inset figure 4.23(e)). The intercept with  $x$ -axis gives the equivalent series resistance which is  $0.055 \text{ k}\Omega$  (figure 4.23(e)). At low frequency, a nearly vertical Nyquist plot is observed, which indicates good supercapacitor behavior. From the Bode plot (figure 4.23(f)), the phase angle of the device is measured to be  $74.5^\circ$  at low frequency. At the phase angle of  $45^\circ$ , a drastic change in the frequency represents the lower Warburg element ( $Z_w$ ), owing to the large and accessible surface area [167].

The LED test is carried out on the tandem cell prepared by connecting the symmetric devices in series to check the device's practicability. The cell is charged up to  $4 \text{ V}$  and

discharged through an LED. Inset in figure 4.23(f) shows the illumination of LED.

## 4.6 Conclusion

Transformation of the intrinsic hydrophobic nature of vertical graphene nanosheets (VGN) into super-hydrophilic is achieved while preserving its advantageous 3D interconnected structure by post oxygen plasma treatment. A detailed investigation of the surface chemistry by XPS, affirmed an increase in surface oxygen content in VGN structures after plasma exposure. This leads to the conversion of hydrophobic VGN surface to super-hydrophilic which enhanced the electrochemically active surface area. Besides, a preferential increase in C-O bonding (hydroxyl & carbonyl) in plasma-treated VGN is observed at higher plasma power. Additionally, a significant variation in concentration of oxygenated functional groups is evident among *ex-situ* & *in-situ* plasma-treated samples. Interestingly, the super-hydrophilic VGN surfaces exhibited a ten times enhancement in capacitance. The highest areal capacitance value observed is  $1.7 \text{ mF/cm}^2$  for 600 W *in-situ* VGN. *In-situ* plasma-treated VGN exhibited better capacitance than *ex-situ* treated, at all plasma powers. This is correlated with the higher concentration of unwanted carboxyl type oxygenated functional groups in *ex-situ* plasma-treated samples. Also, a comparative study confirms the oxygen plasma treatment is the most effective plasma treatment than other ( $\text{H}_2$  &  $\text{N}_2$ ) plasma treatment. However, the oxygenated functional groups' temporal instability with ageing is confirmed, which affects the hydrophilic nature. The rate of change in wetting is found to be influenced by the plasma power. Herein, a correlation between capacitance, wetting nature and oxygen functional groups is established. The charge storage capability of the plasma functionalized VGN electrodes is also demonstrated by fabricating a symmetric device and glowing a LED using it.

# Chapter 5

## Metal/metal oxide-VGN hybrid structures and their electrochemical capacitor performance

The most beautiful system of the sun, planets and comets, could only proceed from the counsel and dominion of an intelligent and powerful being.

-Isaac Newton

### 5.1 Introduction

Supercapacitors (SCs) are one of the emerging energy storage devices due to their superior power density and long cycle life [52, 53, 110, 168]. However, a lower energy density compared to conventional batteries has restricted their potential utilization. Supercapacitors are classified into two categories depending upon the charge storage mechanism, electric double-layer capacitor (EDLC) and pseudocapacitor [169]. The charge storage in the case of EDLC relies on the electric double layer (EDL) formation at the electrode/electrolyte interface [145, 147]. Whereas Faradic redox reactions are responsible for the pseudocapacitance [52]. Although pseudocapacitor materials like transition metal oxides, hydroxides, nitrides and conducting polymers give a higher charge storage capacity, the carbon materials have drawn more attention due to their high power density, excellent electrical conductivity and good electrochemical stability [145, 146]. Amongst the carbon family,

vertical graphene nanosheets (VGN) garnered a lot of attention as an efficient SC electrode material, due to its large accessible surface area, non-agglomerated structure and 3-D porous geometry and high in-plane electrical conductivity [23, 119, 155].

The VGN has a theoretical charge storage capacity of around  $1.5 \times 10^4$  F/cm<sup>2</sup> [18]. Whereas, the reported SC values for graphene derivatives are found to be in the range of micro to milli F/cm<sup>2</sup> [86, 93, 156, 170]. Hence, an improvement in the charge storage capacity of graphene structures has attracted a lot of attention in recent times. Numerous methods, like changing wettability [92–94], functionalization by nitrogen and oxygen [95, 96], decoration of transition metal oxide/hydroxides [171, 172], use of organic/ionic electrolyte [97, 98] or designing symmetric/asymmetric SC [99] were tried to enhance the capacitance performance of carbon nanostructures. Amidst, hybrid graphene structures decorated with transition metal nanoparticles (NPs) exhibited significant improvement in specific capacitance [100, 101]. It is expected that a VGN with a homogeneous decoration of metal NPs will further improve its conductivity and facilitate an easy ion insertion/extraction into the structure. Also, the charge transfer due to the adsorption of metals on graphene as well as the electrochemical performance of the metal NP decorated carbon nanostructures are reported independently [103, 104]. Thus, the focus of this chapter is on engineering the electrode materials with transition metal/metal oxide NPs to achieve a superior charge storage performance and to understand the effect of charge transfer at the graphene/metal interface on the capacitance.

This chapter is focused on the influence of the transition metal NPs (Au, Ag, Cu and Ni) decoration of a VGN structure on its capacitance performance. The energy storage performance is correlated with the charge transfer that occurs due to the mismatch in the work function. The Ni decorated VGN exhibited highest charge transfer (+ 0.48  $e$ ) and capacitance (3.04 mF/cm<sup>2</sup>). Further, NiO and TiO<sub>2</sub> NP decoration to VGN is also carried out and the capacitance performance is discussed.

## 5.2 Metal-VGN hybrid electrodes and the effect of charge transfer on electrochemical capacitance

VGN were synthesized on SiO<sub>2</sub>/Si and carbon paper (CP), using microwave plasma-enhanced chemical vapor deposition. The detailed synthesis procedure is described in **chapter-3**.

After the VGN synthesis, a variety of metal NPs, namely Au, Ag, Cu, and Ni, were deposited onto the VGN surface using a thermal evaporation technique (12A4D, HIND-HIVAC, India). The rate of deposition for all these metals was controlled using a quartz crystal thickness monitor and the areal distribution of NPs depends on their evaporation rates. The deposition rate (0.1 Å/s) and mass loading were maintained the same for all the metal decorations.

### 5.2.1 Morphological analysis

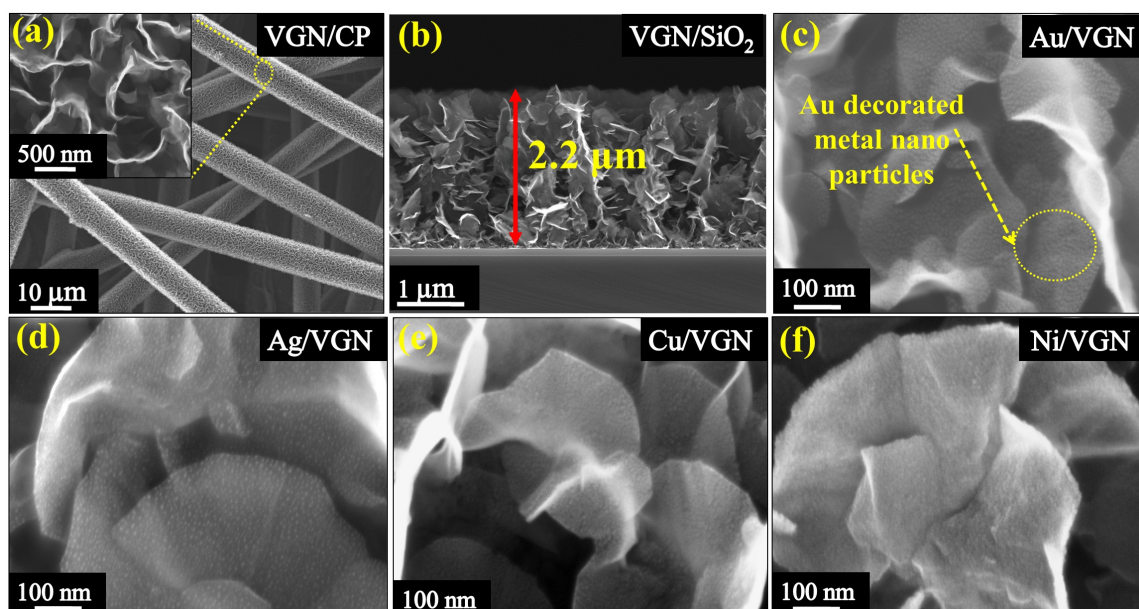


**Figure 5.1** – FESEM micrographs of (a) as-grown VGN on CP (VGN/CP) and inset shows magnified image and (b) a cross-sectional image of as-grown VGN. Magnified micrographs of the metal nanoparticle (c) Au, (d) Ag, (e) Cu and (f) Ni decorated VGN/CP.

Figure 5.1(a) illustrates the morphology of the as-grown VGN on fibers of the CP substrate. The magnified micrograph in the inset shows an interconnected network-like structure of VGN. The cross-sectional image of FESEM in figure 5.1(b) confirms the vertical orientation with a sheet height of about  $2 \mu\text{m}$ . Additionally, figures 5.1(c-f) depict high-resolution FESEM micrographs showing the uniform distribution of metal NPs of size 5-10 nm on the VGN structures. It is clearly evident that the morphology and structure of the VGN are preserved after NP decoration.

### 5.2.2 Structural analysis

Figure 5.2(a) illustrates the Raman spectrum of VGN consists  $D''$ , D, G,  $D'$ ,  $D+D''$ ,  $G'$ ,  $D+D'$  and  $2D'$  peaks [137]. The D ( $1355 \text{ cm}^{-1}$ ), G ( $1583 \text{ cm}^{-1}$ ), and  $G'$  ( $2707 \text{ cm}^{-1}$ ) are characteristic peaks of VGN [137, 156] and their presence confirm graphitic nature of the structure [136, 137]. Whereas, the presence of the  $D''$  ( $1100 \text{ cm}^{-1}$ ),  $D'$  ( $1621 \text{ cm}^{-1}$ ),  $D+D''$  ( $2455 \text{ cm}^{-1}$ ),  $D+D'$  ( $2950 \text{ cm}^{-1}$ ) and  $2D'$  ( $3245 \text{ cm}^{-1}$ ) bands confirm the highly defective nature of VGN [136, 173]. The reason behind the origin of different peaks are discussed in **chapter-3** section 3.3.

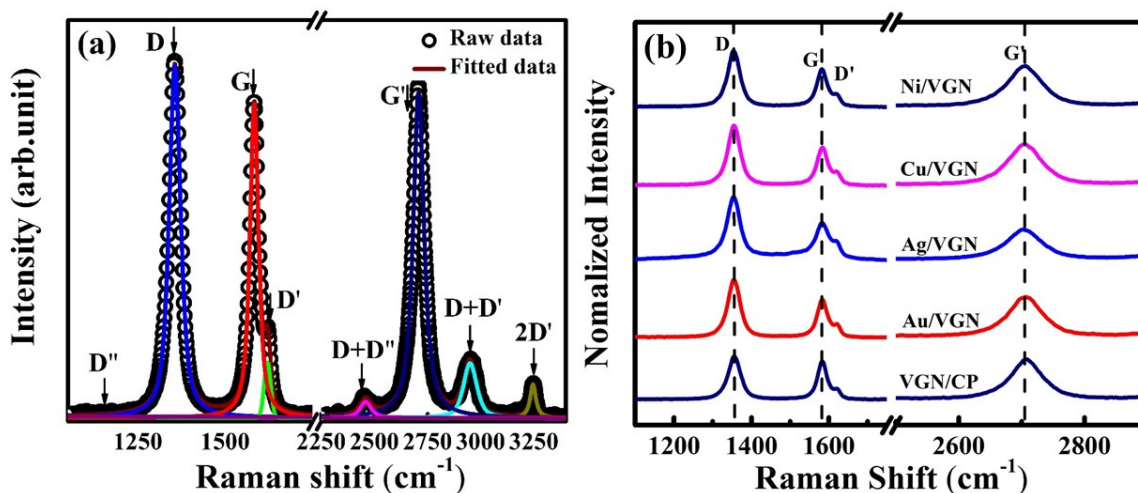


**Figure 5.2** – (a) Raman spectrum of as-grown VGN with deconvoluted peaks and (b) Raman spectra of as-grown and metal-decorated VGN.

The shape and features of the Raman spectra are retained after different metal NP

decoration, which confirms the structural stability of VGN after the decoration. There is no change in the peak position and structure of the spectra for different metal-decorated VGN is evident from figure 5.2(b).

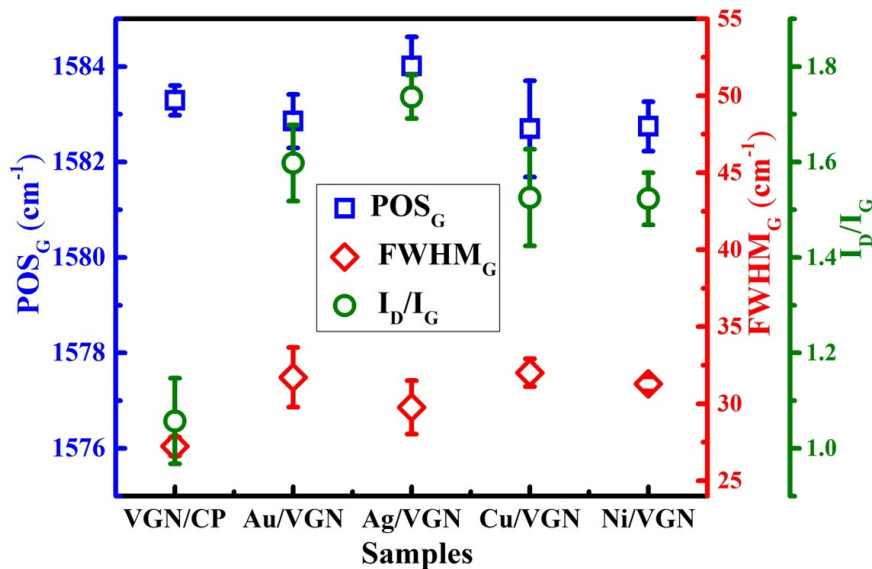


**Figure 5.3** – Variations in the  $POS_G$ ,  $FWHM_G$  and  $I_D/I_G$  values of as-grown VGN and different metal-decorated VGN.

Furthermore, the Raman spectra are deconvoluted and the extracted parameters are plotted in figure 5.3. The key parameters are the intensity ratio of D-to-G peaks ( $I_D/I_G$ ), the position and the full width at half maximum (FWHM) of G-peak. A shift in the G-peak position ( $POS_G$ ) indicates strain (compressive or tensile) introduced in the structure [75]. Whereas, the FWHM and  $I_D/I_G$  ratio measure crystallinity and defect density, respectively and the crystalline size is inversely proportional to the FWHM of G and  $I_D/I_G$  ratio [174].

There is no significant shift in the G peak position of VGN structures is observed after the metal NP decoration Figure 5.3. However, the different metal-decorated VGN resulted in a slight broadening of the G peak and an increase in the  $I_D/I_G$  ratio. Both confirm an increase in structural disorder or defects in the metal-decorated VGN, attributed to the alteration in local bonding upon interaction between the graphene structure and the

metal nanoparticle [175].

### 5.2.3 Surface chemistry analysis

Elemental and chemical composition of the as-grown and metal-decorated VGN are carried out by X-ray photoelectron spectroscopy (XPS).

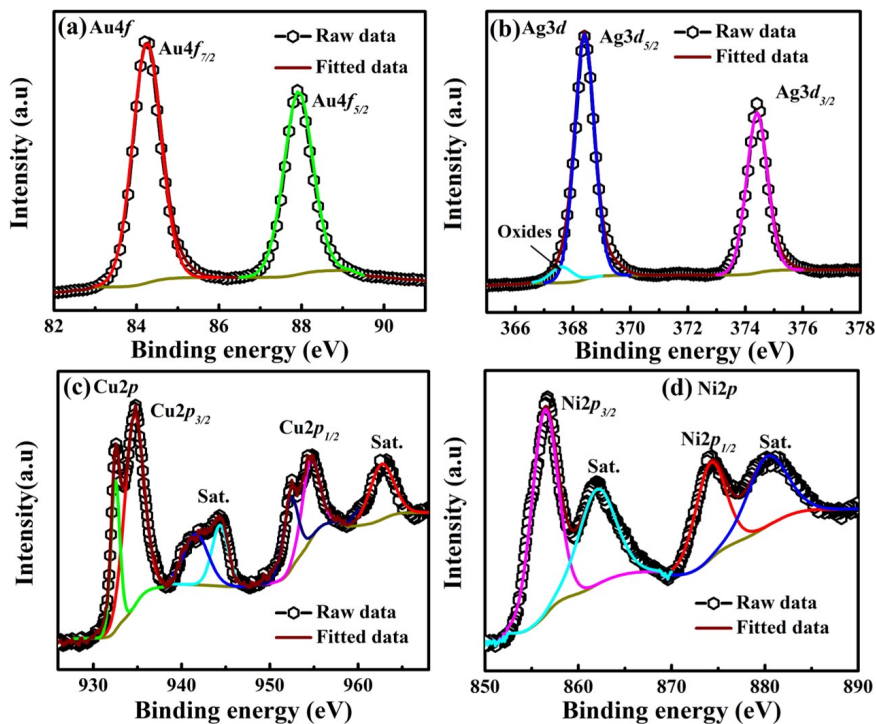


Figure 5.4 – XPS spectra of (a) Au4f, (b) Ag3d, (c) Cu2p and (d) Ni2p.

The survey and deconvoluted spectra (figures 5.4, 5.5 and 5.6) confirms the presence of peaks corresponding to C1s, O1s, Au4f, Ag3d, Cu2p and Ni2p at 284.9, 532.7, 84.2, 368.4, 934.6 and 856.4 eV, respectively [176]. A high oxygen percentage is observed in metal-decorated VGN and is attributed to the oxygen absorption by the reactive metal nanoparticles upon exposure to ambient conditions. However, there is no evidence of metal oxide formation from the low frequency region of Raman spectroscopy and XRD [176], which could be due to a lower metal concentration or amorphous oxide. Individual fitted metal peaks (Au, Ag, Cu, and Ni) shown in figure 5.4 confirm the metal decoration on VGN. The Au decorated VGN shows strong metal peaks and Ag displays less intense

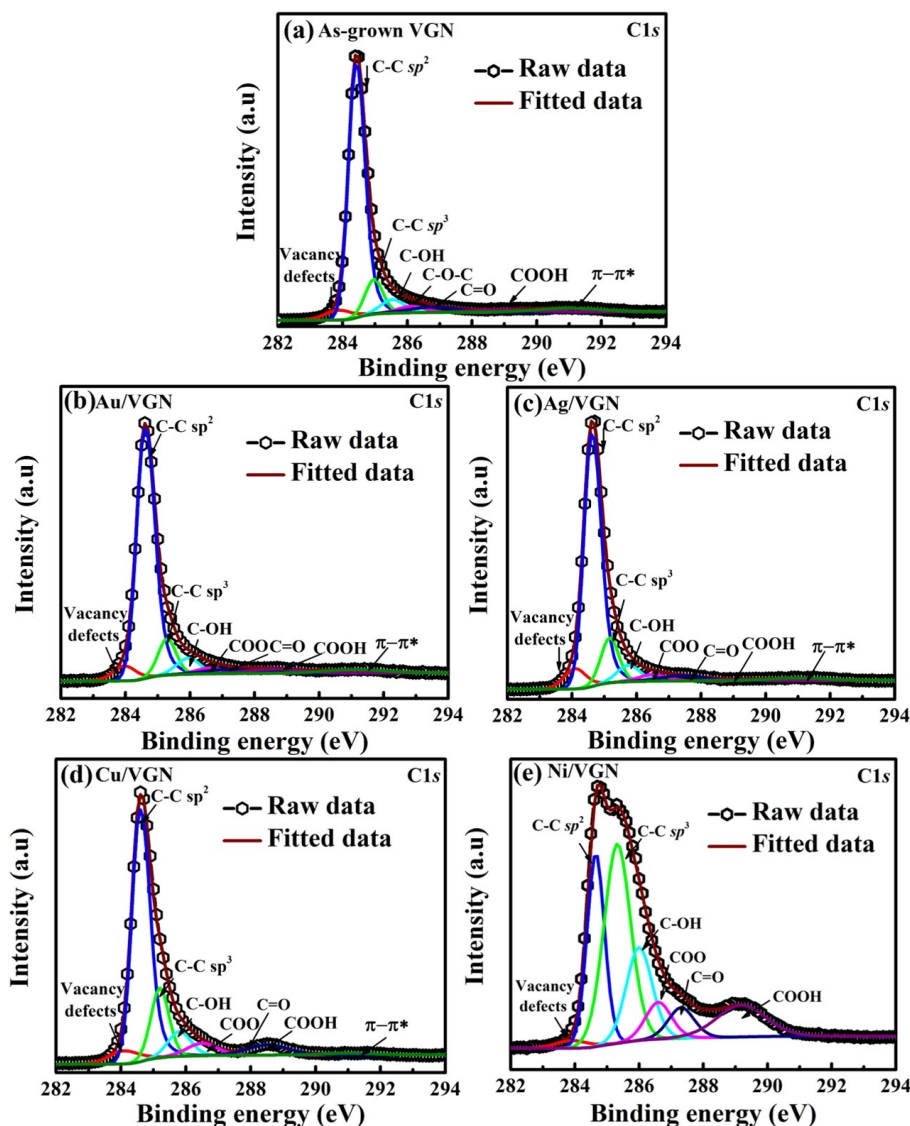


Figure 5.5 – XPS C1s spectra for as-grown and metal-decorated VGN.

oxide peak, indicating the presence of oxides. In the case of Cu and Ni peak,  $2p_{3/2}$  and  $2p_{1/2}$  peak position difference confirms the presence of oxides.

Figure 5.5 and 5.6 depict the high resolution C1s and O1s spectra respectively for as-grown and metal-decorated VGN. The deconvoluted C1s spectra of VGN consists of major peaks at 283.8, 284.4 and 285 eV corresponding to structural defects,  $sp^2$  C-C and  $sp^3$  C-C, respectively [138, 156]. Also, less intense peaks at 285.5, 286.1, 286.8 and 288.9 eV corresponding to oxygenated carbon bonds, such as hydroxyl group (C-OH), ether/epoxy group (C-O-C), carbonyl group (C=O) and carboxyl group (COOH),

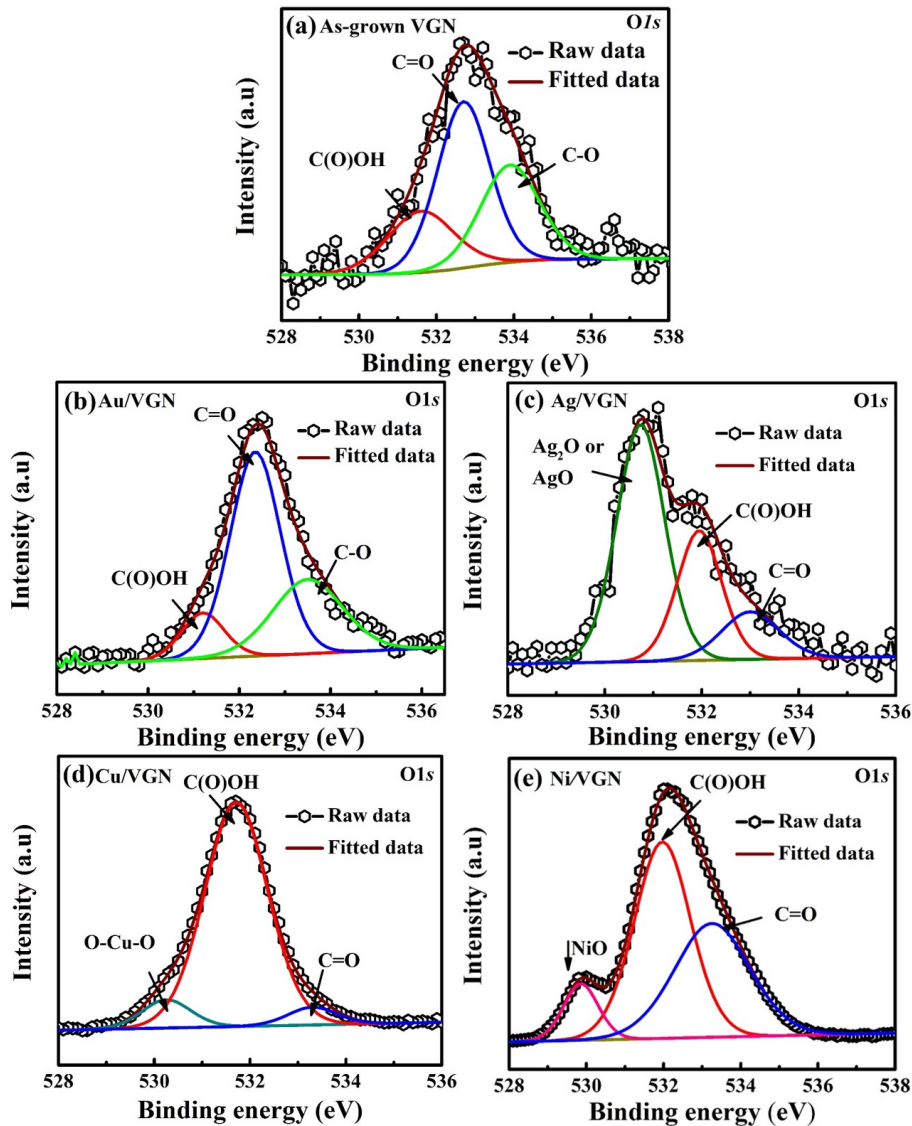
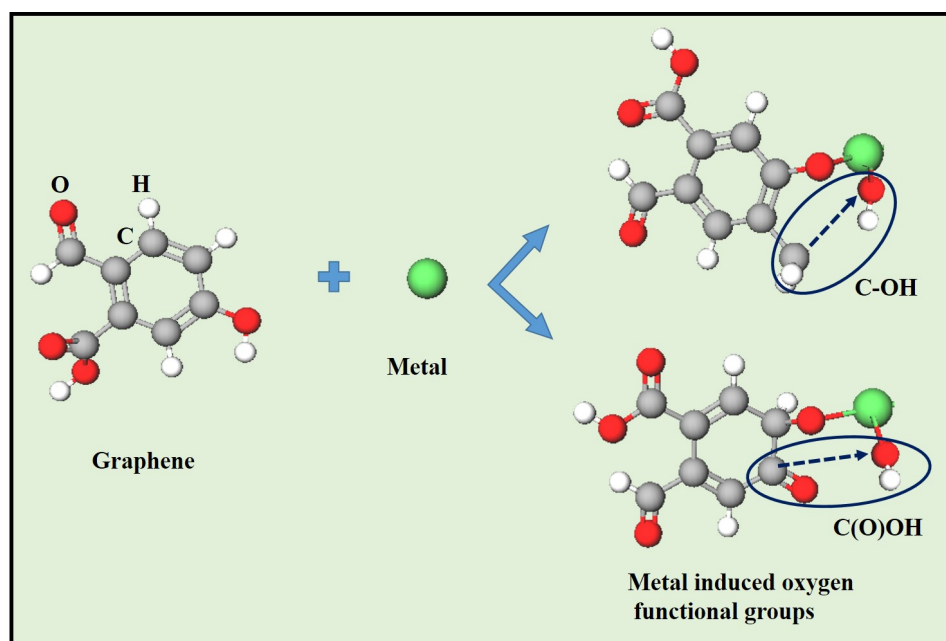


Figure 5.6 – XPS O1s spectra for as-grown and metal-decorated VGN.

respectively was observed [79, 139]. These oxygenated functional groups can serve as bridges for the heteroatoms. The presence of  $\pi$ - $\pi^*$  transition at *ca.* 291 eV, originating from the conjugated delocalized electrons, indicates graphitic carbon contribution [177]. The C1s spectrum of metal-decorated VGN shows an increase in  $sp^3$  concentration and is higher in the Ni decorated VGN, i.e 35 %. Figure 5.6 shows the deconvoluted O1s spectrum of Ni-decorated VGN, which confirms the formation of oxides in the case of the Ag, Cu and Ni decorated VGN. The oxide in case of the Ni/VGN corresponds to NiO (529.8 eV). Also figure 5.4 and 5.6 confirm the oxygen bonding between the metal

NPs and VGN [178–180]. Additionally, a change in the type of C-O bonding is observed with different metal NP decorations. The reason is that different metal NPs have different reactivities to the atmospheric oxygen, which leads to a variation in the adsorbed oxygen. Further, the pre-existing oxygen on the graphene surface provides reactive sites for the metal ions to get attached. Further, the adsorbed metal ions get linked to the carbon and influence the formation of functional groups upon oxygen adsorption from the atmosphere, as shown in the schematic figure 5.7 [181, 182]. Therefore, high reactive metals like Cu and Ni show enhancement in COOH (from 0.65% in case of Au and Ag to 13% in Cu/VGN) bonds and Ni/VGN shows an increase in C=O (from 1.5 to 12.4%) bonds.



**Figure 5.7** – A schematic diagram showing the metal-induced formation of oxygen functional groups.

#### 5.2.4 Electrical measurement

The metal NP decoration is expected to improve the electrical conductivity of graphene structures. Therefore, the sheet resistance of these samples is measured using the four-probe technique and calculated by the Van der Pauw method. The Ohmic behavior of the as-grown and metal NP-decorated VGN structures is observed from the linear current-

voltage relationship of the I-V measurements. The as-grown VGN exhibited a sheet resistance of around  $677 \Omega/\square$ , and was found to reduce after NP decoration. The obtained sheet resistance values for Ag/VGN, Cu/VGN, Au/VGN and Ni/VGN are 257, 160, 139 and  $122 \Omega/\square$ , respectively. Therefore, the improvement in the electrical conductivity of VGN after metal NP decoration is evident.

The metal decoration of VGN induces a charge transfer and, in-turn influences the sheet resistance. It has been reported that the adsorption of metal NPs onto graphene significantly affects its electronic properties. Because of the short-range interaction between graphene and metal NPs, a shift in the graphene's Fermi level occurs. To equilibrate the Fermi level, charge transfer takes place between the graphene and metal NPs. It is reported that the weakly bonding metals like Cu, Ag and Au, preserves the electronic structure of the graphene and strongly interacting metals like Co and Ni, etc., form a covalent bond with the graphene and alters its electronic structure significantly.

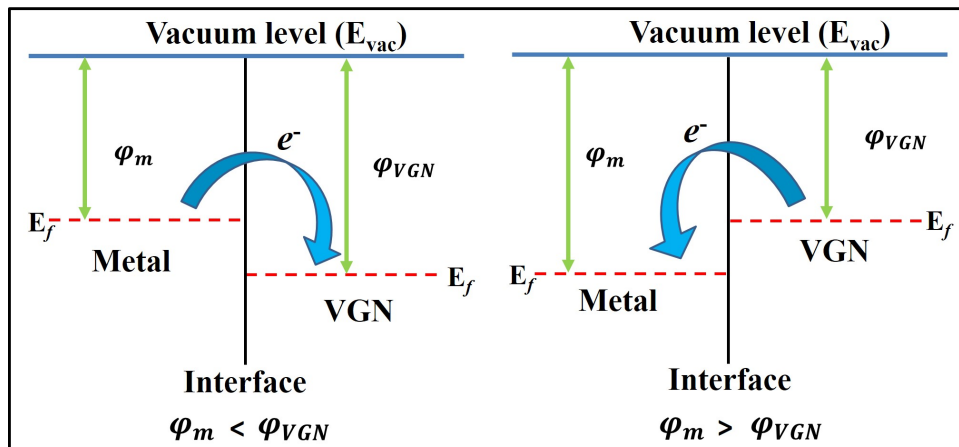


**Figure 5.8** – A schematic diagram of work function dependent charge ( $e^-$ ) transfer at the VGN and metal NP interface.

Furthermore, charge transfers between the graphene sheet and metal NPs is due to the mis-match in their work function ( $\varphi$ ), with the transfer of electrons from metal NP to VGN when  $\varphi_m < \varphi_{VGN}$  and from VGN to metal NP when  $\varphi_m > \varphi_{VGN}$ . Here,  $\varphi_m$  is the work function of the metal NP and  $\varphi_{VGN}$  is the VGN work function. In both cases,

carrier density at the surface increases and reduces the resistance for charge locomotion. Further, it helps in drawing more ions to the electrode-electrolyte interface to form an electric double layer. Figure 5.8 illustrates a schematic of charge ( $e^-$ ) transfer process that occurs at the interface of the metal NP and VGN surface. Where,  $E_f$  is the Fermi energy level. The table 5.1 shows the difference in the work function values for VGN and metal/metal oxide from the literature.

Material	Work function (eV) from the literature	Reference
VGN	4.6-5.2	[183, 184]
Au	5.1-5.5	[185]
Ag, Ag oxide	4.3-4.8	[102]
Cu, Cu oxide	4.5-5.1	[186, 187]
Ni, Ni oxide	4.8-5.6	[187, 188]

**Table 5.1** – Work functions for VGN, metal and metal oxides from the literature.

### 5.2.5 Electrochemical capacitance study

Electrochemical capacitance studies are carried out for as-grown and metal-decorated VGN in a three-electrode electrochemical cell set-up. The cyclic voltammogram (CV) and charging-discharging (CD) of as-grown VGN are discussed in the previous chapter. A nearly rectangular CV and a triangular CD profile of the as-grown VGN affirms good capacitor behaviour. Comparative CVs of as-grown and NP decorated VGN are shown in figure 5.9(a). A significant increase in area under the CV curve confirms an enhancement in charge storage performance of VGN with NP decoration. The areal capacitance of these samples is calculated using the following equation:

$$C_A = \frac{\int idV}{\Delta V \times A \times s} \quad (5.1)$$

Where  $\int idV$  is the area under CV,  $s$  is the scan rate of CV,  $\Delta V$  is the potential window and  $A$  is the exposed area of working electrode in the electrolyte. The calculated capac-

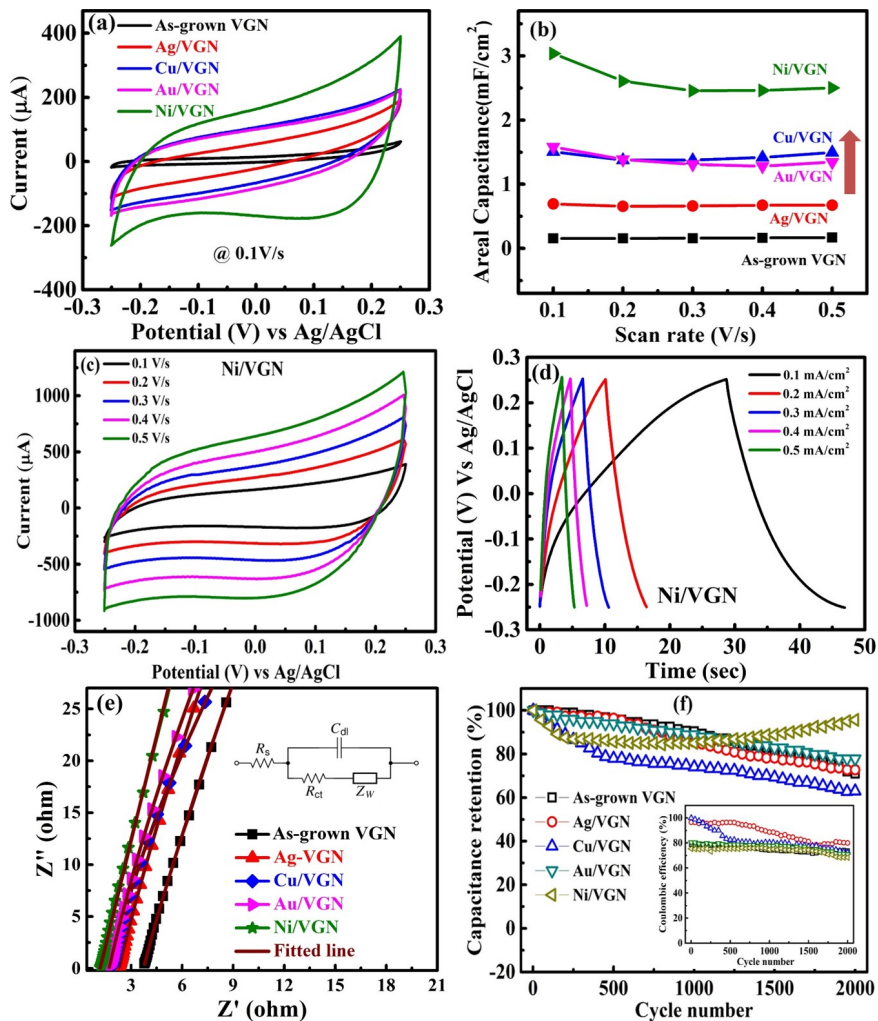


**Figure 5.9** – (a) A comparison of CVs for as-grown and different NP-decorated VGN, (b) plots of areal capacitance *vs.* scan rate of as-grown and metal NP-decorated VGN, (c) CVs and, (d) CD data of Ni/VGN, (e) impedance spectra for as-grown and metal-decorated VGN (the inset shows the fitted equivalent circuit), and (f) capacitance retention and coulombic efficiency (inset) for as-grown and metal-decorated VGN.

itance values for as-grown, Ag/VGN, Cu/VGN, Au/VGN and Ni/VGN at 0.1 V/s are 0.16, 0.62, 1.47, 1.58 and 3.04 mF/cm<sup>2</sup> (121.6 F/g), respectively.

A significant enhancement in capacitance with metal NP decoration is evident, which also corroborated with the electrical conductivity results. Although Au has more electrical conductivity than Cu, both exhibited a similar range of capacitance. This could be attributed to the contribution of oxygen in the Cu/VGN, as evident from the XPS spectra. On the other hand, Ni NP decoration exhibited a nineteen-fold enhancement

in capacitance. Even though the electrical resistivity of Ni/VGN is slightly lower than that of Au and Cu/VGN, the capacitance enhancement is nearly double. This could be attributed to the presence of NiO as confirmed from XPS spectra. However, the enhanced capacitance value in this study is still less compared to the reported values due to the lower mass loading of metals. As our focus is to understand the charge transfer process in metal-decorated VGN structures, thus we limited the decoration to a lower mass loading to reduce the effect of pseudocapitance. Nevertheless, we found that the measured capacitance values are still higher than a few of the reported ones. A detailed comparison is provided in table 5.2.

Materials	Capacitance (C in F/g)	Capacitance measurement at	Electrolyte	Reference
NiO	80	10 mA/cm <sup>2</sup>	6M KOH	[189]
NiO Nanoparticle	97	0.1 A/g	1M KOH	[190]
NiO nanosheet	81.6	0.5 A/g	3M KOH	[191]
CNT/NiO nanoflower	120	10 mV/s	1M Na <sub>2</sub> SO <sub>4</sub>	[192]
VGN/NiO nanoparticle	121.6	100 mV/s	1M KOH	This work
Graphene/Ni nanocomposite	144	10 A/g	1M KOH	[193]

**Table 5.2** – Electrochemical capacitance comparison of NiO and carbon nanostructure/NiO hybrid electrodes.

The CV measurements are carried out in a potential window from -0.25 V to 0.25 V to evaluate the effect of charge transfer on the capacitance. Additionally, the CV measurements in the extended window, also carried out for Cu and Ni/VGN to find out the existence of redox peaks, which evident no sign of strong redox peaks [176]. Furthermore, the CV curves are not perfectly rectangular, which also affirms the presence of pseudocapitance. The enhanced capacitance of VGN after NP decoration is attributed to the enhanced electrical conductivity of the composite and kinetically limited pseudocapaci-

tance due to the absorbed oxygen. The areal capacitance values of all the samples at different scan rates are shown in figure 5.9(b). As-grown VGN offers a constant capacitance value for different scan rates and there is a trivial decrease in capacitance value with scan rate for metal-decorated NPs due to the electrolyte's inaccessibility at higher scan rates. The CV and CD profiles for the Ni/VGN are shown in figure 5.9(c) and (d) and they affirm the ideal SC behavior. The CV and CD profiles of other metal decorated VGN also showed a similar behavior [176].

Electrochemical impedance spectroscopy (EIS) is carried out to bring out insights on the ion-movement and interactions at the electrode-electrolyte interface. Figure 5.9(e) depicts the impedance response of as-grown and metal-decorated VGN. The  $Z'$  intercept in the Nyquist plot is a measure of equivalent series resistance (ESR). Therefore, the impedance spectra were fitted with an equivalent circuit model, as shown in the inset of figure 5.9(e). The equivalent series resistance values obtained from the fitting are 3.5, 2.2, 1.8, 1.7 and 1.1  $\Omega$  for as-grown, Ag, Cu, Au and Ni NP-decorated VGN, respectively. A reduction in the ESR after the metal NP decoration is evident and the lowest value is observed for Ni nanoparticle decorated VGN, which affirms its lower resistance for ion movement.

The capacitance retention (CR) and Coulombic efficiency ( $\eta$ ) was obtained from the CD profile using the following equations:

$$CR = \frac{t_{d_n}}{t_{d_1}} \times 100 \quad (5.2)$$

$$\eta = \frac{t_d}{t_c} \times 100 \quad (5.3)$$

where,  $t_d$  and  $t_c$  is the charging and discharging time respectively,  $t_{d_n}$  is the discharging time for  $n^{th}$  cycle ( $n= 1.....n$ ) and  $t_{d_1}$  is the discharging time for 1<sup>st</sup> cycle.

The coulombic efficiency was found to be in the range of 80% (inset of figure 5.9(f)). Also,

the cycle life of the electrode material is one of the key factors for SC applications. Figure 5.9(f) shows the capacitance retention values of all the samples with respect to the CD cycle. An enhanced capacitance retention of 95% was found for Ni-decorated VGN, which is only 70% for the as-grown VGN. Interestingly, capacitance retention initially reduced and started to increase after 250 cycles for the Ni/VGN. This is due to the change in the oxidation state and local chemical environment during the electrochemical process, which is confirmed from the XPS analysis of the VGN electrodes after the electrochemical testing [176].

### 5.2.6 Computational analysis of charge transfer

In order to get a qualitative idea on how charge transfer happens between the transition metal (TM) adatoms and graphene sheet, we performed spin-polarized *ab initio* DFT calculations using the Vienna *ab initio* simulation package (VASP) [194]. The projector augmented wave (PAW) pseudopotential is employed to improve the efficiency and accuracy of the calculations. The generalized gradient approximation (GGA) exchange-correlation functionals of Perdew-Burke-Ernzerhof (PBE) are used in this study. To truncate the size of the plane wave basis set, a kinetic energy cut-off of 500 eV was used. The partial occupancies near the Fermi levels were treated using Methfessel-Paxton smearing with a 0.1 eV width. Integration over the Brillouin zone was performed using a Monkhorst-Pack grid of  $3 \times 3 \times 1$  k points for a  $6 \times 6 \times 1$  super-cell of the TM/graphene systems. The effects of Van der Waals (vdW) correction to the *ab initio* total energy are analyzed using a method proposed by Tkatchenko et al. i.e., Tkatchenko-Scheffler self-consistent screening (TS-SCS) [195].

*Ab initio* calculations were performed to substantiate the charge transfer between TM adatoms and the graphene sheet to corroborate with improved electrical conductivity and the charge storage performance of metal-decorated VGN. Here we considered a simplified

model, in which a TM atom is adsorbed onto a graphene sheet. The adsorbed TM atom can be anchored at three different locations on the graphene sheet, such as hollow (H), bridge (B) and top (T) [196]. The preferred adsorption sites of each TM atom is identified by computing the adsorption energies ( $E_{ads}$ ) as,

$$E_{ads} = E_{TM-GR} - (E_{GR} + E_{TM}) \quad (5.4)$$

where  $E_{TM-GR}$ ,  $E_{GR}$  and  $E_{TM}$  are the energy of graphene with TM adatoms, a pristine graphene sheet and isolated TM atom, respectively. The adsorption energy ( $E_{ads}$ ) and equilibrium distance ( $d_{min}$ ) between the TM atom and graphene sheet with and without van der Waals (vdW) interactions are listed in table 5.3. The computed energies show that Ni prefers the H site, Cu sits on the B site and Ag and Au reside on the T site. The corresponding optimized geometries are shown in figure 5.10.

Ad atom	sites	$-E_{ads}$ (eV)	$-E_{ads}^{vdW}$ (eV)	$d_{TM-C}$ (Å)	$d_{TM-C}^{vdW}$ (Å)
Ni	H	1.432	1.738	2.117	2.112
	T	1.137	1.383	1.856	1.856
	B	1.218	1.477	1.939	1.939
Cu	H	0.178	0.438	2.391	2.372
	T	0.327	0.555	2.079	2.084
	B	0.334	0.572	2.167	2.167
Ag	H	0.091	0.354	4.268	3.835
	T	0.098	0.361	4.072	3.529
	B	0.096	0.360	3.972	3.591
Au	H	0.296	0.583	4.165	4.015
	T	0.308	0.591	4.128	3.807
	B	0.307	0.589	4.176	3.879

**Table 5.3** – Adsorption energy for different sites of metal decorated adatoms on graphene.

The nature of charge transfer is analyzed by computing the effective charges ( $Q_{eff}$ ) on adsorbed TM and bounded C atoms using Badar charge analysis. The Badar charges ( $Q_{Badar}$ ) on each atom are computed using the scheme of Tang *et al.*, [197] and the

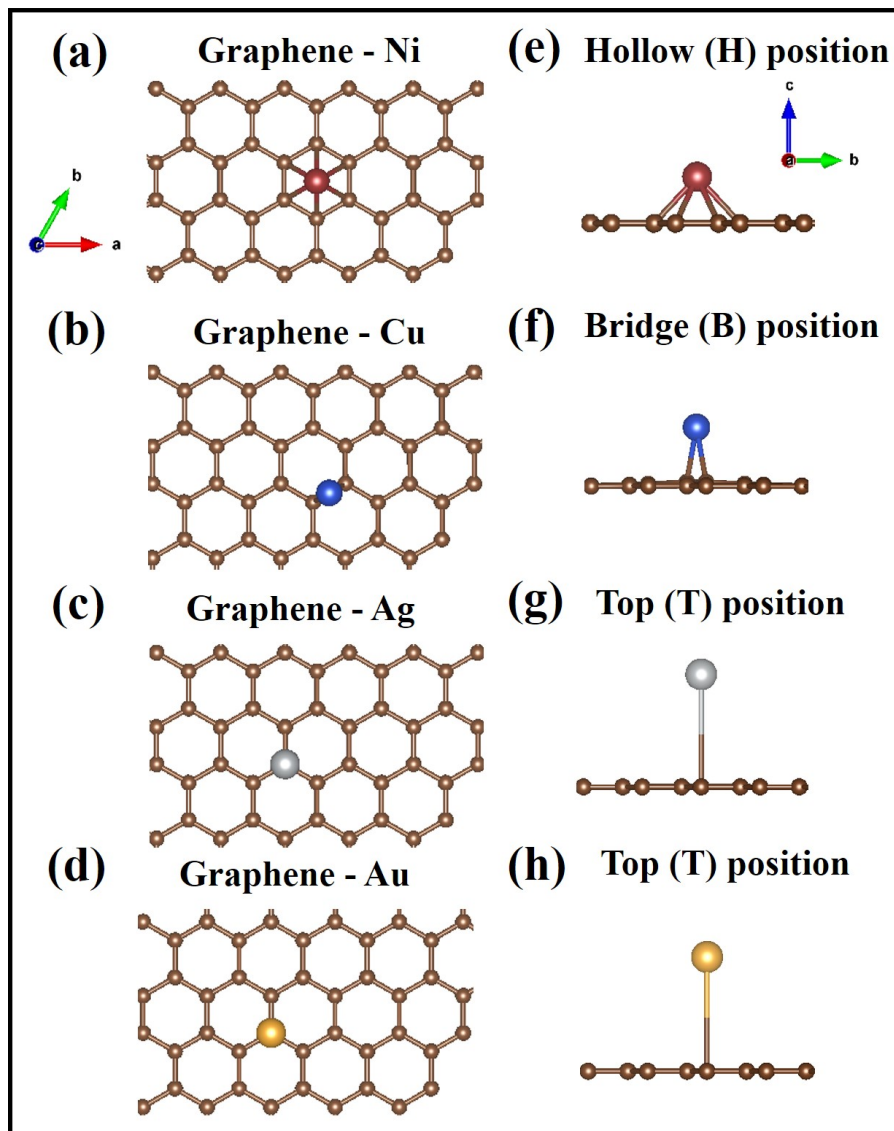


**Figure 5.10** – The optimized geometries of TM particles adsorbed on a graphene sheet ( $6 \times 6 \times 1$  super-cell): top view (a-d) and side view (e-h).

effective charges are computed as follows,

$$Q_{eff} = Z_{val} - Q_{Badar} \quad (5.5)$$

where  $Z_{val}$  is the number of valence electrons on each atom. The  $Q_{eff}$  in terms of electronic charge  $e$  is shown in table 5.4.

The positive sign of the effective charge on the carbon atom ( $Q_{eff}(C)$ ) represents the

Ad atom	$Q_{eff}$ (TM) units of $e$	$Q_{eff}^{vdW}$ (TM) in units of $e$	$Q_{eff}$ (C) in units of $e$	$Q_{eff}^{vdW}$ (C) in units of $e$
Ni	+0.488	+0.495	-0.531	-0.528
Cu	+0.219	+0.216	-0.521	-0.521
Ag	+0.060	+0.046	-0.233	-0.245
Au	-0.314	-0.313	+0.299	+0.299

**Table 5.4** – Effective charges on the transition metal and carbon atoms.

charge transfer from graphene to the metal atom and a negative sign is for the charge transfer from the metal atom to graphene and is also the same for a charge on metal atom ( $Q_{eff}$  (TM)). From table 5.4 it is evident that the Ni, Cu and Ag atoms give charge ( $e^-$ ) to graphene; in contrast, Au acquires charge from the graphene sheet. The direction of charge transfer (either metal to graphene or graphene to metal) is determined by the difference in the Fermi energy  $\Delta E_f(d)$ . Khomyakov *et al.*, [198] reported a model to explain the Fermi level shift and nature of the charge transfer. The parameters that depend on the direction of charge-transfer are the equilibrium distance ( $d_{eq}$ ) between graphene, the adatom atom and the work function of the metal atom. It is evident from table 5.3 that the computed equilibrium separation is high for Au and also Au has a high work function. Thus, Au atom's adsorption on graphene results in a positive shift in the Fermi level. Hence, the Au atom gains charge ( $e^-$ ) from graphene and acts as a  $p$ -type dopant [198]. Although the equilibrium separation between the Ag atom and graphene is high, it has a lower work function and hence it acts as an  $n$ -type dopant. Conversely, Cu has a high work function, but low equilibrium separation. Whereas, for Ni adatoms both the equilibrium separation and work function are low. Hence, all three, Ag, Cu and Ni, are found to donate charge ( $e^-$ ) to graphene and acts as  $n$ -type dopants. So, adsorption of both  $p$ -type and  $n$ -type dopants on to graphene results in charge transfer at the interface.

### 5.2.7 Discussion

The Ni adatoms acquired a higher effective charge (+0.488) that is also more than twice that of Cu and nearly eight times that of Ag adatoms (table 5.4). It is reported by Rego *et al.*, [196] that Ni with a  $d$  orbital occupancy upon adsorption onto graphene, induces the transfer of charge twice that of Pd or Pt with higher  $d$  orbital occupancies. In this study also, Ni, with lower  $d$  orbital occupancy than that of the Cu, Au and Ag induces a higher charge transfer and thus a higher specific capacitance. The above results validate the proposed charge transfer process driven by the mismatch in work function among metal NPs. From the XPS results depicted in figures 5.4, 5.5 and 5.6, it is confirmed that all the samples possess metal-oxygen-carbon bonding. This oxygen bridge between the metal NPs and graphene creates a considerable electron charge overlap and further acts as an effective pathway for the charge transfer. Finally, the enhancement in the total capacitance of the hybrid (metal NPs/VGN) electrode is the combined effect of charge transfer and pseudocapacitance (figure 5.11).

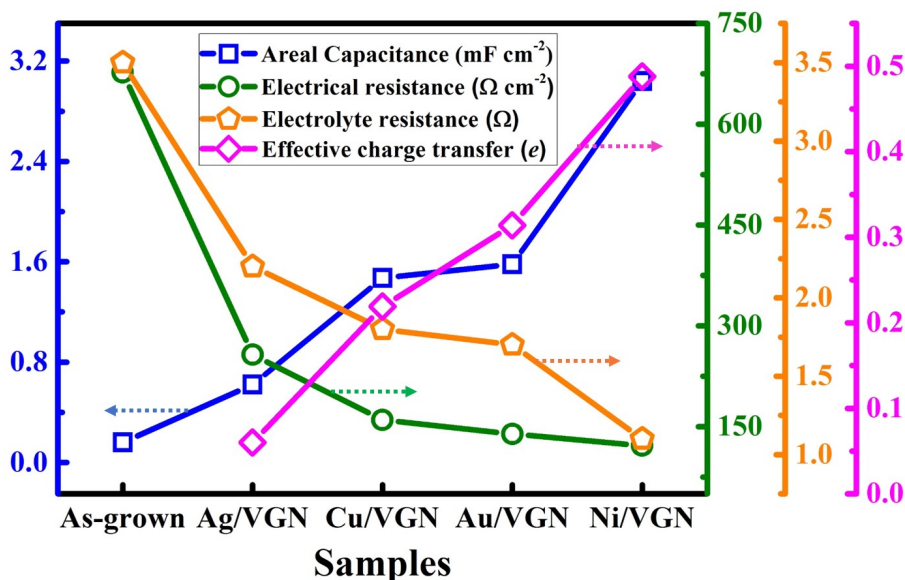


Figure 5.11 – Variation of capacitance and the different factors affecting the capacitance.

From the above discussion, the electrochemical performance of the hybrid structures can

be attributed to (i) the uniform and homogeneous distribution of NPs on VGN with the preserved morphology of VGN, (ii) a significant increase in the electrical conductivity of VGN after metal NP decoration which is attributed to the charge ( $e^-$ ) transfer between the metal NPs and graphene network at the interface due to the mis-match in work function, thus increasing the carrier density at the electrode surface leading to the high charge accumulation and (iii) catalytic effect of the metal NPs for the formation of metal-oxygen-carbon bonding which helps in the surface redox reaction.

### **5.3 Metal oxide-VGN hybrid structure and the electrochemical capacitance**

The previous discussions, confirmed that the Ni decorated VGN hybrid structure provides high capacitance value with the better electrochemical properties. Hence, the metal oxide NP decoration is carried out in a sputtering deposition system to investigate the effects further.

Towards that, NiO deposition was carried out by using a Ni target in a rough vacuum of nearly  $1 \times 10^{-1}$  mbar. The deposition was carried out at 70 V potential and deposition time is varied like 30 sec, 2 min, 5 min and 10 min. The samples are named as NiO<sub>30s</sub>/VGN, NiO<sub>2m</sub>/VGN, NiO<sub>5m</sub>/VGN and NiO<sub>10m</sub>/VGN, respectively. Similarly, TiO<sub>2</sub> is also decorated on VGN and the capacitance performance is investigated.

#### **5.3.1 Morphological analysis**

Morphology of as-grown and NiO decorated VGN (NiO/VGN) are illustrated in figure 5.12, where figure 5.12(a) consists the cross-sectional view of the as-grown VGN as an inset. From FESEM morphology, the retention of 3D interconnected structure with vertical orientations is evident, which acts as a reservoir for electrolyte and facilitates the

electrolyte ions to interact with the entire surface of VGN. Further, figure 5.12 (b-e) illustrate the morphology of different NiO/VGN.

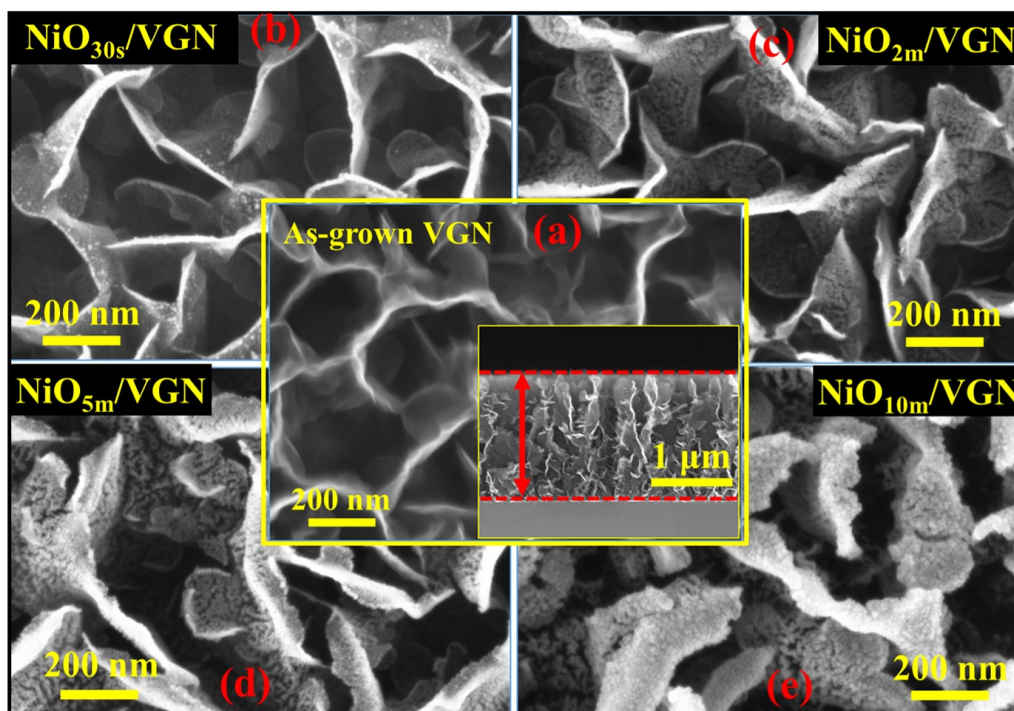


**Figure 5.12** – FESEM micrograph of as-grown and NiO decorated VGN; (a) as-grown VGN with cross-sectional image in the inset (b) NiO<sub>30s</sub>/VGN (c) NiO<sub>2m</sub>/VGN (d) NiO<sub>5m</sub>/VGN and (e) NiO<sub>10m</sub>/VGN.

From the FESEM images, it is evident that a gradual increase in NiO nanoclusters size with the deposition time but without affecting the vertically oriented networked structure of the VGN. However, curling of the vertically aligned graphene sheet edges is witnessed at higher NiO deposition time. It is attributed to higher mass loading to the VGN edges.

### 5.3.2 Structural analysis

The structural characterization of as-grown and NiO deposited VGN are carried out by Raman spectroscopy. Figure 5.13 depicts the Raman spectra of as-grown VGN and NiO deposited VGN for 30 sec, 2 min, 5 min and 10 min.

The Raman spectra of as-grown VGN consists of peaks corresponding to D (1348 cm<sup>-1</sup>), G (1582 cm<sup>-1</sup>), D' (1617 cm<sup>-1</sup>), G' (2690 cm<sup>-1</sup>) and D+D' (2936 cm<sup>-1</sup>) [83, 129, 137].

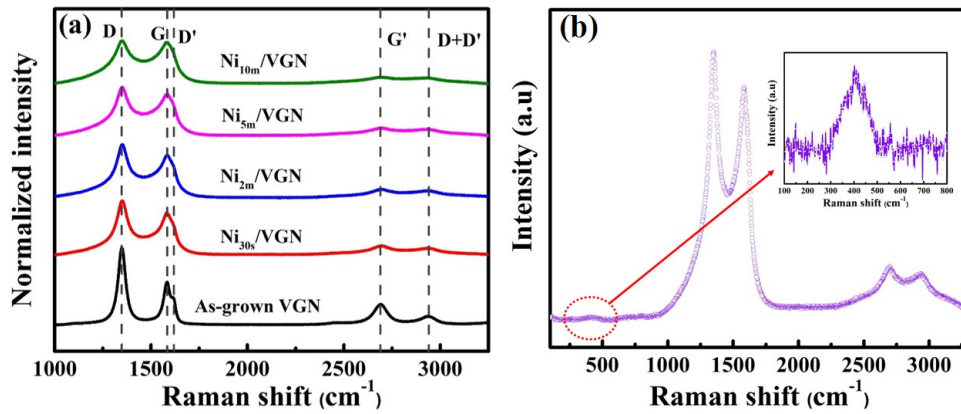


**Figure 5.13** – Shows (a) Raman spectra for as-grown and different NiO decorated VGN and (b) full spectra and inset confirms NiO peak.

The origin and the peak details are discussed in section 3.3. All the samples exhibit the characteristic Raman peaks D, G and G' of VGN. Figure 5.13(a), broadening of the D and G peaks is apparent in NiO decorated VGN samples. Also, the reduction in the intensity of D', G' and D+D' peaks is evident. Furthermore, the peaks are deconvoluted and the obtained parameters like full width at half maxima (FWHM) of peaks,  $I_D/I_G$  and  $I_{G'}/I_G$  ratios are tabulated in table 5.5.

Samples	$FWHM_D$	$FWHM_G$	$FWHM_{G'}$	$I_D/I_G$	$I_{G'}/I_G$
As-grown VGN	$47.6 \pm 0.5$	$43.5 \pm 0.1$	$86.3 \pm 1.1$	$1.81 \pm 0.02$	$0.48 \pm 0.02$
NiO <sub>30s</sub> /VGN	$75.5 \pm 1.9$	$72.2 \pm 4.5$	$123.8 \pm 3.2$	$1.35 \pm 0.02$	$0.21 \pm 0.01$
NiO <sub>2m</sub> /VGN	$76.8 \pm 2.1$	$84.4 \pm 5.2$	$139.6 \pm 4.4$	$1.23 \pm 0.01$	$0.17 \pm 0.02$
NiO <sub>5m</sub> /VGN	$106.5 \pm 3.5$	$80.4 \pm 4.5$	$142.5 \pm 3.6$	$1.21 \pm 0.02$	$0.18 \pm 0.01$
NiO <sub>10m</sub> /VGN	$120 \pm 32.6$	$85.6 \pm 1.1$	$178 \pm 2.5$	$1.13 \pm 0.02$	$0.15 \pm 0.02$

**Table 5.5** – Tabulated  $FWHM_D$ ,  $FWHM_G$ ,  $FWHM_{G'}$ ,  $I_D/I_G$  and  $I_{G'}/I_G$  for as-grown and different NiO deposited VGN.

The increase in FWHM confirms the reduction in in-plane  $sp^2$  domain size and the variation in local bonding. The intensity ratio of D and G peaks is considered an indication of the structural quality of graphene. The  $I_D/I_G$  is found to decrease with NiO decoration, which could be due to the full coverage of unsaturated edges of VGN by NiO particles. The  $I_{G'}/I_G$  ratio for all samples less than one, signifies a multilayer graphene structure and the decrease in ratio is due to the coverage of NiO nanoparticles on the surface of

the edges. Figure 5.13 shows the Raman spectra for 5 min NiO decorated VGN sample with low frequency region and the inset confirms the presence of NiO. The peak observed at the  $405\text{ cm}^{-1}$  corresponds to the  $A_{1g}$  of NiO [199].

### 5.3.3 Electrochemical capacitance study

Electrochemical capacitance measurements for as-grown and NiO decorated VGN are carried out in a 3-electrode set-up, where 1M KOH is used as the electrolyte. Platinum and Ag/AgCl are used as the counter and reference electrode, respectively. Figure 5.14(a) shows the comparative CV curve for NiO decorated VGN at 0.1 V/s scan rate in a 0.8 V potential window (-0.2 to 0.6 V) and the calculated capacitance using equation 5.1 is comparatively higher for the NiO<sub>5m</sub>/VGN i.e. 13.8 mF/cm<sup>2</sup> (Figure 5.14(b)). The obtained capacitance values for as-grown VGN, NiO<sub>30s</sub>/VGN, Ni<sub>2m</sub>/VGN and Ni<sub>10m</sub>/VGN are 0.15, 5.8, 10 and 11.9 mF/cm<sup>2</sup> respectively. The NiO<sub>30s</sub>/VGN, Ni<sub>2m</sub>/VGN and Ni<sub>10m</sub>/VGN samples exhibit similar CV and CD behavior like Ni<sub>5m</sub>/VGN. The capacitance is reduced for high NiO deposition time, which is due to the damage that occurred to the VGN structure, as confirmed from the SEM micrograph.

The NiO<sub>5m</sub>/VGN sample shows consistent CV (-0.2 to 0.6 V) and CD (0 to 0.5 V) behavior at different scan rates (0.01 to 0.5 V/s) and current densities (0.05 to 0.2 mA/cm<sup>2</sup>) respectively (Figure 5.14(c, d)). The CV and CD reflect the redox-mediated charge storage. The capacitive stability is plotted in figure 5.14(e) and found a decrease in capacitance with the scan rate, which also confirms the redox-mediated charge storage. The capacitance retention for all the NiO deposited VGN samples are plotted in figure 5.14(f), inset shows the Coulombic efficiency. The capacitance retention increased from 78 to 98 % and amongst the NiO<sub>5m</sub>/VGN shows better stability. The Coulombic efficiency is found to be in the range of 80 to 85 %.

Also, the TiO<sub>2</sub> deposition is carried out on VGN in the same condition as NiO and

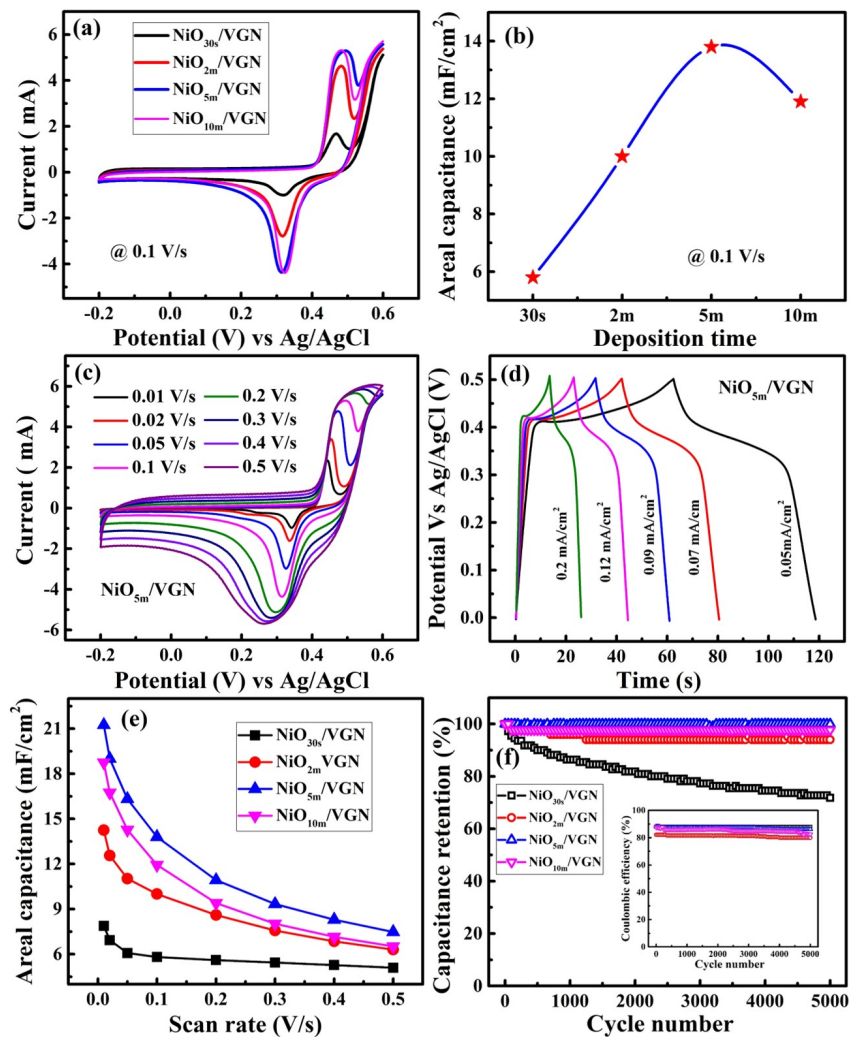


**Figure 5.14** – Shows (a) CV comparison at 0.1 V/s scan rate, (b) areal capacitance at 0.1 V/s for different NiO/VGN, (d) CV at different scan rates, (e) CD at different current densities for 5m NiO deposited VGN, (e) capacitance stability for different NiO/VGN and (f) capacitance retention for different NiO/VGN (inset shows the coulombic efficiency).

studied the capacitance performance. Conformally coating of TiO<sub>2</sub> on the VGN surface is evident from the magnified FESEM micrograph shown in figure 5.15(a). XPS spectra confirms the TiO<sub>2</sub> deposition (figure 5.15(b)). The capacitance for TiO<sub>2</sub>/VGN is found to be 2.8 mF/cm<sup>2</sup> whereas as-grown and TiO<sub>2</sub> on carbon paper shows capacitance of 0.15 and 0.06 mF/cm<sup>2</sup>, respectively (figure 5.15(c)). Figure 5.15(d) depicts the CV behavior of TiO<sub>2</sub>/VGN at different scan rates. The capacitance enhancement is due to the increase in the electrical conductivity of the hybrid electrode and presence of pseudocapacitance [200].

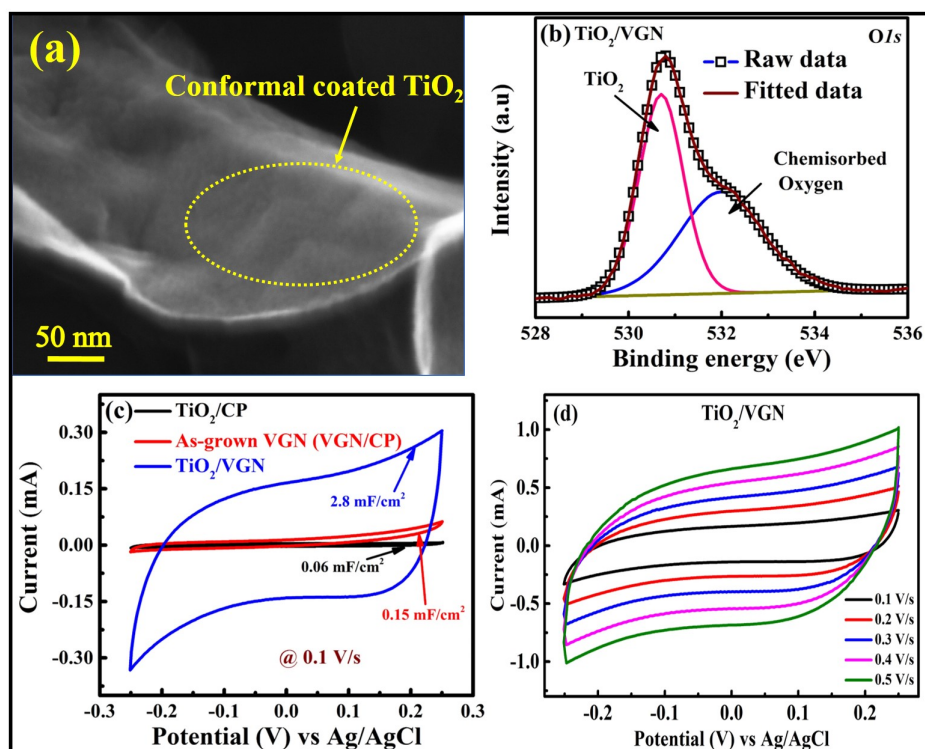


**Figure 5.15** – (a) Magnified FESEM micrograph of  $\text{TiO}_2$  decorated VGN ( $\text{TiO}_2/\text{VGN}$ ), (b)  $\text{O}1s$  spectra of  $\text{TiO}_2/\text{VGN}$ , (c) CV comparison of as-grown VGN,  $\text{TiO}_2$  decorated on carbon paper ( $\text{TiO}_2/\text{CP}$ ) and  $\text{TiO}_2/\text{VGN}$  (d) CV of  $\text{TiO}_2/\text{VGN}$  at different scan rates.

### 5.3.4 Surface chemistry analysis

The chemical structure and bonding of the as-grown and NiO decorated VGN samples are evaluated using XPS. The details about the deconvoluted  $\text{C}1s$  and  $\text{O}1s$  peak is discussed in the previous section. All the results obtained after deconvolution are tabulated in the table 5.6.

The oxygen percentage after the NiO deposition increased from 1.3 % to nearly 18 %. With different NiO deposition times, the NiO percentage is also found to increase from 10.2 ( $\text{NiO}_{30s}/\text{VGN}$ ) to 44.8 % ( $\text{NiO}_{10m}/\text{VGN}$ ). The  $sp^2$  to  $sp^3$  ratio showed a decrease with increasing NiO deposition time due to the carbon bonding with NiO nanoparticles. Further, the  $\text{O}1s$  spectra for different NiO deposited VGN are deconvoluted and found that the NiO percentage increased with the NiO deposition time. The deconvoluted  $\text{C}1s$ ,  $\text{O}1s$  and  $\text{Ni}2p$  spectra are shown in figure 5.16.

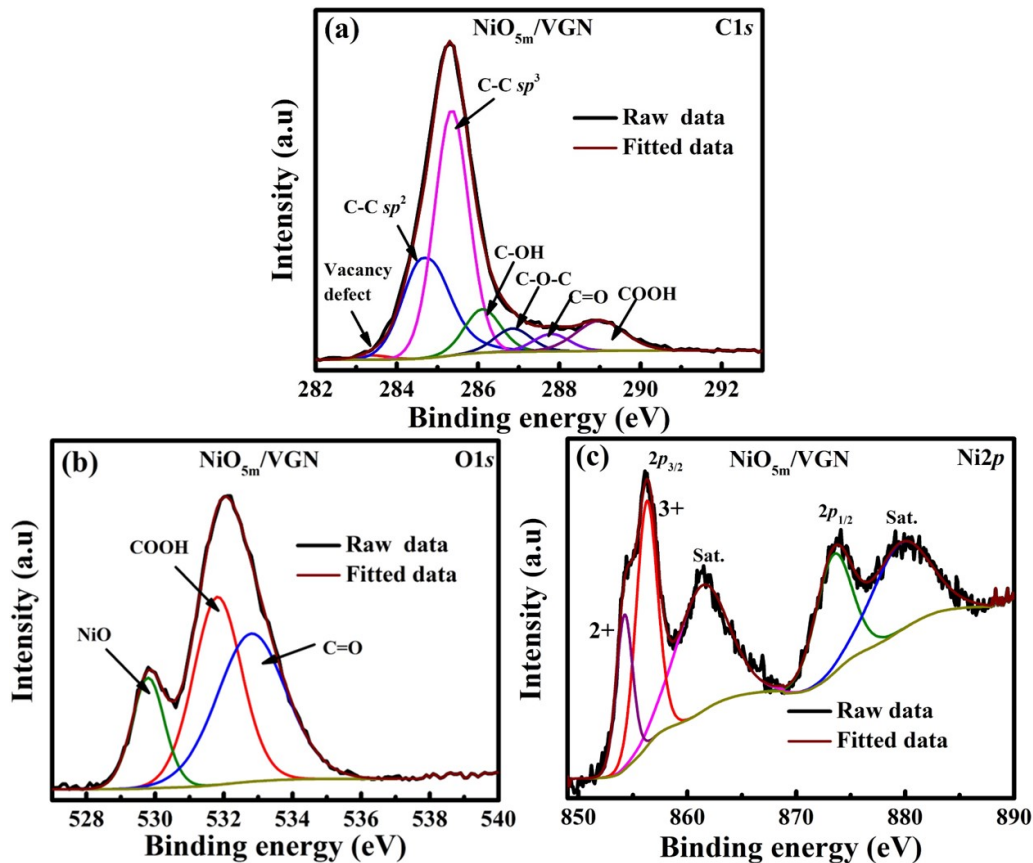
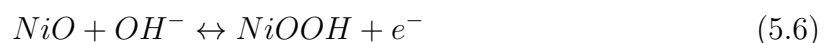


**Figure 5.16** – Shows XPS spectra: (a) C1s, (b) O1s and (c) Ni2p spectra for NiO<sub>5m</sub>/VGN.

Ni2p spectra are deconvoluted by using a Gaussian fitting method considering spin-orbit doublets and shakeup satellites. The binding energy peaks for Ni2p<sub>3/2</sub> and Ni2p<sub>1/2</sub> located at 856 eV and 874 eV, respectively (figure 5.16(c)), Ni2p<sub>3/2</sub> demonstrating the existence of both Ni<sup>2+</sup> and Ni<sup>3+</sup>. The Ni<sup>2+</sup> and Ni<sup>3+</sup> are more in samples NiO<sub>5m</sub>/VGN, although high in NiO<sub>10m</sub>/VGN but with high NiO deposition, there is damage occurred to the VGN structure (table 5.6).

This distinct peak Ni<sup>2+</sup>/Ni<sup>3+</sup> attributes reversible Faradic redox process based on the following reaction:



So pseudocapacitance plays a role in the enhancement of the capacitance and NiO<sub>5m</sub>-/VGN sample shows better capacitance performance due to the high percentage of Ni<sup>2+</sup>/Ni<sup>3+</sup>

Samples	O %	Ni %	NiO %	Ni2p <sub>3/2</sub> %	2 <sup>+</sup> %	3 <sup>+</sup> %
As-grown VGN	1.27	-	-	-	-	-
NiO <sub>30s</sub> /VGN	19.16	10.21	-	2.16	-	2.16
NiO <sub>2m</sub> /VGN	18.73	16.73	0.52	5.27	-	5.27
NiO <sub>5m</sub> /VGN	17.81	31.74	2.81	10.41	3.4	7
NiO <sub>10m</sub> /VGN	17.45	44.83	5.09	14.95	4.41	10.53

**Table 5.6** – XPS spectra fitted parameters for all NiO/VGN systems.

and undamaged VGN structure.

## 5.4 Conclusion

Vertical graphene nanosheets (VGN) are decorated with transition metal (Au, Ag, Cu and Ni) nanoparticles and demonstrated charge-storage performance. The transition metal nanoparticle (TM NP) decoration of VGN evidenced an improvement in electrical conductivity, which led to enhancement in the charge storage capacity. Amongst them, the Ni NP decorated VGN resulted in a 20 times enhancement in capacitance (3.04 mF/cm<sup>2</sup>). *Ab initio* calculations substantiated the charge-transfer process in the TM NPs/VGN hybrid, which is found to be highest for Ni/VGN. The supercapacitor performance of metal NP decorated VGN is attributed to the charge transfer and improved electrical conductivity. Additionally, in the case of both Cu and Ni decorated VGN, the pseudocapacitance induced by their oxides also contributed capacitance enhancement. Further, the NiO and TiO<sub>2</sub> NP is deposited on the VGN surface and studied their capacitance performance. The five minutes NiO deposited VGN gives a high capacitance value of 13.8 mF/cm<sup>2</sup>. The enhancement in capacitance is due to the enhancement in the Ni<sup>2+</sup>/Ni<sup>3+</sup>, which helps in Faradic redox reaction. We anticipate that our investigations will pave the way to realize the hybrid VGN electrode for supercapacitor devices with superior performance.

# Chapter 6

## Electrochemical capacitor performance of activated VGN in hybrid electrolyte

There is no great genius without a mixture of madness.

-Aristotle

### 6.1 Introduction

Supercapacitors (SCs) are becoming crucial for energy storage applications due to their high power density and superior cycle life compared to conventional batteries [52, 53, 201]. However, the low energy density of SCs compared to batteries limits their use in some applications. To achieve high energy density, interconnected porous vertical graphene nanosheets (VGN) have proved to be leading SC electrode materials due to the remarkable properties such as high surface area, sharp edges, good electrical conductivity and easy functionalization [15, 119, 202–205].

Although the active electrode material is important for the SC performance, the electrolyte and its concentration also play significant roles. The ever-rising demand for high energy density device drives the research community to aim on novel electrolytes to improve capacitance [112]. Moreover, the electrolyte and its interaction with electrode

helps to enhance the SC device's potential window. Since VGN are one of the promising SC electrode material, here the focus mainly lies on finding out a potential electrolyte to achieve enhanced storage performance. The aqueous electrolytes are environmental friendly, safe and cost-effective but the limitation of narrow operational potential window gives low SC performance. Recently, a lot of research for high capacitance SC is being reported on ionic and organic electrolytes, because they help to extend the potential window. Besides the use of aqueous, ionic or organic electrolytes, recent research is focused on hybrid electrolytes, for improving the performance of SC. For example, iso-propanol added aqueous electrolytes [115], acetate aqueous electrolytes [114], aqueous solution of acidic ionic liquid [116], hydroquinone doped hybrid gel electrolytes [118] and ionic liquid added polymer electrolytes [117] are reported for enhanced capacitance and working potential window. Therefore the research to enhance the capacitance and extending the potential window using hybrid electrolyte is still under active research.

Further, the electroactive surface area has an important role in the SC performance, which is mainly controlled by the wetting nature of the electrode surface. But, VGN is hydrophobic and restricts the surface for access of electrolyte [117]. This can be overcome by the functionalization of VGN surface with some polar groups [156]. In **chapter-3** it is found that there is an enhancement in wettability and SC performance by *in-situ* oxygen plasma treatment [155, 156]. However, chemical functionalization is a very easy and cost-effective way. It is reported that KOH is widely used in the activation process to improve SC performance and also generate nanoscale pores in carbon nanostructures [47, 121]. Hence, our interest is to activate VGN and study the SC performance in a hybrid electrolyte.

The present chapter demonstrates an approach based on the combination of surface activation and utilization of a organo-aqueous hybrid electrolyte, tetraethylammonium tetrafluoroborate ( $\text{TEABF}_4$ ) in  $\text{H}_2\text{SO}_4$ , to achieve enhancement in SC performance of

VGN. The study manifests the importance of hybrid electrolyte in enhancing the areal capacitance ( $1.99 \text{ mF cm}^{-2}$ ) with capacitance retention of 94.6% after 5000 cycles. Also, a five fold enhancement in the capacitance of VGN ( $0.64$  to  $3.31 \text{ mF cm}^{-2}$ ) is achieved by the combination of KOH activation of VGN with the hybrid electrolyte.

## 6.2 Growth and activation of VGN

Microwave plasma-enhanced chemical vapor deposition is used for the growth of VGN. The detailed procedure of growth is described in **chapter-3**. After the growth, VGN is dipped in KOH solution for 28 h to activate the VGN surface. As KOH is an oxidizing agent that grafts the functional group to the surface and improves the quality of the material [84]. The activation of VGN in the KOH medium proceeds as [120],



After activation, the VGN was rinsed with de-ionized water several times and dried at room temperature.

## 6.3 Morphology and structural analysis

The morphology of VGN grown on carbon paper is depicted in figure 6.1(a). The high-resolution FESEM micrograph in figures 6.1(b) and (c) confirm the uniform growth and porous structure of vertically aligned graphene sheets with transparent sheets at the edges. Figure 6.1(c) shows the presence of transparent thin sheets at the top of each edges, which acts as the active sites. This 3-D porous structure with exposed surface provides sites for the functional groups and electrolyte ions to interact to form an electric double layer. A trivial change in the VGN morphology after the KOH activation process confirms the stability of the structure. However, the highly magnified image shows the

nanopore formation on the nanosheets after the activation process (figure 6.1(d)).

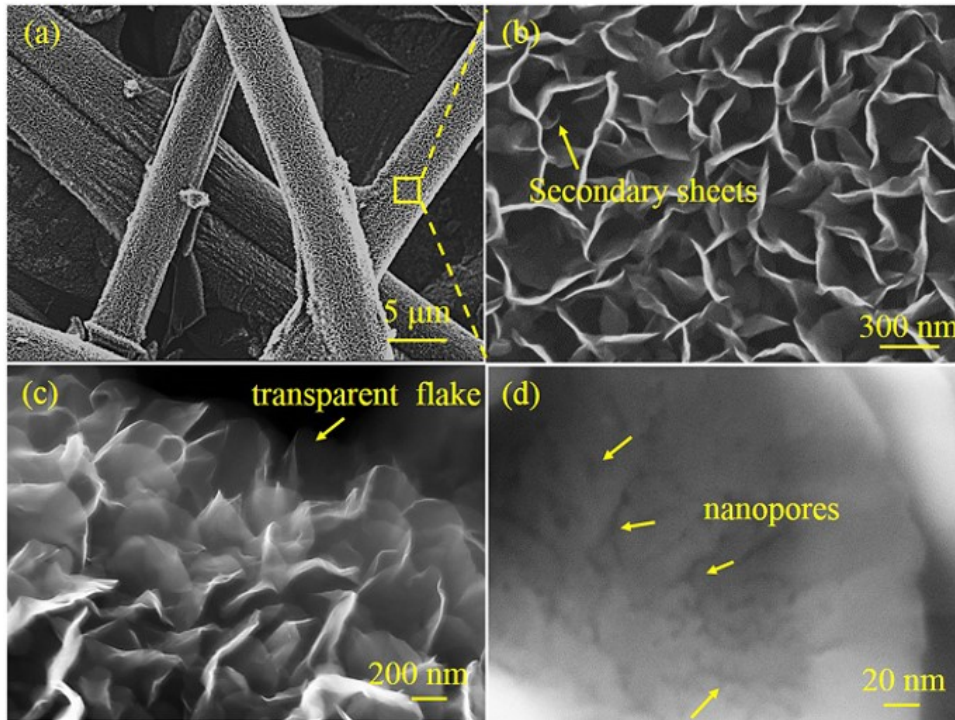


**Figure 6.1** – (a)-(c) SEM micrograph of VGNC with different magnifications (d) Magnified image of single nanosheets after KOH activation.

Raman spectra of as-grown and activated VGNC are depicted in figure 6.2. Typical Raman spectra of VGNC consists of prominent peaks D-band ( $1350\text{ cm}^{-1}$ ), G-band ( $1580\text{ cm}^{-1}$ ), and  $G'$  ( $2700\text{ cm}^{-1}$ ) [129, 137]. The D-band corresponds to the breathing mode of hexagonal rings and disorder-induced band, whereas, in-plane vibration of  $sp^2$  bonded carbon in the ring and chain form/fashion is attributed to the G-band ( $E_{2g}$  symmetry). The  $G'$ -band arises due to the double resonance process, and it is a measure of number of graphene layers present in the structure [136]. The D band and other defect related bands,  $D''$ -band ( $1100\text{ cm}^{-1}$ ) and  $D'$ -band ( $1620\text{ cm}^{-1}$ ), and their overtones at  $2456$ ,  $2945$ , and  $3240\text{ cm}^{-1}$  confirm the presence of defects due to huge edge density, high ion bombardment, heptagon-pentagon structure and presence of C-H bonds [83, 139]. An insignificant difference between the normalized Raman spectra of as-grown and activated VGNC confirms the retention of the structural quality (figure 6.2). The FWHM ( $\Gamma$ ) of the

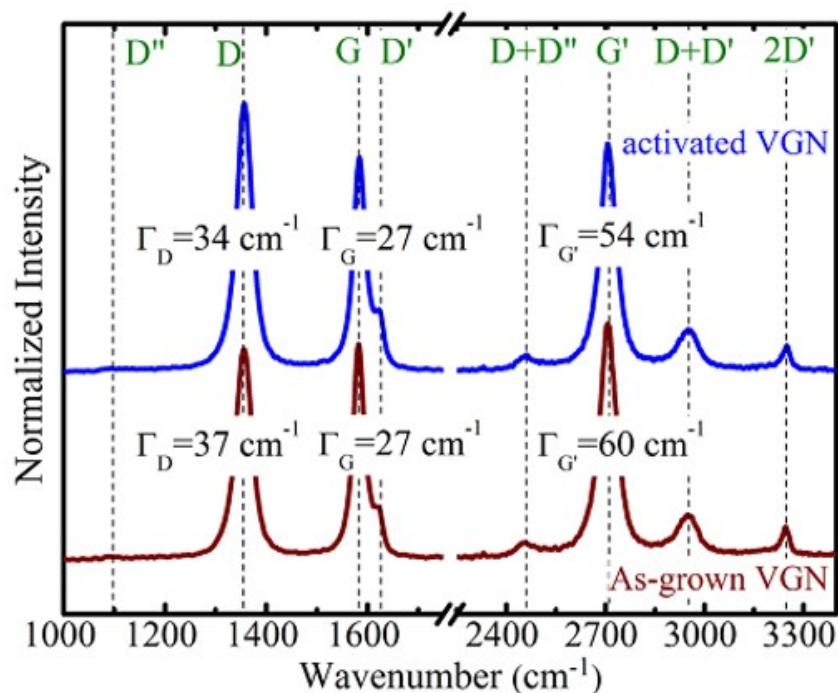


**Figure 6.2** – Raman spectra of as-grown and activated vertical graphene nanosheets.

G'-band for both as-grown and KOH activated VGN is lying within the range of 53-64  $\text{cm}^{-1}$  signifies the formation of few-layered graphene sheets. The KOH activation serves to graft the oxygen functional groups, leading to a reduction in the FWHM of D and G' bands and in-turn improves the graphitic structure. However, increased D-band intensity in activated VGN might be due to the formation of nanopores in the structure and hence more defect or disorder density [121].

## 6.4 Water contact angle measurement

The wetting property of the electrode material depends on the capacitance performance. The higher the wettability, the better electrode-electrolyte interaction and in-turn, improved SC performance.

The as-grown VGN shows hydrophobic characteristics with a water contact angle of  $137^\circ$ , as illustrated in figure 6.3(a). The hydrophobicity of VGN is attributed to the interconnected porous network and non-polar C-H bonds. There is a reduction in water

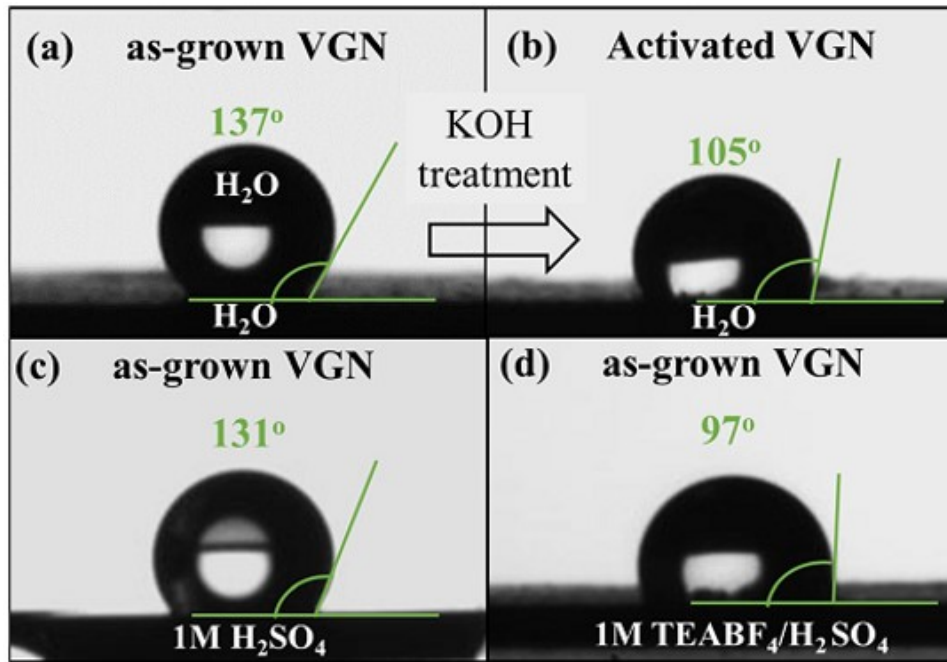


**Figure 6.3** – Water contact angle of (a) as-grown and (b) activated VG N, contact angle of as-grown VG N in (c) 1M H<sub>2</sub>SO<sub>4</sub>, and (d) 1M TEABF<sub>4</sub>/H<sub>2</sub>SO<sub>4</sub>.

contact angle by 30° is observed after KOH activation (figure 6.3(b)). The oxidizing nature of the KOH helps to saturate the dangling bonds at edges and defects in basal planes with oxygen functional groups, so a reduction in wettability. Hence, the activation process not only improved the graphitic structure also rearranged the structures without disturbing the morphology. In addition, the contact angle of as-grown VG N in 1M H<sub>2</sub>SO<sub>4</sub> and 1M TEABF<sub>4</sub>/H<sub>2</sub>SO<sub>4</sub> is measured to be 131° and 97°, respectively (figure 6.3(c) and (d)). It confirms the improved wettability of VG N with the hybrid electrolyte.

## 6.5 Surface chemistry analysis

X-ray photoelectron spectra of activated VG N is carried out to investigate the chemical changes after the activation process. The survey spectra of as-grown and activated VG N are compared and illustrated in figure 6.4(a). Clearly, a high intense O1s peak at 532.5 eV and O<sub>KLL</sub> Auger band around 974 eV is observed in the activated VG N. The calculated O<sub>2</sub> content for the as-grown and activated VG N is found to 1.5% and 4.5%, respectively.

Which confirms the oxygen functionalization after the activation. Hence, the reduction in wettability can be attributed to the oxygen functionalization through KOH activation. Also, the fitted C1s spectra for both as-grown and activated VGN are shown in figures 6.4(b) and (c). The typical C1s spectra consists of  $sp^2$ -C at 284.4 eV,  $sp^3$ -C at 284.82 eV and defect peak at 283.88 eV along with oxygen functional groups [138, 139].

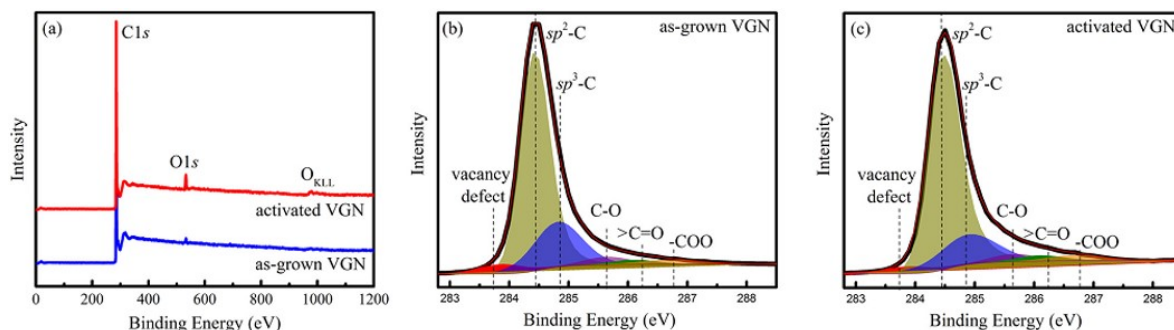


**Figure 6.4** – (a) XPS survey spectra of as-grown and activated VGN and C1s spectra of (b) as-grown and (c) activated VGN.

A reduction in area under the vacancy defect peak from 4.3 to 2.8 % is observed from figures 6.4(b) and (c) and an increase in the  $sp^2/sp^3$  ratio from 3 to 4.2. Which indicates an improvement in the graphitic structure after the activation process. So, the XPS result corroborates well with the above mentioned Raman spectroscopic result.

## 6.6 Electrochemical capacitance study

The electrochemical capacitance study on as-grown and activated VGN were carried out by conducting cyclic voltammetry (CV), galvanostatic charge-discharge (CD), and electrochemical impedance spectroscopy (EIS). The electrochemical measurements were carried out in a 3-electrode configuration using the Metrohm-Autolab workstation (model PGSTAT302N). A  $1 \times 1 \text{ cm}^2$  area of the as-grown and activated VGN were used as working electrodes, whereas platinum foil and Ag/AgCl (KCl saturated) were used as counter and reference electrodes, respectively. Aqueous  $\text{H}_2\text{SO}_4$  and  $\text{TEABF}_4/\text{H}_2\text{SO}_4$  of 1M concentration were used as electrolytes.  $\text{TEABF}_4/\text{H}_2\text{SO}_4$  was prepared by dissolving  $\text{TEABF}_4$

in 1M H<sub>2</sub>SO<sub>4</sub> solution.

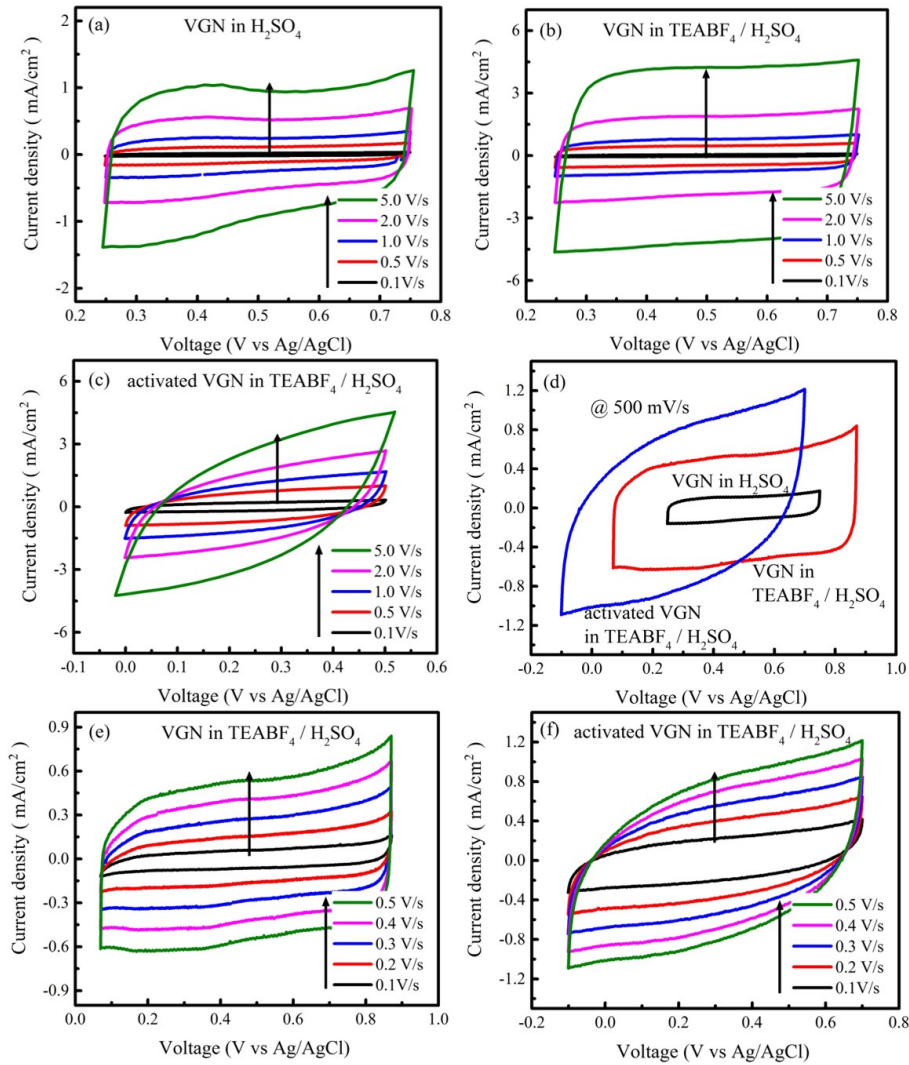


**Figure 6.5** – CV of (a) VGN in 1M H<sub>2</sub>SO<sub>4</sub>, (b) VGN in 1M TEABF<sub>4</sub>/H<sub>2</sub>SO<sub>4</sub>, and (c) activated VGN in 1M TEABF<sub>4</sub>/H<sub>2</sub>SO<sub>4</sub>; (d) comparative CV at the 500 mV/s scan rate; CV with an extended potential window of (e) VGN in 1M TEABF<sub>4</sub>/H<sub>2</sub>SO<sub>4</sub> and (f) activated VGN in 1M TEABF<sub>4</sub>/H<sub>2</sub>SO<sub>4</sub>

The areal capacitance ( $C_A$  in F/cm<sup>2</sup>) was estimated from the CV and CD profile using the following equations,

$$C_A = \frac{\int idV}{\Delta V \times A \times s} \quad (6.2)$$

$$C_A = \frac{I \times t_d}{A \times \Delta V} \quad (6.3)$$

where  $\int idV$  is the area under CV,  $I$  is the charge-discharge current,  $s$  is the scan rate

of CV,  $\Delta V$  is the potential window,  $A$  is the exposed area of working electrode in the electrolyte and  $t_d$  is the discharge time of the CD profile.

The capacitance retention (CR) and Coulombic efficiency ( $\eta$ ) was obtained from the CD profile using the following equation,

$$CR = \frac{t_{d_n}}{t_{d_1}} \times 100 \quad (6.4)$$

$$\eta = \frac{t_d}{t_c} \times 100 \quad (6.5)$$

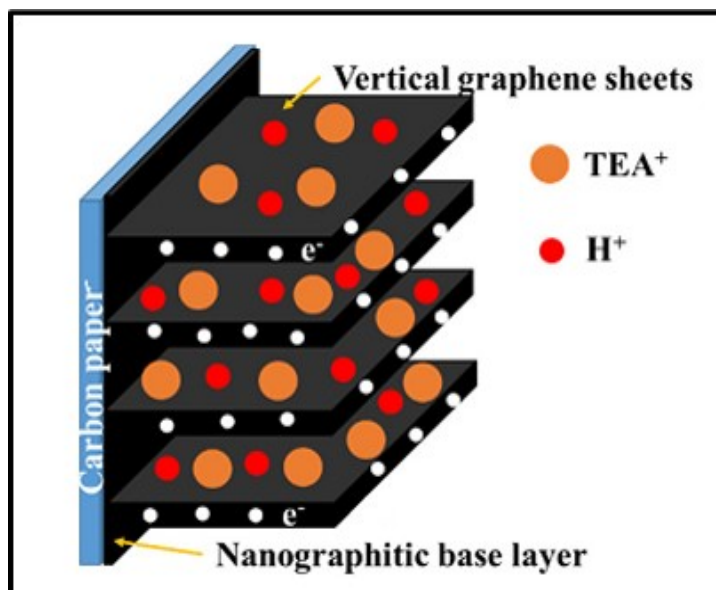
where,  $t_c$  and  $t_d$  is the charging and discharging time respectively,  $t_{d_n}$  is the discharging time for  $n^{th}$  cycle,  $t_{d_1}$  is the discharging time for  $1^{st}$  cycle and  $n= 1, 2, \dots, n$ .

Figure 6.5(a), (b) and (c) demonstrates a near rectangular, a perfect rectangular, and an oval-shaped cyclic voltammogram (CV) for the VGN in  $H_2SO_4$ , VGN in the  $TEABF_4/H_2SO_4$  system and activated VGN in the  $TEABF_4/H_2SO_4$  system, respectively. The potential window is confined to 0.5 V for  $H_2SO_4$  to exclude the possibility of Faradic contributions from electrolyte decomposition and hydrogen storage [114]. Some existing literature on VGN [81, 93] and other nanostructures such as defect engineered graphene [206], single-walled carbon nanotubes (CNTs) [207] and self doped  $TiO_2$  arrays [208] also reported 0.5 V potential window. The CV for  $TEABF_4/H_2SO_4$  electrolyte was also carried out in a 0.5 V potential window for a comparison purpose. Remarkably, similar shapes of CV from 0.1 to 5 V/s scan rates are noticed. A higher current response of the VGN in  $TEABF_4/H_2SO_4$  compared to VGN in  $H_2SO_4$  is observed in figure 6.5(a) and (b). However, further enhancement in area under the CV curve and hence improved charge storage is seen for the activated VGN (figure 6.5(c)). This can be attributed to the enhanced wetting characteristics. The maximum supercapacitance of VGN in  $H_2SO_4$ , VGN in  $TEABF_4/H_2SO_4$ , and activated VGN in  $TEABF_4/H_2SO_4$  estimated from CV are 0.64,

1.99, and 3.31 mF/cm<sup>2</sup>, respectively. The observed experimental findings emphasize the potential of the present electrode-electrolyte combination for SC applications.

It is already reported that the capacitance value of VGN can be improved by functionalizing with hetero-atoms [209], tuning the wettability [93] and varying the morphology [94]. Also, KOH activated VGN TEABF<sub>4</sub>/H<sub>2</sub>SO<sub>4</sub> shows a higher areal capacitance compared to VGN in TEABF<sub>4</sub>/propylene carbonate (PC) (1.1 mF/cm<sup>2</sup>), TEABF<sub>4</sub>/AN (1.4 mF/cm<sup>2</sup>) [210], 1M LiClO<sub>4</sub> in PC (2 mF/cm<sup>2</sup>) [93], ionic electrolyte (2.2 mF/cm<sup>2</sup>) [98] and polymer electrolyte (2.45 mF/cm<sup>2</sup>) [133], as well as other nanostructures such as SWCNTs (0.55 mF/cm<sup>2</sup>) [207], defect engineered graphene in 0.25 M TEABF<sub>4</sub>/AN (0.75-56.6 μF/cm<sup>2</sup>) [206], and 1.6 μm long self-doped TiO<sub>2</sub> (0.91 mF/cm<sup>2</sup>) [208]. In addition, the volumetric capacitance of activated VGN is found to be 9.19 F/cm<sup>3</sup>, which is higher than that of reduced graphene oxide and its composite [118]. Therefore, the usage of TEABF<sub>4</sub>/H<sub>2</sub>SO<sub>4</sub> and surface activation by KOH not only for the improvement of SC performance of VGN but also to open up a new window for other carbon based electrode materials. Moreover, an extension of potential window by 0.3 V is observed in TEABF<sub>4</sub>/H<sub>2</sub>SO<sub>4</sub> solution. The comparison of CV shape for all the samples is depicted in figure 6.5(d). The CV of VGN and activated VGN in TEABF<sub>4</sub>/H<sub>2</sub>SO<sub>4</sub> in the extended potential window with different scan rates are depicted in figure 6.5(e) and (f), respectively. The enhancement in the capacitance value is attributed to the presence of both cations (TEA<sup>+</sup> and H<sup>+</sup>) and improved wettability in the hybrid electrolyte (the schematic is provided in figure 6.6).

Further to confirm the enhancement in SC performance, the CD test of VGN and activated VGN is carried out in aqueous and hybrid electrolyte (figure 6.7(a-c)). It is noticed that the CD profiles are symmetrical at various current densities, which indicates excellent CD behavior. The higher area under the CD profile of activated VGN in the hybrid electrolyte indicates its quality performance (figure 6.7(c)). The areal capacitance of



**Figure 6.6** – Schematic of the different ion adsorbed VGN electrode in TEABF<sub>4</sub>/H<sub>2</sub>SO<sub>4</sub>.

VGN and activated VGN are calculated using equation 6.3. The highest capacitance obtained for the activated VGN in TEABF<sub>4</sub>/H<sub>2</sub>SO<sub>4</sub> is 2.85 mF/cm<sup>2</sup> at a current density of 0.05 mA/cm<sup>2</sup>. The calculated areal capacitance for the VGN in 1M H<sub>2</sub>SO<sub>4</sub> and 1M TEABF<sub>4</sub>/H<sub>2</sub>SO<sub>4</sub> is 0.62 and 1.48 mF/cm<sup>2</sup>, respectively. Figure 6.7(d) shows the variation of the areal capacitance of the VGN/electrolyte systems with different current densities. The decrease in capacitance for the activated VGN with current density indicates the pseudocapacitance nature due to presence of oxygen groups. The Coulombic efficiency of the VGN with different electrolyte systems are calculated using equation 6.5. VGN in TEABF<sub>4</sub>/H<sub>2</sub>SO<sub>4</sub> shows 93.1 % Coulombic efficiency at 0.05 mA/cm<sup>2</sup> and 82.5 % at 0.5 mA/cm<sup>2</sup>.

Cycle stability is one of the important parameter to evaluate the SC performance. A comparative result of the cyclic stability of VGN in 1M H<sub>2</sub>SO<sub>4</sub>, VGN in TEABF<sub>4</sub>/H<sub>2</sub>SO<sub>4</sub> and activated VGN in TEABF<sub>4</sub>/H<sub>2</sub>SO<sub>4</sub> is demonstrated in figure 6.8(a). VGN in H<sub>2</sub>SO<sub>4</sub> and TEABF<sub>4</sub>/H<sub>2</sub>SO<sub>4</sub> exhibited cycle stabilities of 98.9 % and 94.6 %, respectively after 5000 CD cycles (calculated by using equation 6.4). The areal capacitance of activated VGN in TEABF<sub>4</sub>/H<sub>2</sub>SO<sub>4</sub> is dropped only by 7.1 % after 5000 charge-discharge cycles.

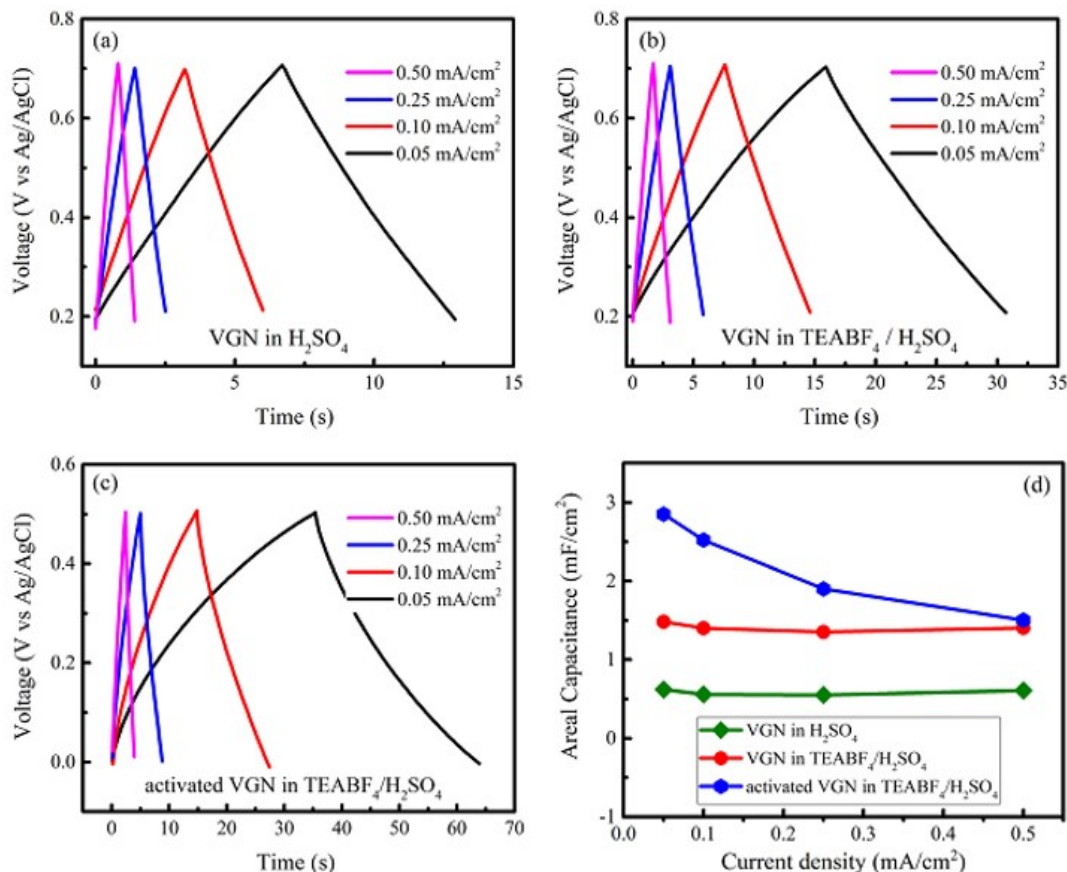


**Figure 6.7** – CD profile of (a) VGN in 1M H<sub>2</sub>SO<sub>4</sub>, (b) VGN in 1M TEABF<sub>4</sub>/H<sub>2</sub>SO<sub>4</sub>, and (c) activated VGN in 1M TEABF<sub>4</sub>/H<sub>2</sub>SO<sub>4</sub>; (d) variation of the areal capacitance of VGN in 1M H<sub>2</sub>SO<sub>4</sub>, VGN in TEABF<sub>4</sub>/H<sub>2</sub>SO<sub>4</sub>, and activated VGN in TEABF<sub>4</sub>/H<sub>2</sub>SO<sub>4</sub> with respect to current density in the range of 0.05 mA/cm<sup>2</sup> to 0.5 mA/cm<sup>2</sup>.

Also, the cyclic stability of the activated VGN in the hybrid electrolyte is verified from CV after the cyclability test (figure 6.8(b)).

Electrochemical impedance spectroscopy (EIS) was carried out to obtain further insights into the electrode-electrolyte interaction [211]. Figure 6.9 depicts the impedance responses at an open circuit alternate current perturbation of 10mV in the frequency range of 100 kHz to 10 mHz. Almost a vertical line in the Nyquist plot for all the samples confirm near-ideal SC behaviour (figure 6.9(a)). The equivalent circuit used to fit the impedance spectra is shown in the inset of figure 6.9(a). The component of the equivalent circuit is the equivalent series resistance ( $R_s$ ), double layer capacitance ( $C_{dl}$ ), charge transfer resistance ( $R_{ct}$ ) and Warburg component ( $Z_w$ ). The  $Z'$  intercepts in the Nyquist plot

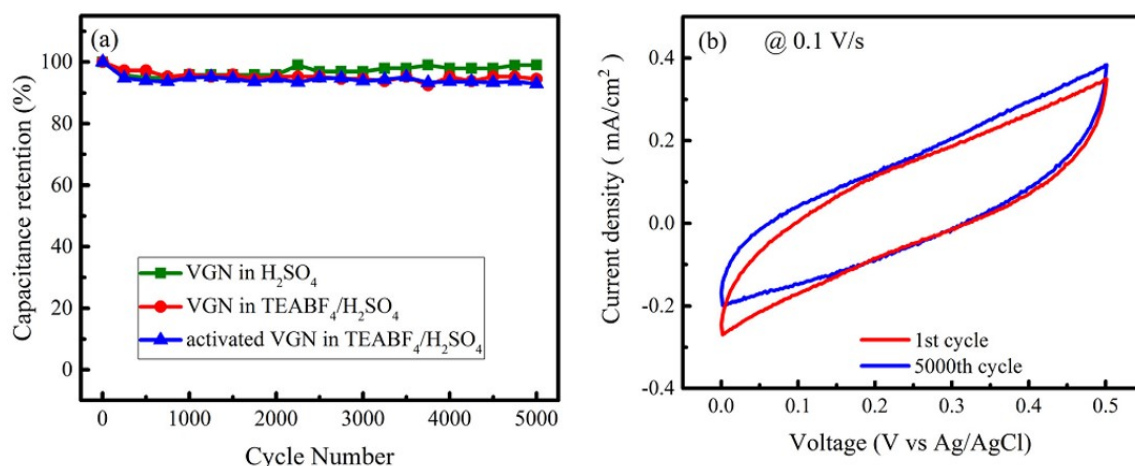


**Figure 6.8** – (a) Capacitance retention with respect to the CD cycle number and (b) comparison of CV after the cyclability test for activated VGN in TEABF<sub>4</sub>/H<sub>2</sub>SO<sub>4</sub> at 0.1 V/s.

is a measure of equivalent series resistance ( $R_s$ ). The  $R_s$  values found from the fitting are 3.03, 2.56 and 1.28  $\Omega$  for VGN in H<sub>2</sub>SO<sub>4</sub>, VGN in TEABF<sub>4</sub>/H<sub>2</sub>SO<sub>4</sub> and activated VGN in TEABF<sub>4</sub>/H<sub>2</sub>SO<sub>4</sub> electrolyte, respectively. It is observed that there is a reduction of  $R_s$  after the activation of VGN (figure 6.9(a)). The low  $R_s$  of activated VGN in TEABF<sub>4</sub>/H<sub>2</sub>SO<sub>4</sub> ensures an effective ion accumulation at the electrolyte-electrode interface.

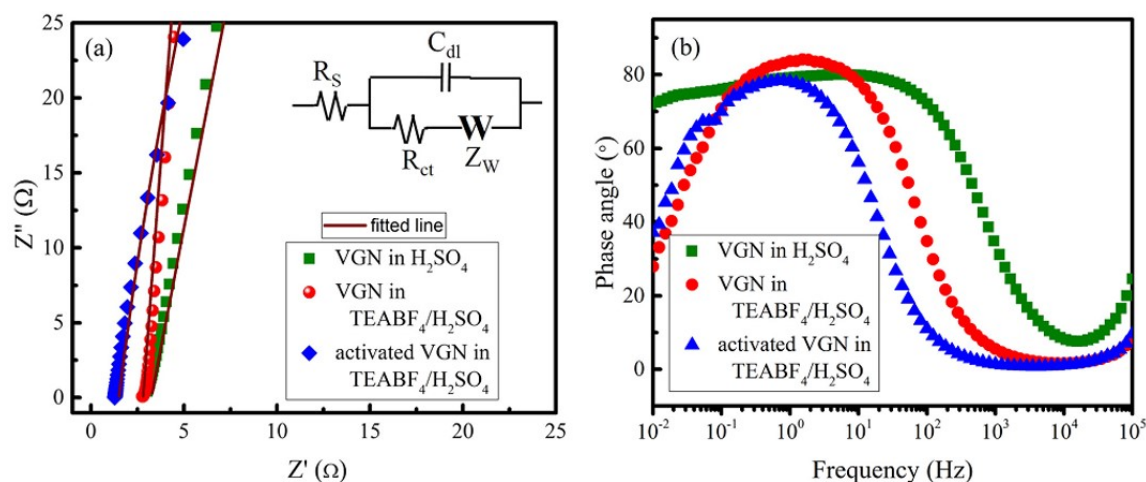


**Figure 6.9** – Impedance responses of VGN in H<sub>2</sub>SO<sub>4</sub>, VGN in TEABF<sub>4</sub>/H<sub>2</sub>SO<sub>4</sub> and activated VGN TEABF<sub>4</sub>/H<sub>2</sub>SO<sub>4</sub>: (a) Nyquist plot and (b) Bode plot. The inset of (a) represents the equivalent circuit used for impedance curve fitting.

The phase angle versus frequency is plotted in figure 6.9(b). The phase angle of 90 $^\circ$  is

indicative of ideal SC behaviour. The maximum phase angle obtained for VGN in 1M  $\text{H}_2\text{SO}_4$ , VGN in  $\text{TEABF}_4/\text{H}_2\text{SO}_4$  and activated VGN in  $\text{TEABF}_4/\text{H}_2\text{SO}_4$  is  $79.6^\circ$ ,  $84.1^\circ$  and  $78.3^\circ$ , respectively. The reduced phase angle behavior for the  $\text{TEABF}_4/\text{H}_2\text{SO}_4$  electrolyte at a lower frequency can be attributed to the difficulty in accessing the electrode surface by the  $\text{TEA}^+$  electrolyte ion and can be avoided by engineering the nanoarchitecture not to block the ions [212]. The results obtained are the proof for potential usage of the hybrid electrolyte (aqueous electrolyte with organic salt) with the KOH activation process for higher charge storage capacity and extended operating potential window.

## 6.7 Conclusion

In summary, 3D porous and self-supported vertical graphene nanosheets exhibited enhanced supercapacitor performance combined with the organo-aqueous hybrid electrolyte and KOH activation. The hybrid electrolyte  $\text{TEABF}_4/\text{H}_2\text{SO}_4$  boosts the energy storage capacity by five folds and also extends the potential window from by 0.3 V (0.5 to 0.8 V). An unchanged cyclic voltammogram of VGN in the hybrid electrolyte at different scan rates ranging from 0.1 to 5 V/s assures efficient electrolyte ion access to the electrode material's interior surfaces. Herein, we demonstrated a viable strategy of KOH activation of VGN with the preserved morphology, improved wettability and structural quality. This study will pave the way to new combinations of the organo-aqueous electrolyte and chemical activation to achieve superior charge storage capacity of novel nanostructures based supercapacitors.

# Chapter 7

## Summary and future scope

The thesis primarily focused on improvement of the charge storage capacity of vertical graphene nanosheets (VGN). Herein, the capacitance enhancement is achieved by surface modification (plasma activation and metal/metal oxide decoration) of the VGN, while retaining its unique geometry. An effort is made to understand the role of surface functionalization and charge-transfer on capacitance performance. Also, a simple and easily scalable polymer-free transfer process is established to fabricate VGN based flexible supercapacitor device. Furthermore, the combination of hybrid electrolyte (Tetraethylammonium tetrafluoroborate + sulfuric acid) with chemical activation is attempted to enhance the charge storage performance of VGN electrodes. The summary of the individual chapter is also discussed below.

### 7.1 Summary of the Thesis

Chapter 1 introduced the structure and unique properties of the vertical graphene nanosheets and the basic electrochemical capacitor concepts. An up to date literature survey of the VGN electrode for electrochemical capacitor application is also covered. This chapter reported the literature on various methods adopted to enhance the capacitance performance of VGN electrodes such as surface functionalization, metal decoration, chemical activation and usage of hybrid electrolytes, etc. Furthermore, the novel process for the

development of flexible electrodes is also detailed. Chapter 2 provided a brief description of the growth techniques used to synthesize VGN, surface modification/activation of VGN and metal nanoparticle decoration on VGN. It also discussed the characterization techniques employed to evaluate the morphology, structure and chemical analysis. Also, a brief introduction to electrochemical measurement, principles for cyclic voltammetry, galvanostatic charge-discharge curve and electrochemical impedance spectroscopy (EIS) are presented.

The major findings of the present thesis are briefed as follows:

Chapter 3:

1. An easily scalable polymer-free scalable transfer of vertical graphene nanosheets onto a flexible substrate is developed.
2. Retention of morphology, surface chemistry and structural quality of VGN upon transfer onto polymer substrate is achieved.
3. The fabrication of the supercapacitor device without any current collector and binder proved the utility of transferred VGN electrode.

Chapter 4:

1. Transformation of intrinsic hydrophobic VGN into super-hydrophilic is achieved by post oxygen plasma treatment while preserving the unique interconnected porous structure.
2. Functionalization of VGN electrodes with preferential groups such as C-OH (hydroxyl) and C=O (carbonyl) is achieved.
3. The super-hydrophilic VGN exhibited a 10 times enhancement in capacitance value.

Chapter 5:

1. A significant enhancement in the charge storage capacity of metal nanoparticles (NPs) decorated VGN electrodes is observed. Amongst the Ni NPs decorated VGN is resulted nearly 20 times enhancement in capacitance from 0.15 to 3.04 mF/cm<sup>2</sup>.

2. The supercapacitor performance of NPs/VGN hybrid structure is due to the synergetic effect of i) charge transfer because of the work function mismatch between NPs and VGN network ii) Pseudocapacitance induced by the oxide part of NPs.
3. The NiO NP is deposited on the VGN surface and capacitance performance is further improved upto 13.8 mF/cm<sup>2</sup>.

Chapter 6:

1. The combination of organic and aqueous hybrid electrolyte with KOH etching of VGN exhibited good supercapacitor property.
2. The hybrid electrolyte not only enhanced the charge storage capacity by five times but also extends the potential window by 0.3 V.

## 7.2 Future scope

1. Combination of metal/metal oxide and plasma activation for high energy density supercapacitors.
2. Heteroatom decoration of vertical graphene nanosheets and its effect on electrochemical capacitor performance.
3. Surface sulphonation and phosphorization of VGN and electrochemical capacitance performance.

## Abstract

Vertical graphene nanosheets (VGN), a graphene derivative, is an ensemble of vertically standing few-layer graphene sheets of few tens of nanometer-thick, has drawn significant attention of the research community, for supercapacitor (SC) applications. The present thesis addresses two things: first is to develop a polymer-free transfer process of VGN for flexible supercapacitor applications. Second is the improvement in capacitance of VGN based electrode by surface modification (plasma activation and metal/metal oxide decoration) while retaining its unique geometry. The combination of hybrid electrolyte and chemical activation is also explored to enhance the capacitance performance of VGN electrodes. The findings of the thesis work are listed below.

The rapid growth of wearable electronics popularity in the past decade has resulted a strong interest in flexible electronics. Presently, for this application the most commonly employed approach for the transfer of graphene relies on the chemical etching of underlying substrates and involves protection polymers. Polymer removal is one of the difficult tasks in this process. A polymer-free and scalable technique adopted to transfer the VGN onto a flexible substrate without disrupting its structure and properties in the present work. The charge storage capacity is also studied by fabricating a flexible symmetric supercapacitor device using the transferred VGN electrodes free of binder and current collector.

Generally, as-grown VGN is hydrophobic, which restricts the electrolyte ion to access the entire electrode surface. In contrast, hydrophilic surfaces are most desired for better electrode wettability, which improves the interaction with electrolyte and, in-turn the capacitance performance. Therefore, hydrophilic VGN structures are achieved by post oxygen plasma treatment while retaining its geometry. The super-wetting VGN

electrode exhibited a ten-time (0.15 to 1.6 mF/cm<sup>2</sup>) enhancement in capacitance performance. Further, the preferentially functionalization by specific type of oxygenated groups is achieved by post deposition plasma treatment. Moreover, the correlation between the type of oxygen functional groups (hydroxyl, carbonyl and carboxyl) with wetting nature, ageing rate of wettability and supercapacitor performance of VGN surfaces is established. The significant role of process parameters towards achieving hydrophilic VGN surfaces with long-term stability is brought out. The capacitance performance of VGN samples undergone oxygen plasma treatment is also compared with the ones treated with H<sub>2</sub> and N<sub>2</sub> plasmas also. Finally, a tandem device of solid-state symmetric supercapacitor is fabricated and used to light up a light-emitting-diode to demonstrate its practicability. The present thesis studied the influence of the transition metal nanoparticles (NPs) decoration of a VGN structure on its capacitance performance. Also, It is expected that a VGN with a homogeneous decoration of metal NPs will further improve its conductivity and facilitate an easy ion insertion/extraction into the structure. The energy storage performance is correlated with the charge transfer that occurs due to the mismatch in the work function. The Ni decorated VGN exhibited highest charge transfer (+0.48 e) and capacitance (3.04 mF/cm<sup>2</sup>). Further, the metal oxide (NiO and TiO<sub>2</sub>) nanoparticle decoration on VGN is carried out and studied the capacitance performance.

Although the electrode material is crucial, the choice of electrolyte and its concentration also play significant roles in enhancing capacitance and potential window of the capacitor. Additionally, the electroactive surface of the electrode also has a crucial role in determining the SC performance, which is mainly controlled by the wetting nature of the electrode. A novel approach based on the combination of KOH surface activation and an organo-aqueous hybrid electrolyte, tetraethylammonium tetrafluoroborate (TEABF<sub>4</sub>) in H<sub>2</sub>SO<sub>4</sub> is carried out and achieved significant enhancement from 0.64 to 3.31 mF/cm<sup>2</sup> in SC performance of VGN.

# References

- [1] K. S. Novoselov, V. Fal, L. Colombo, P. Gellert, M. Schwab, K. Kim *et al.*, *nature*, 2012, **490**, 192–200.
- [2] K. S. Novoselov and A. Geim, *Nat. Mater*, 2007, **6**, 183–191.
- [3] C. Ataca, H. Sahin and S. Ciraci, *The Journal of Physical Chemistry C*, 2012, **116**, 8983–8999.
- [4] Y. Gao, Y. Zhang, P. Chen, Y. Li, M. Liu, T. Gao, D. Ma, Y. Chen, Z. Cheng, X. Qiu *et al.*, *Nano letters*, 2013, **13**, 3439–3443.
- [5] P. Avouris, *Nano letters*, 2010, **10**, 4285–4294.
- [6] A. H. Castro Neto, F. Guinea, N. M. R. Peres, K. S. Novoselov and A. K. Geim, *RvMP*, 2009, **81**, 109–162.
- [7] S. Morozov, K. Novoselov, M. Katsnelson, F. Schedin, D. Elias, J. A. Jaszczak and A. Geim, *Physical review letters*, 2008, **100**, 016602.
- [8] A. A. Balandin, S. Ghosh, W. Bao, I. Calizo, D. Teweldebrhan, F. Miao and C. N. Lau, *Nano letters*, 2008, **8**, 902–907.
- [9] C. Lee, X. Wei, J. W. Kysar and J. Hone, *science*, 2008, **321**, 385–388.

- [10] M. D. Stoller, S. Park, Y. Zhu, J. An and R. S. Ruoff, *Nano letters*, 2008, **8**, 3498–3502.
- [11] R. R. Nair, P. Blake, A. N. Grigorenko, K. S. Novoselov, T. J. Booth, T. Stauber, N. M. Peres and A. K. Geim, *Science*, 2008, **320**, 1308–1308.
- [12] M. J. Allen, V. C. Tung and R. B. Kaner, *Chemical reviews*, 2010, **110**, 132–145.
- [13] A. Bianco, H.-M. Cheng, T. Enoki, Y. Gogotsi, R. H. Hurt, N. Koratkar, T. Kyotani, M. Monthieux, C. R. Park, J. M. Tascon *et al.*, *carbon*, 2013.
- [14] P. Wick, A. E. Louw-Gaume, M. Kucki, H. F. Krug, K. Kostarelos, B. Fadeel, K. A. Dawson, A. Salvati, E. Vázquez, L. Ballerini *et al.*, *Angewandte Chemie International Edition*, 2014, **53**, 7714–7718.
- [15] Z. Bo, S. Mao, Z. J. Han, K. Cen, J. Chen and K. K. Ostrikov, *Chemical Society Reviews*, 2015, **44**, 2108–2121.
- [16] M. Hiramatsu, K. Shiji, H. Amano and M. Hori, *Applied physics letters*, 2004, **84**, 4708–4710.
- [17] P. Hojati-Talemi and G. P. Simon, *Carbon*, 2010, **48**, 3993–4000.
- [18] X. Zhao, H. Tian, M. Zhu, K. Tian, J. Wang, F. Kang and R. Outlaw, *Journal of Power Sources*, 2009, **194**, 1208–1212.
- [19] W.-C. Shih, J.-M. Jeng, C.-T. Huang and J.-T. Lo, *Vacuum*, 2010, **84**, 1452–1456.
- [20] T.-C. Hung, C.-F. Chen and W.-T. Whang, *Electrochemical and Solid State Letters*, 2009, **12**, K41.
- [21] J. Wang, M. Zhu, R. Outlaw, X. Zhao, D. Manos, B. Holloway and V. Mammana, *Applied physics letters*, 2004, **85**, 1265–1267.

- [22] Z. Bo, Y. Yang, J. Chen, K. Yu, J. Yan and K. Cen, *Nanoscale*, 2013, **5**, 5180–5204.
- [23] D. Seo, S. Kumar and K. Ostrikov, *Carbon*, 2011, **49**, 4331–4339.
- [24] Z. Bo, W. Zhu, W. Ma, Z. Wen, X. Shuai, J. Chen, J. Yan, Z. Wang, K. Cen and X. Feng, *Advanced materials*, 2013, **25**, 5799–5806.
- [25] Q. Liao, N. Li, S. Jin, G. Yang and C. Wang, *ACS nano*, 2015, **9**, 5310–5317.
- [26] Z. Bo, K. Yu, G. Lu, P. Wang, S. Mao and J. Chen, *Carbon*, 2011, **49**, 1849–1858.
- [27] M. Cai, R. A. Outlaw, S. M. Butler and J. R. Miller, *Carbon*, 2012, **50**, 5481–5488.
- [28] J. Dong, Z. Yao, T. Yang, L. Jiang and C. Shen, *Scientific reports*, 2013, **3**, 1733.
- [29] Q. Yuan, H. Hu, J. Gao, F. Ding, Z. Liu and B. I. Yakobson, *Journal of the American Chemical Society*, 2011, **133**, 16072–16079.
- [30] B. Li, S. Li, J. Liu, B. Wang and S. Yang, *Nano letters*, 2015, **15**, 3073–3079.
- [31] S. Chul Shin, A. Yoshimura, T. Matsuo, M. Mori, M. Tanimura, A. Ishihara, K.-i. Ota and M. Tachibana, *Journal of applied physics*, 2011, **110**, 104308.
- [32] J. Liu, W. Sun, D. Wei, X. Song, T. Jiao, S. He, W. Zhang and C. Du, *Applied Physics Letters*, 2015, **106**, 043904.
- [33] L. Cheng, L. Qu and J.-H. Deng, *Materials Letters*, 2016, **176**, 165–168.
- [34] P. K. Roy, A. Ganguly, W.-H. Yang, C.-T. Wu, J.-S. Hwang, Y. Tai, K.-H. Chen, L.-C. Chen and S. Chattopadhyay, *Biosensors and Bioelectronics*, 2015, **70**, 137–144.
- [35] J. C. Claussen, A. Kumar, D. B. Jaroch, M. H. Khawaja, A. B. Hibbard, D. M. Porterfield and T. S. Fisher, *Advanced Functional Materials*, 2012, **22**, 3399–3405.

- [36] M. Fu, B. Quan, J. He, Z. Yao, C. Gu, J. Li and Y. Zhang, *Applied Physics Letters*, 2016, **108**, 121904.
- [37] J. R. Miller, R. Outlaw and B. Holloway, *Science*, 2010, **329**, 1637–1639.
- [38] Y. Kita, S. Hayashi, I. Kinoshita, M. Tachibana, M. Tachikawa, K. Kobayashi and M. Tanimura, *Journal of Applied Physics*, 2010, **108**, 013703.
- [39] V. Krivchenko, S. Evlashin, K. Mironovich, N. Verbitskiy, A. Nefedov, C. Wöll, A. Y. Kozmenkova, N. Suetin, S. Svyakhovskiy, D. Vyalikh *et al.*, *Scientific reports*, 2013, **3**, 3328.
- [40] S. C. Ray, N. Soin, T. Makgato, C. Chuang, W. Pong, S. S. Roy, S. K. Ghosh, A. M. Strydom and J. McLaughlin, *Scientific reports*, 2014, **4**, 1–7.
- [41] L. Zhang, Z. Sun, J. L. Qi, J. Shi, T. Hao and J. Feng, *Carbon*, 2016, **103**, 339–345.
- [42] A. Guirguis, S. R. Polaki, G. Sahoo, S. Ghosh, M. Kamruddin, A. Merenda, X. Chen, J. W. Maina, G. Szekely and L. F. Dumée, *Carbon*, 2020, **168**, 32–41.
- [43] Y. Wu, B. Yang, G. Han, B. Zong, H. Ni, P. Luo, T. Chong, T. Low and Z. Shen, *Advanced Functional Materials*, 2002, **12**, 489–494.
- [44] C. S. Rout, A. Kumar, G. Xiong, J. Irudayaraj and T. S. Fisher, *Applied Physics Letters*, 2010, **97**, 133108.
- [45] P. Russo, M. Xiao and N. Y. Zhou, *Carbon*, 2017, **120**, 54–62.
- [46] C. Liu, Z. Yu, D. Neff, A. Zhamu and B. Z. Jang, *Nano letters*, 2010, **10**, 4863–4868.
- [47] T. Kim, G. Jung, S. Yoo, K. S. Suh and R. S. Ruoff, *Acs Nano*, 2013, **7**, 6899–6905.
- [48] J. Li *et al.*, *Graphene*, 2012, **1**, 1.

- [49] F. Lufrano and P. Staiti, *Int. J. Electrochem. Sci*, 2010, **5**, 903–916.
- [50] B. E. Conway, *Electrochemical supercapacitors: scientific fundamentals and technological applications*, Springer Science & Business Media, 2013.
- [51] J. R. Miller and P. Simon, *Science Magazine*, 2008, **321**, 651–652.
- [52] Y. Wang, Y. Song and Y. Xia, *Chemical Society Reviews*, 2016, **45**, 5925–5950.
- [53] P. Simon, Y. Gogotsi and B. Dunn, *Science*, 2014, **343**, 1210–1211.
- [54] H. v. Helmholtz, *Annalen der Physik*, 1853, **165**, 353–377.
- [55] G. Gouy, *J. Phys. Theor. Appl*, 1910, **9**, 457–458.
- [56] D. L. Chapman, *The London, Edinburgh, and Dublin philosophical magazine and journal of science*, 1913, **25**, 475–481.
- [57] O. Stern, *Zeitschrift für Elektrochemie und angewandte physikalische Chemie*, 1924, **30**, 508–516.
- [58] L. L. Zhang and X. Zhao, *Chemical Society Reviews*, 2009, **38**, 2520–2531.
- [59] F. Wang, X. Wu, X. Yuan, Z. Liu, Y. Zhang, L. Fu, Y. Zhu, Q. Zhou, Y. Wu and W. Huang, *Chemical Society Reviews*, 2017, **46**, 6816–6854.
- [60] L. Zhang, X. Hu, Z. Wang, F. Sun and D. G. Dorrell, *Renewable and Sustainable Energy Reviews*, 2018, **81**, 1868–1878.
- [61] G. Ren, X. Pan, S. Bayne and Z. Fan, *Carbon*, 2014, **71**, 94–101.
- [62] D. H. Seo, S. Yick, Z. J. Han, J. H. Fang and K. Ostrikov, *ChemSusChem*, 2014, **7**, 2317–2324.

- [63] D. H. Seo, Z. J. Han, S. Kumar and K. Ostrikov, *Advanced Energy Materials*, 2013, **3**, 1316–1323.
- [64] G. Xiong, C. Meng, R. G. Reifengerger, P. P. Irazoqui and T. S. Fisher, *Advanced Energy Materials*, 2014, **4**, 1300515.
- [65] D. Akinwande, N. Petrone and J. Hone, *Nature communications*, 2014, **5**, 1–12.
- [66] A. Gurarslan, Y. Yu, L. Su, Y. Yu, F. Suarez, S. Yao, Y. Zhu, M. Ozturk, Y. Zhang and L. Cao, *ACS nano*, 2014, **8**, 11522–11528.
- [67] K. S. Kim, Y. Zhao, H. Jang, S. Y. Lee, J. M. Kim, K. S. Kim, J.-H. Ahn, P. Kim, J.-Y. Choi and B. H. Hong, *nature*, 2009, **457**, 706.
- [68] H. J. Park, B. W. Ahn, T. Y. Kim, J. W. Lee, Y. H. Jung, Y. S. Choi, Y. I. Song and S. J. Suh, *Thin Solid Films*, 2015, **587**, 8–13.
- [69] A. Palla-Papavlu, M. Filipescu, S. Vizireanu, L. Vogt, S. Antohe, M. Dinescu, A. Wokaun and T. Lippert, *Applied Surface Science*, 2016, **374**, 312–317.
- [70] C. Constantinescu, S. Vizireanu, V. Ion, G. Aldica, S. D. Stoica, A. Lazea-Stoyanova, A.-P. Alloncle, P. Delaporte and G. Dinescu, *Applied Surface Science*, 2016, **374**, 49–55.
- [71] R. A. Quinlan, A. Javier, E. E. Foos, L. Buckley, M. Zhu, K. Hou, E. Widenkvist, M. Drees, U. Jansson and B. C. Holloway, *Journal of Vacuum Science & Technology B, Nanotechnology and Microelectronics: Materials, Processing, Measurement, and Phenomena*, 2011, **29**, 030602.
- [72] P. Gupta, P. D. Dongare, S. Grover, S. Dubey, H. Mamgain, A. Bhattacharya and M. M. Deshmukh, *Scientific reports*, 2014, **4**, 3882.

- [73] Z. Zhang, C.-S. Lee and W. Zhang, *Advanced Energy Materials*, 2017, **7**, 1700678.
- [74] D. J. Cott, M. Verheijen, O. Richard, I. Radu, S. De Gendt, S. van Elshocht and P. M. Vereecken, *Carbon*, 2013, **58**, 59–65.
- [75] S. Ghosh, S. R. Polaki, N. Kumar, S. Amirthapandian, M. Kamruddin and K. K. Ostrikov, *Beilstein journal of nanotechnology*, 2017, **8**, 1658–1670.
- [76] K. V. Mironovich, D. M. Itkis, D. A. Semenenko, S. A. Dagesian, L. V. Yashina, E. Y. Kataev, Y. A. Mankelevich, N. V. Suetin and V. A. Krivchenko, *Physical Chemistry Chemical Physics*, 2014, **16**, 25621–25627.
- [77] X. Shuai, Z. Bo, J. Kong, J. Yan and K. Cen, *RSC advances*, 2017, **7**, 2667–2675.
- [78] S. Ghosh, T. Mathews, B. Gupta, A. Das, N. G. Krishna and M. Kamruddin, *Nano-Structures & Nano-Objects*, 2017, **10**, 42–50.
- [79] H. Watanabe, H. Kondo, M. Hiramatsu, M. Sekine, S. Kumar, K. Ostrikov and M. Hori, *Plasma Processes and Polymers*, 2013, **10**, 582–592.
- [80] Z. Bo, Y. Tian, Z. J. Han, S. Wu, S. Zhang, J. Yan, K. Cen and K. K. Ostrikov, *Nanoscale Horizons*, 2017, **2**, 89–98.
- [81] J. L. Qi, X. Wang, J. H. Lin, F. Zhang, J. C. Feng and W.-D. Fei, *Nanoscale*, 2015, **7**, 3675–3682.
- [82] S. Vizireanu, M. D. Ionita, G. Dinescu, I. Enculescu, M. Baibarac and I. Baltog, *Plasma Processes and Polymers*, 2012, **9**, 363–370.
- [83] S. Ghosh, K. Ganesan, S. Polaki, T. Mathews, S. Dhara, M. Kamruddin and A. Tyagi, *Applied Surface Science*, 2015, **349**, 576–581.
- [84] J. Wang and S. Kaskel, *Journal of Materials Chemistry*, 2012, **22**, 23710–23725.

- [85] T. S. Hui and M. A. A. Zaini, *Carbon Letters (Carbon Lett.)*, 2015, **16**, 275–280.
- [86] S. Ghosh, G. Sahoo, S. Polaki, N. G. Krishna, M. Kamruddin and T. Mathews, *Journal of Applied Physics*, 2017, **122**, 214902.
- [87] S. Vizireanu, M. D. Ionita, R. E. Ionita, S. D. Stoica, C. M. Teodorescu, M. A. Husanu, N. G. Apostol, M. Baibarac, D. Panaitescu and G. Dinescu, *Plasma Processes and Polymers*, 2017, **14**, 1700023.
- [88] Y.-R. Nian and H. Teng, *Journal of Electroanalytical Chemistry*, 2003, **540**, 119–127.
- [89] H. Cao, X. Peng, M. Zhao, P. Liu, B. Xu and J. Guo, *RSC advances*, 2018, **8**, 2858–2865.
- [90] A. I. Belova, D. G. Kwabi, L. V. Yashina, Y. Shao-Horn and D. M. Itkis, *The Journal of Physical Chemistry C*, 2017, **121**, 1569–1577.
- [91] C. Paliteiro, A. Hamnett and J. B. Goodenough, *Journal of electroanalytical chemistry and interfacial electrochemistry*, 1987, **233**, 147–159.
- [92] J. Lin, H. Jia, Y. Cai, S. Chen, H. Liang, X. Wang, F. Zhang, J. Qi, J. Cao, J. Feng *et al.*, *Journal of Materials Chemistry A*, 2018, **6**, 908–917.
- [93] S. Deheryan, D. J. Cott, P. W. Mertens, M. Heyns and P. M. Vereecken, *Electrochimica Acta*, 2014, **132**, 574–582.
- [94] Y. Zhang, Q. Zou, H. S. Hsu, S. Raina, Y. Xu, J. B. Kang, J. Chen, S. Deng, N. Xu and W. P. Kang, *ACS applied materials & interfaces*, 2016, **8**, 7363–7369.
- [95] D. H. Seo, S. Yick, D. Su, G. Wang, Z. J. Han and K. K. Ostrikov, *Carbon*, 2015, **91**, 386–394.

- [96] Q. Lv, F. Jing, Y. Huang, J. Xiao, Y. Zhang, F. Xiao, J. Xiao and S. Wang, *ACS Sustainable Chemistry & Engineering*, 2018, **6**, 6042–6051.
- [97] Y.-W. Chi, C.-C. Hu, H.-H. Shen and K.-P. Huang, *Nano letters*, 2016, **16**, 5719–5727.
- [98] D. Aradilla, M. Delaunay, S. Sadki, J.-M. Gérard and G. Bidan, *Journal of Materials Chemistry A*, 2015, **3**, 19254–19262.
- [99] B. Ouyang, Y. Zhang, Z. Zhang, H. J. Fan and R. Rawat, *RSC Advances*, 2016, **6**, 23968–23973.
- [100] B. Ankamwar, P. Das and U. Sur, *Indian Journal of Physics*, 2016, **90**, 391–397.
- [101] D. S. Patil, S. A. Pawar, J. H. Kim, P. S. Patil and J. C. Shin, *Electrochimica Acta*, 2016, **213**, 680–690.
- [102] L. He and S. C. Tjong, *Rsc Advances*, 2017, **7**, 2058–2065.
- [103] S. Gupta and N. Dimakis, *Applied Surface Science*, 2019, **467**, 760–772.
- [104] S. Gupta, S. Carrizosa, J. Jasinski and N. Dimakis, *AIP Advances*, 2018, **8**, 065225.
- [105] A. Majeed, W. Ullah, A. W. Anwar, F. Nasreen, A. Sharif, G. Mustafa and A. Khan, *Journal of Alloys and Compounds*, 2016, **671**, 1–10.
- [106] A. Jana, E. Scheer and S. Polarz, *Beilstein journal of nanotechnology*, 2017, **8**, 688–714.
- [107] S. Ghosh, S. Polaki, G. Sahoo, E.-M. Jin, M. Kamruddin, J. S. Cho and S. M. Jeong, *Journal of Industrial and Engineering Chemistry*, 2019, **72**, 107–116.
- [108] J. Li, M. Zhu, Z. An, Z. Wang, M. Toda and T. Ono, *Journal of Power Sources*, 2018, **401**, 204–212.

- [109] X. Wang, Y. Wang, C. Zhao, Y. Zhao, B. Yan and W. Zheng, *New Journal of Chemistry*, 2012, **36**, 1902–1906.
- [110] A. González, E. Goikolea, J. A. Barrena and R. Mysyk, *Renewable and Sustainable Energy Reviews*, 2016, **58**, 1189–1206.
- [111] G. A. Ali, A. Divyashree, S. Supriya, K. F. Chong, A. S. Ethiraj, M. Reddy, H. Algarni and G. Hegde, *Dalton Transactions*, 2017, **46**, 14034–14044.
- [112] A. Balducci, *Journal of Power Sources*, 2016, **326**, 534–540.
- [113] Z. Bo, Z. Wen, H. Kim, G. Lu, K. Yu and J. Chen, *Carbon*, 2012, **50**, 4379–4387.
- [114] J. Piwek, A. Platek, K. Fic and E. Frackowiak, *Electrochimica Acta*, 2016, **215**, 179–186.
- [115] D. G. Gromadskyi, J. H. Chae, S. A. Norman and G. Z. Chen, *Applied energy*, 2015, **159**, 39–50.
- [116] C. Hu, E. Zhao, N. Nitta, A. Magasinski, G. Berdichevsky and G. Yushin, *Journal of Power Sources*, 2016, **326**, 569–574.
- [117] C.-W. Liew, S. Ramesh and A. Arof, *Energy*, 2016, **109**, 546–556.
- [118] D. P. Dubal, J. Suarez-Guevara, D. Tonti, E. Enciso and P. Gomez-Romero, *Journal of Materials Chemistry A*, 2015, **3**, 23483–23492.
- [119] S. Ghosh, S. Polaki, P. Ajikumar, N. Krishna and M. Kamruddin, *Indian Journal of Physics*, 2018, **92**, 337–342.
- [120] M. Lillo-Ródenas, D. Cazorla-Amorós and A. Linares-Solano, *Carbon*, 2003, **41**, 267–275.

- [121] Y. Zhu, S. Murali, M. D. Stoller, K. Ganesh, W. Cai, P. J. Ferreira, A. Pirkle, R. M. Wallace, K. A. Cychosz, M. Thommes *et al.*, *science*, 2011, **332**, 1537–1541.
- [122] H. Kim, K.-Y. Park, J. Hong and K. Kang, *Scientific reports*, 2014, **4**, 5278.
- [123] P. M. Martin, *Handbook of deposition technologies for films and coatings: science, applications and technology*, William Andrew, 2009.
- [124] I. Levchenko, M. Keidar, S. Xu, H. Kersten and K. Ostrikov, *Journal of Vacuum Science & Technology B*, 2013, **31**, 050801.
- [125] K. L. Chopra, *Thin film phenomena*, McGraw-hill, 1969.
- [126] R. C. Jaeger, *Introduction to Microelectronic Fabrication: Volume 5 of Modular Series on Solid State Devices*, Prentice Hall Upper Saddle River, 2001.
- [127] J. F. Watts and J. Wolstenholme, *An introduction to surface analysis by XPS and AES*, Wiley-VCH, 2003.
- [128] J. R. Ferraro, *Introductory raman spectroscopy*, Elsevier, 2003.
- [129] L. Malard, M. Pimenta, G. Dresselhaus and M. Dresselhaus, *Physics Reports*, 2009, **473**, 51–87.
- [130] A. Kozbial, Z. Li, C. Conaway, R. McGinley, S. Dhingra, V. Vahdat, F. Zhou, B. D' Urso, H. Liu and L. Li, *Langmuir*, 2014, **30**, 8598–8606.
- [131] E. N. Kaufmann, *Characterization of Materials*, Wiley-VCH, 2003.
- [132] Y. Shao, M. F. El-Kady, L. J. Wang, Q. Zhang, Y. Li, H. Wang, M. F. Mousavi and R. B. Kaner, *Chemical Society Reviews*, 2015, **44**, 3639–3665.
- [133] Y. Ma, M. Wang, N. Kim, J. Suhr and H. Chae, *Journal of Materials Chemistry A*, 2015, **3**, 21875–21881.

- [134] W. S. Choi, Y. Park, S. H. Kwon, D.-D. Lee, Y.-H. Joung, J. H. Kim and H. Kang, *Journal of Nanoscience and Nanotechnology*, 2016, **16**, 11477–11479.
- [135] N. A. Nayan and N. Ramli, *Int. J. Appl. Eng. Res*, 2016, **11**, 7815–22.
- [136] A. C. Ferrari and D. M. Basko, *Nature nanotechnology*, 2013, **8**, 235.
- [137] S. Ghosh, K. Ganesan, S. R. Polaki, T. Ravindran, N. G. Krishna, M. Kamruddin and A. Tyagi, *Journal of Raman Spectroscopy*, 2014, **45**, 642–649.
- [138] Y. Yamada, Y. Suzuki, H. Yasuda, S. Uchizawa, K. Hirose-Takai, Y. Sato, K. Sue-naga and S. Sato, *Carbon*, 2014, **75**, 81–94.
- [139] K. Ganesan, S. Ghosh, N. G. Krishna, S. Ilango, M. Kamruddin and A. Tyagi, *Physical Chemistry Chemical Physics*, 2016, **18**, 22160–22167.
- [140] E. Redondo, E. Goikolea and R. Mysyk, *Electrochimica Acta*, 2016, **221**, 177–183.
- [141] C. H. A. Wong and M. Pumera, *The Journal of Physical Chemistry C*, 2016, **120**, 4682–4690.
- [142] D. Premathilake, R. A. Outlaw, S. G. Parler, S. M. Butler and J. R. Miller, *Carbon*, 2017, **111**, 231–237.
- [143] Y. Yan, Y. Luo, J. Ma, B. Li, H. Xue and H. Pang, *Small*, 2018, **14**, 1801815.
- [144] P. Simon and Y. Gogotsi, in *Nanoscience and technology: a collection of reviews from Nature journals*, World Scientific, 2010, pp. 320–329.
- [145] E. Frackowiak, *Physical chemistry chemical physics*, 2007, **9**, 1774–1785.
- [146] E. Frackowiak and F. Beguin, *Carbon*, 2001, **39**, 937–950.
- [147] M. Inagaki, H. Konno and O. Tanaike, *Journal of power sources*, 2010, **195**, 7880–7903.

- [148] A. Borenstein, O. Hanna, R. Attias, S. Luski, T. Brousse and D. Aurbach, *Journal of Materials Chemistry A*, 2017, **5**, 12653–12672.
- [149] Y. Wu, P. Qiao, T. Chong and Z. Shen, *Advanced materials*, 2002, **14**, 64–67.
- [150] H.-T. Zhou, N. Yu, F. Zou, Z.-H. Yao, G. Gao and C.-M. Shen, *Chinese Physics B*, 2016, **25**, 096106.
- [151] Y. H. Jung and W. S. Choi, *Journal of nanoscience and nanotechnology*, 2016, **16**, 5298–5301.
- [152] J. E. Zuliani, S. Tong, C. Q. Jia and D. W. Kirk, *Journal of Power Sources*, 2018, **395**, 271–279.
- [153] S. Bachmann, M. Schulze, J. Morasch, S. Hesse, L. Hussein, L. Krell, J. Schnagl, R. W. Stark and S. Narayan, *Applied Surface Science*, 2016, **371**, 613–623.
- [154] V. MĂRĂSCU, S. Vizireanu, S. Stoica, V. Barna, A. Lazeastoyanova and G. Diniescu, *Romanian Reports in Physics*, 2016, **68**, 1108–1114.
- [155] G. Sahoo, S. Polaki, S. Ghosh, N. Krishna and M. Kamruddin, *Journal of Power Sources*, 2018, **401**, 37–48.
- [156] G. Sahoo, S. Polaki, S. Ghosh, N. Krishna, M. Kamruddin and K. K. Ostrikov, *Energy Storage Materials*, 2018, **14**, 297–305.
- [157] S. Kurita, A. Yoshimura, H. Kawamoto, T. Uchida, K. Kojima, M. Tachibana, P. Molina-Morales and H. Nakai, *Journal of Applied Physics*, 2005, **97**, 104320.
- [158] A. C. Ferrari and J. Robertson, *Philosophical Transactions of the Royal Society of London. Series A: Mathematical, Physical and Engineering Sciences*, 2004, **362**, 2477–2512.

- [159] N. Ghaderi and M. Peressi, *The Journal of Physical Chemistry C*, 2010, **114**, 21625–21630.
- [160] A. S. Dobrota, I. A. Pašti, S. V. Mentus and N. V. Skorodumova, *Physical Chemistry Chemical Physics*, 2017, **19**, 8530–8540.
- [161] M. J. Gira, K. P. Tkacz and J. R. Hampton, *Nano convergence*, 2016, **3**, 6.
- [162] M. Xie, L. Yang, Y. Ji, Z. Wang, X. Ren, Z. Liu, A. M. Asiri, X. Xiong and X. Sun, *Nanoscale*, 2017, **9**, 16612–16615.
- [163] Z. Lin, Y. Liu, Y. Yao, O. J. Hildreth, Z. Li, K. Moon and C.-p. Wong, *The Journal of Physical Chemistry C*, 2011, **115**, 7120–7125.
- [164] M. J. Bleda-Martínez, J. A. Maciá-Agulló, D. Lozano-Castelló, E. Morallon, D. Cazorla-Amorós and A. Linares-Solano, *Carbon*, 2005, **43**, 2677–2684.
- [165] C.-M. Chen, Q. Zhang, X.-C. Zhao, B. Zhang, Q.-Q. Kong, M.-G. Yang, Q.-H. Yang, M.-Z. Wang, Y.-G. Yang, R. Schlögl *et al.*, *Journal of Materials Chemistry*, 2012, **22**, 14076–14084.
- [166] Y. J. Oh, J. J. Yoo, Y. I. Kim, J. K. Yoon, H. N. Yoon, J.-H. Kim and S. B. Park, *Electrochimica Acta*, 2014, **116**, 118–128.
- [167] Z. Gao, X. Wang, J. Chang, D. Wu, L. Wang, X. Liu, F. Xu, Y. Guo and K. Jiang, *RSC Advances*, 2015, **5**, 48665–48674.
- [168] M. Winter and R. J. Brodd, *Chemical reviews*, 2005, **105**, 1021–1021.
- [169] P. Simon, T. Brousse and F. Favier, *Supercapacitors based on carbon or pseudocapacitive materials*, Wiley Online Library, 2017.

- [170] G. Sahoo, S. Ghosh, S. Polaki, T. Mathews and M. Kamruddin, *Nanotechnology*, 2017, **28**, 415702.
- [171] C. Zhao, X. Wang, S. Wang, Y. Wang, Y. Zhao and W. Zheng, *international journal of hydrogen energy*, 2012, **37**, 11846–11852.
- [172] C. Jiang, B. Zhao, J. Cheng, J. Li, H. Zhang, Z. Tang and J. Yang, *Electrochimica Acta*, 2015, **173**, 399–407.
- [173] A. Eckmann, A. Felten, A. Mishchenko, L. Britnell, R. Krupke, K. S. Novoselov and C. Casiraghi, *Nano letters*, 2012, **12**, 3925–3930.
- [174] O. Maslova, M. Ammar, G. Guimbretière, J.-N. Rouzaud and P. Simon, *Physical Review B*, 2012, **86**, 134205.
- [175] L. Wang, J. Jin, J. Cao, P. Yang and Q. Peng, *Crystals*, 2018, **8**, 160.
- [176] G. Sahoo, S. Polaki, P. Anees, S. Ghosh, S. Dhara and M. Kamruddin, *Physical Chemistry Chemical Physics*, 2019, **21**, 25196–25205.
- [177] J. Li, M. Zhu, Z. Wang and T. Ono, *Applied Physics Letters*, 2016, **109**, 153901.
- [178] T. C. Kaspar, T. Droubay, S. A. Chambers and P. S. Bagus, *The Journal of Physical Chemistry C*, 2010, **114**, 21562–21571.
- [179] M. A. Hossain, R. Al-Gaashani, H. Hamoudi, M. J. Al Marri, I. A. Hussein, A. Belaidi, B. A. Merzougui, F. H. Alharbi and N. Tabet, *Materials Science in Semiconductor Processing*, 2017, **63**, 203–211.
- [180] B. Sone, X. Fuku and M. Maaza, *Int. J. Electrochem. Sci*, 2016, **11**, 8204–8220.
- [181] X. Zhang, J. Zhou, H. Song, C. Liu, S. Zhang and X. Chen, *Carbon*, 2016, **99**, 370–374.

- [182] K. Spilarewicz-Stanek, A. Kisielewska, J. Ginter, K. Bałuszyńska and I. Piwoński, *RSC Advances*, 2016, **6**, 60056–60067.
- [183] O. Leenaerts, B. Partoens, F. Peeters, A. Volodin and C. Van Haesendonck, *Journal of Physics: Condensed Matter*, 2016, **29**, 035003.
- [184] D. Ziegler, P. Gava, J. Güttinger, F. Molitor, L. Wirtz, M. Lazzeri, A. Saitta, A. Stemmer, F. Mauri and C. Stampfer, *Physical Review B*, 2011, **83**, 235434.
- [185] N. T. Khoa, S. W. Kim, D.-H. Yoo, E. J. Kim and S. H. Hahn, *Applied Catalysis A: General*, 2014, **469**, 159–164.
- [186] G. D. M. Dabera, M. Walker, A. M. Sanchez, H. J. Pereira, R. Beanland and R. A. Hatton, *Nature communications*, 2017, **8**, 1–10.
- [187] M. T. Greiner, L. Chai, M. G. Helander, W.-M. Tang and Z.-H. Lu, *Advanced Functional Materials*, 2012, **22**, 4557–4568.
- [188] S. Hietzschold, S. Hillebrandt, F. Ullrich, J. Bombsch, V. Rohnacher, S. Ma, W. Liu, A. Köhn, W. Jaegermann, A. Pucci *et al.*, *ACS applied materials & interfaces*, 2017, **9**, 39821–39829.
- [189] S. R. Gawali, D. P. Dubal, V. G. Deonikar, S. S. Patil, S. D. Patil, P. Gomez-Romero, D. R. Patil and J. Pant, *ChemistrySelect*, 2016, **1**, 3471–3478.
- [190] N. Duraisamy, A. Numan, S. O. Fatin, K. Ramesh and S. Ramesh, *Journal of colloid and interface science*, 2016, **471**, 136–144.
- [191] H. Xiao, S. Yao, H. Liu, F. Qu, X. Zhang and X. Wu, *Progress in Natural Science: Materials International*, 2016, **26**, 271–275.
- [192] D. Banerjee, U. K. Ghorai, N. S. Das, B. Das, S. Thakur and K. K. Chattopadhyay, *ACS omega*, 2018, **3**, 6311–6320.

- [193] N. A. M. Zaid and N. H. Idris, *Scientific reports*, 2016, **6**, 1–8.
- [194] G. Kresse and J. Hafner, *Physical Review B*, 1993, **47**, 558.
- [195] A. Tkatchenko, R. A. DiStasio Jr, R. Car and M. Scheffler, *Physical review letters*, 2012, **108**, 236402.
- [196] C. R. Rêgo, P. Tereshchuk, L. N. Oliveira and J. L. Da Silva, *Physical Review B*, 2017, **95**, 235422.
- [197] W. Tang, E. Sanville and G. Henkelman, *Journal of Physics: Condensed Matter*, 2009, **21**, 084204.
- [198] P. Khomyakov, G. Giovannetti, P. Rusu, G. v. Brocks, J. Van den Brink and P. J. Kelly, *Physical Review B*, 2009, **79**, 195425.
- [199] B. Zhao, J. Song, P. Liu, W. Xu, T. Fang, Z. Jiao, H. Zhang and Y. Jiang, *Journal of Materials Chemistry*, 2011, **21**, 18792–18798.
- [200] G. Sahoo, S. Polaki, N. Krishna and M. Kamruddin, *Journal of Physics D: Applied Physics*, 2019, **52**, 375501.
- [201] A. Noori, M. F. El-Kady, M. S. Rahmanifar, R. B. Kaner and M. F. Mousavi, *Chemical Society Reviews*, 2019, **48**, 1272–1341.
- [202] J. R. Miller and R. A. Outlaw, *Journal of The Electrochemical Society*, 2015, **162**, A5077–A5082.
- [203] K. Mishra, S. Ghosh, T. Ravindran, S. Amirthapandian and M. Kamruddin, *The Journal of Physical Chemistry C*, 2016, **120**, 25092–25100.

- [204] S. Vizireanu, G. Dinescu, L. C. Nistor, M. Baibarac, G. Ruxanda, M. Stancu and D. Ciuparu, *Physica E: Low-dimensional Systems and Nanostructures*, 2013, **47**, 59–65.
- [205] H. J. Cho, H. Kondo, K. Ishikawa, M. Sekine, M. Hiramatsu and M. Hori, *Carbon*, 2014, **68**, 380–388.
- [206] J. Zhu, A. S. Childress, M. Karakaya, S. Dandeliya, A. Srivastava, Y. Lin, A. M. Rao and R. Podila, *Advanced Materials*, 2016, **28**, 7185–7192.
- [207] P. Kanninen, N. D. Luong, I. V. Anoshkin, A. Tsapenko, J. Seppälä, A. G. Nasibulin, T. Kallio *et al.*, *Nanotechnology*, 2016, **27**, 235403.
- [208] R. Vellacheri, H. Zhao, M. Mühlstädt, J. Ming, A. Al-Haddad, M. Wu, K. D. Jandt and Y. Lei, *Advanced Materials Technologies*, 2016, **1**, 1600012.
- [209] S. Ghosh, B. Gupta, K. Ganesan, A. Das, M. Kamruddin, S. Dash and A. Tyagi, *Materials Today: Proceedings*, 2016, **3**, 1686–1692.
- [210] J. L. Qi, J. H. Lin, X. Wang, J. Le Guo, L. F. Xue, J. C. Feng and W.-D. Fei, *Nano Energy*, 2016, **26**, 657–667.
- [211] M. Reddy, R. Jose, A. Le Viet, K. I. Ozoemena, B. Chowdari and S. Ramakrishna, *Electrochimica Acta*, 2014, **128**, 198–202.
- [212] K. Lehmann, O. Yurchenko, A. Heilemann, S. Vierrath, L. Zielke, S. Thiele, A. Fischer and G. Urban, *Carbon*, 2017, **118**, 578–587.